Experimental Measurement of Laminar Flame Speed of a Novel Liquid Biofuel 1,3 Dimethoxyoctane

By

Carlos Alberto Gomez Casanova

A Thesis submitted to the Faculty of Graduate Studies of

The University of Manitoba

in partial fulfillment of the requirements of the degree of

Master Of Science

Department of Mechanical Engineering

University of Manitoba

Winnipeg

Abstract

Laminar flame speed of a novel liquid bio-fuel has been determined experimentally using a closed spherical combustion vessel of 29 L equipped with two pairs of fused silica windows for optical access at atmospheric pressure and elevated temperature conditions. Schlieren technique was used to visualize and record the temporal evolution of the outwardly spherical flame front, and an in-house developed Matlab code was employed to process the flame front images and calculate its area by applying several image processing techniques. The test conditions consisted of varying the fuel-air mixture equivalence ratio at atmospheric standard pressure and different initial temperatures.

Validation of the present method was achieved by measuring and comparing the flame speed of methane/air and n-heptane/air mixture with their published counterparts. Experimental results revealed comparable laminar flame speed of the novel liquid biofuel (1, 3-dimethoxyoctane) to heavy liquid hydrocarbons such as n-heptane and isooctane, especially at stoichiometric and fuel rich conditions. Additionally, the flammability limits of this novel fuel showed similarities with those of gaseous hydrocarbons fuels (e.g. methane, ethane) but higher than those of liquid hydrocarbons (e.g. diesel, gasoline).

Acknowledgements

I would like to express my gratitude to my supervisor Dr. Madjid Birouk for giving me the opportunity of joining the Energy and Combustion Laboratory and also providing guidance during my graduate program. I would like to thank to the technical staff, which made possible through their knowledge and experience the development of the present thesis, especially to S. Karnaoukh, D. Tataryn and the personnel at the machine shop. Additionally, I want to thank Dr. Thomas, who provided me expertise and advice on image processing. I would also acknowledge the financial support received from BioFuelNet Canada through the development of the present research work. I would like to thank the Department of Mechanical Engineering of the University of Manitoba for their support through the teaching assistantships I obtained. Finally, I want to express my sincere gratitude to my family, especially to my dad, who has been an example in my life. I also want to thank the support and advice of Sarita and German, who gave me invaluable guidance and encouragement during this program.

Table of Contents

Abstract ii

Acknowledgements iii

List of Figures viii

List of Tables x

Nomenclature xii

Chapter 1 – Introduction 1

Chapter 2 - Literature Review 4

2.1 Introduction 4

2.2 Laminar flame speed of pure biofuels 4

2.2.1 Numerical investigations 4

2.2.2 Experimental investigations 6

2.3 Flame speed of biofuel blends 12

2.3.1 Numerical investigations 12

2.3.2 Experimental investigations 13

2.4 Flammability of fuels 18

Chapter 3 – Methodology 22

3.1 Introduction 22

3.2 Advantages and disadvantages of laminar flame speed measurement methods 22

3.3. Outwardly-propagating spherical flames 25

Chapter 4 – Experimental Facility 29

4.1 Introduction 29

4.2 Spherical combustion chamber 29

4.3 Fuel Supply System 32

4.3.1 Fuel Injection by the partial pressure method 32
4.3.2 Fuel Injection by the volumetric method 37
4.3.3 Vacuum system 40
4.4 Combustion chamber pressure control 41
4.5 Heating system 42
4.5.1 Fuel vaporization and condensation 43
4.5.2 Heating coils 44
4.5.3 Vaporization chamber 45
4.5.4 Preheated air 46
4.6 Ignition system 47
4.7 Flame visualization and processing 50
4.7.1 Schlieren system 50
4.7.2 Image post processing 53
4.8 Instrumentation 55
4.8.1 Data acquisition system 55
4.8.2 Voltage amplifier 57
4.8.3 Thermocouples 58
4.8.4 User interface 59
Chapter 5 – Results and discussion 61
5.1 Introduction 61
5.2 Validation of the experimental setup and methodology 61
5.2.1 Methane/air mixtures 61
5.2.2 Heptane/air mixtures 65
5.3 Laminar flame speed of 1,3-DMO 68
5.4 Flammability limits of 1,3-DMO fuel 74

Chapter 6 – Conclusions and Recommendations 77
6.1 Conclusions 77
6.2 Recommendations for future work 78
References 81
Appendix A – Instrumentation A-1
Appendix B – Uncertainty analysis B-1
B.1 Formulation B-1
B.2 Calculation B-4
Appendix C – Image Processing Code C-1
C.1. Introduction C-1
C.2. Matlab code C-2
Appendix D – Procedure of operation D-1
D.1. Components D-1
D.2. Procedure D-2
D.2.1. Preliminary activities D-2
D.2.2. Experiments D-5
Appendix E – Calibration of relief valves E-1
Appendix F – Tables F-1
Appendix G – Drawings G-1
G.1 – Ignition electrode holder G-1
G.1.1 – Exploded view G-1
G.1.2 – Holder's body G-2
G.1.3 – Gap adjustment bolt G-3
G.1.4 – Alignment bolt G-4
G.1.5 – Alignment bolt end G-5

G.2 – Vaporization system.....G-6
G.2.1 – Liquid fuel tank.....G-6
G.2.2 – Liquid fuel tank cap.....G-7
G.2.3 – Vaporization chamber.....G-8
G.2.4 – Vaporization chamber cap.....G-9

List of Figures

Figure 2.1. Laminar flame speed of oxygenated fuel surrogates (1 bar) 7

Figure 4.1. Schematic of the experimental setup 30

Figure 4.2. A photograph of the spherical combustion chamber 31

Figure 4.3. Pressure transducers 35

Figure 4.4. Schematic of the fuel supply system by the partial pressure methodology 36

Figure 4.5. Photograph of the fuel supply system 37

Figure 4.6. Schematic of the fuel supply system by the volumetric methodology 38

Figure 4.7. Photograph of the fuel supply system by the volumetric methodology 38

Figure 4.8. Vacuum pump 41

Figure 4.9. Relief valve 42

Figure 4.10. Heating coil 45

Figure 4.11. The vaporization chamber with the heating tape 46

Figure 4.12. Preheated air line 47

Figure 4.13. Schematic of the ignition system 48

Figure 4.14. Spark gap between the two electrodes 48

Figure 4.15. Electrode holder 49

Figure 4.16. Ignition system power supply 49

Figure 4.17. Schematic of the Schlieren system 51

Figure 4.18. Spherical mirrors 52

Figure 4.19. High speed camera 52

Figure 4.20. Light source 52

Figure 4.21. Schlieren flame edge photographs 53

Figure 4.22. Post processing sequence 55

Figure 4.23. Data acquisition system..... 57

Figure 4.24. Voltage amplifier 58

Figure 4.25. Locations of the thermocouples 59

Figure 4.26. User interface 60

Fig 5.2 shows three different databases on density ratio of methane/air mixtures used for determining the laminar burning velocity 64

Figure 5.3. Laminar flame speed of n-heptane/air mixtures..... 67

Figure 5.5. Laminar flame speed vs. stretch rate of 1,3-DMO/air mixtures 70

Figure 5.6. Markstein length vs. equivalence ratio 72

Figure 5.7. Laminar flame speed vs. equivalence ratio of 1, 3-DMO/air mixtures..... 74

Figure 5.8. Flammability limits of fuels..... 76

Figure D.1. Change in heating coil temperature when turning off the heating elements ... D-8

List of Tables

Table 2.1 Summary of published test conditions adopted for determining (experimentally or/and numerically) laminar flame speed of pure biofuels 11

Table 2.2 Summary of published test conditions adopted for determining (experimentally and/or numerically) laminar flame speed of biofuel blends 18

Table 2.3 Flammability limits of some fuels and representative compounds 21

Table 4.1. Fuel conditions 40

Table 4.2 Coefficients for the Antoine equation 43

Table 5.1. Test conditions for methane/air mixtures 64

Table 5.2. Published test conditions for determining laminar flame speed of methane/air mixtures 65

Table 5.3. Temperature reading in the combustion chamber 67

Table 5.4. Test conditions for heptane/air mixtures 67

Table 5.5. Published laminar flame speed of n-heptane/air mixtures 68

Table 5.6. Test conditions for 1, 3-DMO/air mixtures 69

Table 5.7. Uncertainty of laminar flame speed measurements 74

Table 5.8. Measured fuel samples/quantities for determining flammability limits of 1,3-DMO 75

Table 5.9. Flammability limits of 1,3-DMO 75

Table B.1. Elemental uncertainties contributing to the total uncertainty B-2

Table B.2. Total uncertainty of laminar flame speed B-6

Table E.1. Parameters of Eq. E.1 and E.2 ..... E-2

Table F.1. Partial pressure of tested fuels F-1

Table F.2. Fuel volumes F-2

Table F.3. Condensation Temperatures F-3

Nomenclature

A = Experimental coefficient of Antoine Equation (Eq. 4.8)

B = Experimental coefficient of Antoine Equation (Eq. 4.8)

B_{SL} = Total bias uncertainty [cm/s]; (Eq. B.1)

C = Experimental coefficient of Antoine Equation (Eq. 4.8)

k = Stretch rate [s^{-1}]; (Eq. 3.2)

L_b = Markstein length [cm] (Eq. 3.2)

m = Mass [kg]; (Eq. 4.7)

m_F = Mass of fuel [kg]; (Eq. 4.3)

m_A = Mass of fuel/air mixture [kg]; (Eq. 4.3)

N_i = Moles of individual component [mol]; (Eq. 4.2)

N_f = Moles of fuel [mol]; (Eq. 4.4)

N_m = Moles of fuel/air mixture [mol]; (Eq. 4.2)

P = Pressure [kPa]; (Eq. 4.7)

P_i = Partial pressure of individual component [kPa]; (Eq. 4.2)

P_m = Partial pressure of fuel/air mixture [kPa]; (Eq. 4.2)

P_{SL} = Total precision uncertainty [cm/s]; (Eq. B.2)

P_v = Vapor pressure [Torr]; (Eq. 4.8)

R = Specific constant of dry air [kJ/(kg.K)]; (Eq. 4.7)

r = Flame's radius [mm]; (Eq. 3.2)

r_u = Flame's radius (for unburned gases) [mm]; (Eq. 3.4)

r_{sch} = Flame's radius (measured by Schlieren photographs) [mm]; (Eq. 3.4)

S_b^0 = Unstretched laminar flame speed [cm/s]; (Eq. 3.1)

S_b = Stretched laminar flame speed [cm/s]; (Eq. 3.1)

T = Temperature [K]; (Eq. 4.7)

T_m = Temperature of the fuel/air mixture [K]; (Eq. 4.1)

t = time [s]; (Eq. 3.2)

U_{SL} = Total uncertainty [cm/s]; (Eq. B.4)

u_l = Laminar burning velocity [cm/s]; (Eq. 3.8)

V = Volume [m^3]; (Eq. 4.7)

V_m = Volume of the fuel/air mixture [m^3]; (Eq. 4.1)

W_{air} = Molecular weight of air [g/mol]; (Eq. 4.4)

W_f = Molecular weight of fuel [g/mol]; (Eq. 4.4)

GREEK SYMBOLS

α = Moles of carbon [mol]; (Eq. 4.6)

β = Moles of hydrogen [mol]; (Eq. 4.6)

γ = Moles of oxygen [mol]; (Eq. 4.6)

ϕ = Equivalence ratio (Eq. 4.3)

δ_l = Flame thickness [mm]; (Eq. 3.4)

ρ_b = Density of burned gases [kg/m^3]; (Eq. 3.8)

ρ_u = Density of fresh gases [kg/m^3]; (Eq. 3.8)

Chapter 1 – Introduction

Serious concerns have arisen today in the energy sector, based on the fact that gas emissions generated by current transportation systems and industrial applications are deteriorating the environment by generating pollutant contaminants and greenhouse effects [1]. Moreover, fuel supply sustainability has raised awareness due to the fact that demand for petroleum fuel tends to increase mainly owing to transportation growth. In addition, oil exploration tends to be concentrated in remote areas of difficult access which adds to the production and transportation cost of hydrocarbons fuels. Consequently, novel fuels sources should be explored, developed and implemented in combustion-powered systems like car engines, aircraft turbines and industrial burners in order to ease the complete reliance on petroleum based fuels [2, 3].

Different liquid fuel sources have been proposed as feasible candidates to replace petroleum based ones such as vegetable oils methyl and ethyl esters commonly referred to as biodiesel. This fuel can be a viable substitute to diesel fuels usually applied in compression ignition engines. In addition, oxygenated fuels (e.g. ethanol and methanol) are commonly used to power spark ignition engines at blended conditions and synthetic paraffinic kerosene (SPK) for fueling aviation engines [1, 2]. Moreover, several gaseous alternative fuels among which may be listed biogas (CH_4 and CO_2), syngas (H_2 and CO_2) and methane enriched with hydrogen have also been suggested as viable alternatives [8].

In particular, biodiesel has shown to be a sustainable and environment friendly source of energy for the transportation and aerospace sectors owing to its excellent features

which include the absence of additional emission of CO_2 gases to the atmosphere, its low sulfur content, and also its impact on the economy in generating jobs, increasing income taxes, and power other related economic activities such as agriculture [2]. However, biodiesel has also certain drawbacks such as its relatively slightly lower energetic power and torque and hence higher fuel consumption, which forces further research efforts on the improvement of these kind of fuels and the feasibility of their blends with conventional fuels as diesel or gasoline [1]. In addition, biodiesel has poor performance in cold flow environment due mainly to the precipitation of fatty acid methyl esters (FAME) made from saturated fatty acid chains. Oxidative instability is another additional problem of biodiesel fuels [4, 5]. Therefore, numerous research attempts have been devoted to develop fuel additives that can be blended with biodiesel to improve its overall properties and hence its combustion performance under cold weather conditions [5, 6, 7].

The properties and behavior of combustible fuels are influenced by their chemical composition. Understanding the chemical kinetics involved in the combustion reactions generated by these fuels is essential to evaluate their feasibility for real combustion applications [10, 11]. For instance, knowledge about laminar flame speed is important for the design of combustion systems. For example, it is highly needed for the validation of the fuel kinetic mechanisms [11]. Furthermore, laminar flame speed has great impact on engine power output, performance and pollutant emissions as this property provides an indication of the reactivity of a given fuel [9, 20]. In addition to the flame speed, other properties (e.g., evaporation rate, calorific value, minimum ignition energy and viscosity, etc) are key parameters for designing and optimization of combustion systems [46]. Accordingly, measurement of laminar flame speed at realistic engine conditions of temperature, pressure

and equivalence ratio are essential for engine performances and contaminant emissions [47].

Therefore the main objective of the present work was to determine experimentally the laminar flame speed of a novel renewable liquid fuel which is intended to be used as additive to biodiesel or a stand-alone fuel. This renewable liquid fuel was developed in Drs. Levin and Sorensen's research labs at the University of Manitoba as part of a collaborative research project sponsored by BioFuelNet Canada. It was also part of the objectives of this thesis to develop and validate an optical imaging technique in order to determine experimentally laminar flame speed.

The thesis is organized as follows. After this brief introduction, a literature review summary on the different published attempts for determining laminar flame speed of biodiesel and blends is provided in chapter 2. A summary of the different methodologies for measuring flame speed is given in chapter 3, followed by chapter 4 which is dedicated to describe the experimental setup employed in the research of this thesis. Results are provided in chapter 5, and finally conclusions and recommendations are summarized in chapter 6.

Chapter 2 - Literature Review

2.1 Introduction

A summary of published databases on biodiesels and proposed surrogates is presented in the following sections. Both numerical and experimental studies are compiled for both pure and blended fuel conditions, respectively.

2.2 Laminar flame speed of pure biofuels

Literature on laminar flame speed of pure biodiesel fuels is very scarce. Published numerical and experimental studies on biodiesel surrogates are summarized below. In addition, other oxygenated fuel candidates based on methyl ether structures as well as some alcohol fuels are also reviewed here.

2.2.1 Numerical investigations

Biodiesel is chemically composed of long alkyl chain structures attached to methyl esters originated from vegetable and animal oils, which can be characterized by simple fuels named surrogates [10, 11]. In order to appropriately select the suitable surrogate for a given multicomponent fuel (e.g., gasoline, diesel, biodiesel), certain criteria have been suggested, which basically accounts for the H/C ratio, heat of combustion and the ignition quality (e.g. cetane or octane number) as the most important [10]. Based on this selection, a complete review of these biodiesel surrogates is presented by Coniglio et al. [12], who reported a wide range of alkyl ester surrogates and a detailed list of their numerical

simulations. Databases on laminar flame speed of these surrogates are only available for some methyl fuels (e.g. butanoate, decanoate, crotonate) and ethyl pentanoate.

Wang et al. [14] reported a numerical simulation based on counterflow jet configuration to determine laminar flame speed of some biodiesel surrogates such as methyl butanoate ($C_5H_{10}O_2$), methyl crotonate ($C_5H_8O_2$) and methyl decanoate ($C_{11}H_{22}O_2$) flames at atmospheric pressure and 403 K. In this study, five different methyl butanoate kinetic models where simulated using a Fortran-based code denominated PREMIX which models steady planar laminar flames based in counterflow jet technique and integrated in a Fortran-based package called CHEMKIN [59]. Peak laminar flame speed ranged between 60 cm/s and 68 cm/s at equivalence ratios between 1.05 and 1.2 [14].

In addition, a few research teams have also studied methyl butanoate flames at different conditions of pressure and temperature. For instance, Liu et al. [15] used PREMIX and CHEMKIN packages to simulate methyl butanoate, n-butane and iso-butane spherical flames at pressures ranging between 1 and 2 bar, 353 K and equivalence ratios between 0.7 and 1.6. In this investigation, laminar flame speed results were lower at both pressure conditions, peaking at 50 cm/s and 43 cm/s at 1 bar and 2 bar, respectively, and over predicting experimental data by about 8 cm/s in both cases. Golovitchev and Yang [16] and Dooley et al. [17] reported numerically the flame speed of methyl butanoate at atmospheric pressure and different initial temperatures ranging between 298 K and 403 K. Golovitchev and Yang [16] developed an existing methyl butanoate mechanism to represent the combustion model of rapeseed methyl ester ($C_{19}H_{34}O_2$) by using the KIVA-3V code and found similar laminar flame speed data to the one reported by Liu et al. [15]. Dooley et al. [17] applied both a simplified and detailed n-heptane/methyl butanoate mechanisms to

explore the effects of temperature on different combustion properties including the laminar flame speed.

Another remarkable biodiesel surrogate is methyl decanoate ($C_{11}H_{22}O_2$), which is a promising fuel that resembles biodiesel and has very similar properties (e.g., reactivity and ignition delay) as methyl butanoate [11]. One of the attempts to simulate this fuel was reported by Alviso et al. [18], who developed two different modeling schemes based in the counterflow jet configuration at a temperature up to 400 K and equivalence ratios ranging between 0.7 and 1.5. They obtained higher laminar flame speed values compared to that of methyl butanoate. They also reported substantial differences between both schemes as laminar flame speed differs by about 10 cm/s, 5 cm/s and an average 3 cm/s between both schemes at stoichiometric, lean and rich conditions, respectively. Dievart et al. [19], in a numerical simulation based on a counterflow jet configuration at 1 bar and 403 K, reported similar laminar flame speed to Alviso et al. [18], where only a maximum of 10% divergence was observed between both databases.

2.2.2 Experimental investigations

Wang et al. [14] measured experimentally the laminar flame speed of 3 different methyl ester fuels of butanoate, crotonate and decanoate by analyzing the velocity profile generated in a counterflow jet configuration at 1 bar and 403 K. They found 5% scatter between their numerical and experimental results of methyl butanoate (MB) at lean condition but very good agreement for methyl crotonate (MC) and methyl decanoate (MD). Liu et al. [15] measured laminar flame speed of methyl butanoate/air mixtures at pressures ranging between 1 and 2 bar and 353 K, and found a 20% difference from that of Wang et

al. [14], caused probably by the difference in the temperatures of their respective experiments. Rotavera et al. [22] measured laminar flame speed of methyl octanoate (MO) and methyl cyclohexane (MCH) at 1 bar and 443 K, and found slight higher velocities than the ones reported by Wang et al. [14] and Liu et al. [15]. A review of the laminar flame speed of these fuel surrogates is shown in Fig. 2.1.

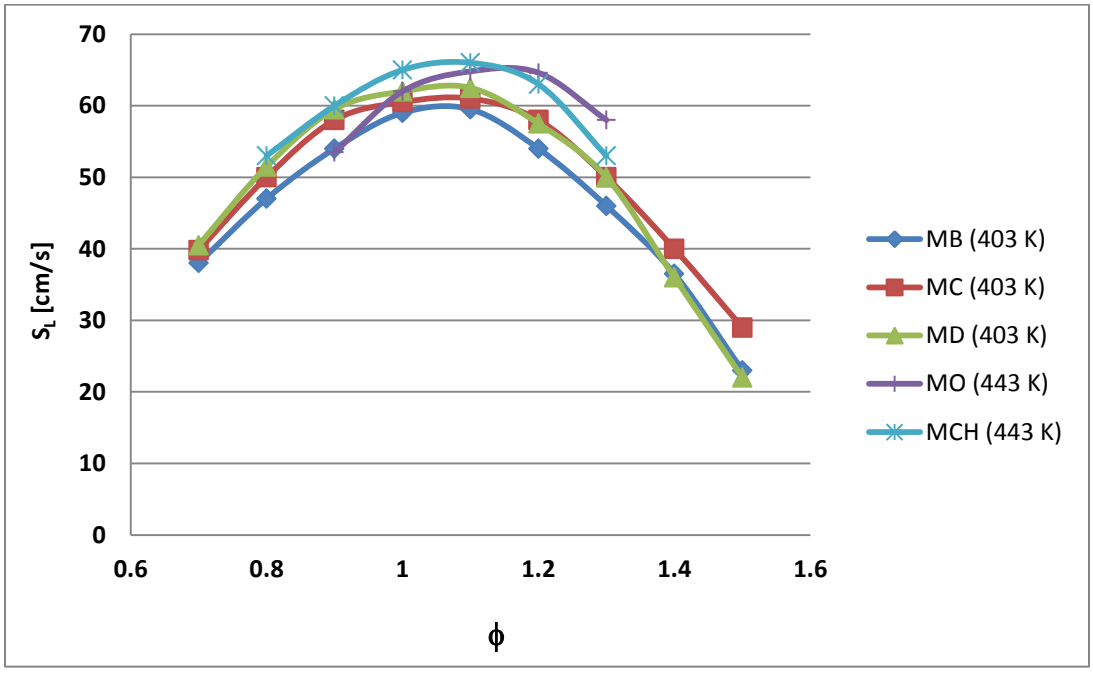

Figure 2.1. Laminar flame speed of oxygenated fuel surrogates (1 bar)

A very promising alternative biofuel is dimethyl ether (DME), which is a light oxygenated ether originated from the steam reforming of methane and the dehydration of the obtained methanol into dimethyl ether [13, 26]. Numerous research teams have devoted efforts in testing the laminar flame speed of DME [23, 24, 25, 26, 27, 28] owing to its remarkable combustion characteristics such as, for example, comparable ignition properties to diesel fuels (cetane number: 55) as well as only a slightly lower heating value to diesel

and gasoline but higher than ethanol [13]. As its chemical structure lacks C-C bond and sulfur content, no soot generation as well as low NO_x and CO emissions are expected, so it is a highly clean alternative fuel [25].

The experimental databases obtained by several research teams on dimethyl ether are based mainly on spherical flames, except the investigation developed by Zhao et al. [23], who measured laminar flame speed using planar flames of pure and diluted dimethyl ether (15% N_2) with a stagnation flame burner configuration, where a gas flow was impinged onto a silica foam flat plate at atmospheric pressure and room temperature, and equivalence ratio ranging between 0.8 and 1.4. Their laminar flame speed of dimethyl ether/air mixtures were found in agreement with that of biodiesel surrogates. The peak flame speed was obtained at equivalence ratios near 1.2 for pure and N_2 diluted dimethyl ether. The nitrogen dilution led to a decrease in the flame speed by approximately 5 cm/s at equivalence ratios between 1 and 1.4. They reported that nitrogen dilution at fuel lean condition had little effect on the laminar flame speed.

In a similar way, Qin and Ju [24] measured the laminar flame speed of dimethyl ether/air mixtures of outwardly-propagating spherical flames at different pressures up to 10 bar and 298 K. Their flame speed showed a certain scatter similar to that reported by Zhao et al. [23]. They [24] assessed the effect of pressure on laminar flame speed and flame structure and confirmed a decreasing trend of laminar flame speed as pressure increased. They also reported that flame instabilities were evident as pressure was increased, as for instance the formation of cellular structures at 6 bar.

De Vries et al. [25] also measured the laminar flame speed of dimethyl ether/air mixtures at pressures up to 10 bar, and found a similar decreasing trend in laminar flame speed with increased pressure, which is in accordance with the experimental data reported by Qin and Ju [24]. De Vries et al. [25] reported a comparative graph of the flame speed measurements obtained by with previously published data on dimethyl ether/air mixtures [23, 24, 25, 26, 27, 28] and showed substantial scatter especially at fuel-rich conditions and also flame speed peak (i.e., the highest value) was found at equivalence ratio close to 1.1.

Laminar flame speed of dimethyl ether/air mixtures were also reported by Daly et al. [26], Huang et al. [27] and Chen et al. [28], who measured outwardly-propagating spherical flames generated in combustion vessels. Their data showed close agreement as a function of equivalence ratio and stretch rate. Huang et al. [27] reported flame speed at different stretch rates for different equivalence ratios between 0.8 and 1.2, Chen et al. [28] accounted for the effects of dilution of CO_2 and N_2 on flame speed as a function of stretch rate.

As a way to compare methyl ester with conventional fuels, Chong and Hochgreb [29] measured flame speed of palm-methyl esters and compared it with Jet-A1 and diesel using a jet-wall stagnation configuration at atmospheric pressure and 470 K. They found substantially higher flame speed compared with the measurements of biodiesel surrogates studied by Wang et al. [14]. They [29] found as expected that Jet-A1 showed higher laminar flame speed than that of palm-methyl fuel, and diesel showed noticeably lower flame speed than that of palm methyl ester at lean conditions but slightly higher at rich conditions.

A recently developed biofuel named dimethylfuran, which is originated from the isomerization of glucose, is currently under investigation by several research groups owing to certain features of its properties such as higher energy density than ethanol, and high octane number and high levels of water absorption [31, 41]. A set of three different reports published experimental results on the outwardly-propagating spherical flames of these new generation biofuels. Tian et al. [30] measured laminar flame speed of 2,5 dimethylfuran (DMF) and compared with gasoline and ethanol. They found slight differences between gasoline and DMF and lower laminar flame speed than that of ethanol at three different initial temperatures. Wu et al. [31] reported experimental results at 393 K at different dilution levels of N_2 and CO_2 ranging between 5% and 15%. More recently, Ma et al. [32] performed measurements of 2 methylfuran and isooctane blend at three different temperatures between 333 K and 393 K, and found flame instabilities when isooctane was blended with DMF in comparison to pure isooctane but more stable flames than pure DMF. They measured higher flame speed as temperature increased.

In order to summarize the available literature on laminar flame speed of pure biofuels, a complete compilation of all explored fuels is presented in Table 2.1, where the different conditions of pressure, temperature, equivalence ratio and methodologies are also provided.

Fuel	ϕ	P [bar]	T [K]	Type of study	Type of flame	Regime	Ref
Methyl esters (butanoate, crotonate and decanoate)	0.7-1.5	1	403	Numerical Experimental	Counterflow planar	Laminar	[14]
Methyl butanoate, n-butanol, iso-butanol	0.7-1.4	1-2	353	Numerical Experimental	Spherical	Laminar	[15]
Methyl butanoate	0.4-1.7	1	298-323	Numerical	Spherical	Laminar	[16]
Methyl butanoate	0.7-1.5	1	333-353	Numerical	Stagnant planar	Laminar	[17]
Methyl decanoate	0.7-1.5	1	300-400	Numerical	Counterflow planar	Laminar	[18]
Methyl decanoate	0.6-1.5	1	403	Numerical	Counterflow planar	Laminar	[19]
n-butane/ dimethyl ether	0.7-1.7	1	300	Numerical Experimental	Spherical	Laminar	[20]
Ethyl pentanoate	0.7-1.4	1-10	423	Numerical Experimental	Jet stirred reactor	Laminar	[21]
Methyl octanoate, methyl cyclohexane	0.8-1.3	1	443	Experimental	Spherical	Laminar	[22]
Dimethyl ether	0.7-1.6	1	298	Experimental	Stagnant planar	Laminar	[23]
Dimethyl ether	0.6-1.4	1-10	295	Experimental	Spherical	Laminar	[24]
Dimethyl ether	0.7-1.6	1-10	298	Experimental	Spherical	Laminar	[25]
Dimethyl ether	0.7-1.7	1	295	Experimental	Spherical	Laminar	[26]
Dimethyl ether	0.7-1.7	0.8-1.5	285	Experimental	Spherical	Laminar	[27]
Dimethyl ether	0.7-1.7	0.97	293	Experimental	Spherical	Laminar	[28]
Palm methyl ester	0.7-1.4	1	470	Experimental	Stagnant planar	Laminar	[29]
2,5 Dimethylfuran	0.6-2.0	1	323-373	Experimental	Spherical	Laminar	[30]
2,5 Dimethylfuran	0.9-1.5	1	393	Experimental	Spherical	Laminar	[31]
2 Methylfuran	0.7-1.4	1	333-393	Experimental	Spherical	Laminar	[32]
Ethanol	0.6-1.5	1	298-358	Numerical Experimental	Planar-heat flux method	Laminar	[34]
Ethanol, Methanol	0.7-1.5	1	298-358	Experimental	Planar-heat flux method	Laminar	[35]

Table 2.1 Summary of published test conditions adopted for determining (experimentally or/and numerically) laminar flame speed of pure biofuels

2.3 Flame speed of biofuel blends

A promising strategy to develop alternative fuels is the combination of two or more combustibles or their surrogates, due to the possibility of taking advantage of particular properties of each component in a suitable mixture for a given application (e.g., internal or compression ignition engines, jet engines). In this section, a summary of numerical and experimental investigations on laminar flame speed of biofuel blends is presented.

2.3.1 Numerical investigations

Numerical studies on laminar flame speed of biofuels blends are basically focused on dimethyl ether fuels blended with some alkane fuels (e.g. methane and butane) and also syngas/dimethyl ether mixtures. The remarkable ignition properties of dimethyl ether and butane fuels (high cetane and octane numbers respectively) make them suitable for charge compression ignition engines (HCCI) [20, 33]. In order to examine dimethyl ether/butane blends, Wu et al. [20] conducted a numerical study where 3 different kinetic models were used to characterize dimethyl ether. The effect of temperature (between 300 K and 400 K), pressure (between 1 bar and 7 bar) and N_2 dilution (up to 30%) were all explored using PREMIX and CHEMKIN software packages [59]. They concluded that dimethyl addition to butane tends to increase laminar flame speed, with a stronger effect at stoichiometric and fuel rich conditions, with this tendency remaining constant at any pressure and temperature levels.

The beneficial effects of dimethyl ether dilution by alkane fuels is confirmed by the numerical investigations reported by Yu et al. [42] and Lowry et al. [43] who simulated dimethyl ether/methane blends at different conditions of pressure and temperature. In the

work reported by Yu et al. [42], four different blends were simulated at temperatures ranging between 303 K and 453 K and at pressures up to 7 bar. Similar to the conclusion obtained by Wu et al. [20], dimethyl ether addition showed a stronger increasing effect of laminar flame speed at fuel rich conditions [42]. In the numerical dataset reported by Lowry et al. [43], two different dimethyl ether/methane blends (60% and 80% DME) were simulated at room temperature and different pressures up to 10 bar. They also investigated flame stability based on the chemical composition of the blend and determined the flame critical radius at difference equivalence ratios ranging between 0.7 and 1.3 of each component and a 60/40 CH_4-DME blend. Accordingly, they reported that flame stability tends to increase as dimethyl ether is added to CH_4 where flame radius shows higher values when dimethyl ether concentration is higher.

The numerical predictions of laminar flame speed of syngas/dimethyl ether blends developed by Song et al. [44], where three different blends at room temperature and atmospheric conditions were considered, revealed a strong effect of syngas addition on flame speed as well as the increasing of flame stability as dimethyl ether is added to syngas mixtures.

2.3.2 Experimental investigations

In recent years, different biofuel blends have been suggested as suitable candidates as possible additives to enhance certain fuel properties where several options have been suggested by different investigators. Tat and Van Gerpen [38, 39] found a slight specific gravity increase of 7 % between pure diesel and biodiesel (constant at a temperature range between -20°C and 100°C), a strong blending effect on kinematic viscosity (about 40%) at

about 50°C, but weaker as temperature increased (about 30%) to 100°C, and a reduction of the lower heating value when biodiesel is blended with diesel (up to 12%) in comparison to pure biodiesel (B100) [40]. In a series of experiments performed by using the jet-wall stagnation configuration, Chong and Hochgreb [29] measured the laminar flame speed in a couple of binary blends based on diesel-biodiesel/air and Jet A1-biodiesel/air blends, where each fuel was tested at pure conditions and at 10%, 20% and 50% biodiesel concentration. Experimental results showed that laminar flame speed of diesel/biodiesel blends tend to decrease by about 7% at lean conditions, but increased up to 5% at rich conditions when B0 and B50 results were compared. In a similar way, Jet A1/biodiesel blends registered a stronger laminar flame speed reduction (around 13%) at lean conditions, but the flame speed increased (by about 10%) at rich conditions when Jet A1 and Jet A1/biodiesel were tested.

A viable fuel candidate for spark ignition engines is based on methylfuran/isooctane blends owing to its remarkable ignition properties (characterized by a similar octane number similar to gasoline), as well as a comparable heating value to isooctane [31, 32]. Experimental results have been reported for dimethylfuran/isooctane binary blends; for example, Ma et al. [32] tested pure isooctane, methylfuran, MF20 and MF50 at temperatures ranging between 333 K and 363 K. According to their experimental work, methylfuran showed higher laminar flame speed values (about 26%) than pure isooctane. They also tested a 20/80 methylfuran/isooctane blend (MF20) and a 50/50 methylfuran-isooctane blend (MF50), and found a stronger effect of methylfuran on isooctane at rich conditions when MF20 blend was considered but weaker as compared to the lean fuel conditions in a MF50 blend. Further experimental results were provided by Wu et al. [46],

who measured the laminar flame speed of a 2.5 dimethylfuran/isooctane blend (20/80), at different pressure (1 bar to 5 bar) and temperature conditions (393 K – 473 K). Their results were found to contradict the increasing trend of laminar flame speed as methylfuran is added to isooctane as claimed by Ma et al. [32] at equivalence ratios lower than 1.2, which could be caused by differences in the fuel chemical compositions.

Yu et al. [42] performed flame speed measurements of dimethyl ether/methane mixtures at atmospheric pressure, 303 K, and equivalence ratios ranging between 0.6 and 1.6. Based on the observations of the obtained results, an increasing effect on laminar flame speed by dimethyl blending on methane at any equivalence ratio was observed, however its effects were more significant at fuel rich conditions (ϕ >1.2) than at lean conditions. Similar results were found by Lowry et al. [43], who reported similarly a stronger increase in the flame speed as dimethyl ether was blended with methane. The experimental data obtained by Wu et al. [20], which in contrast with to the aforementioned dimethyl-alkane blends [42, 43], showed that in general, alkane fuels blended with dimethyl ether tend to strongly decrease flame speed for the initial alkane addition (up to 20%) and its impact is stronger at fuel rich conditions.

The experimental validation of the numerical results on the dimethyl ether/syngas blends was conducted by Song and et al. [44]. In their investigation, different syngas concentrations were blended with dimethyl ether at 298 K and pressures up to 3 bar. They reported that an increasing trend of the flame speed as syngas is added to the blend, which in this case corresponds to a 50/50 H_2/CO syngas fuel, especially at rich conditions. Furthermore, their experimental findings demonstrated that a higher syngas concentration tends to peak laminar flame speed at higher equivalence ratio, varying from 1.1 to 1.2 when

syngas addition was increased from 25% to 75% in volume. Flame instabilities are also evident as pressure is increased at fuel lean conditions.

Alternative biofuels for the aerospace industry have been also explored by a few research groups. For example, Munzar et al. [45] measured the laminar flame speed of a novel biojet fuel called SPK (Synthetic Paraffinic Kerosene), which is essentially an alternative fuel obtained from the hydrotreatment of camelina oils. They used the stagnation flame configuration at atmospheric pressure and 400 K for three different blends. The experimental results of laminar flame speed of SPK/Jet A1 blend led to conclude that this novel synthetic paraffin is comparable to Jet A1 fuel in terms of laminar flame speed over the entire range of equivalence ratios, ranging between 0.7 and 1.3.

Isooctane/alcohol mixtures were also presented as promising alternatives for spark ignition engines because alcohol fuels show close properties to gasoline (e.g. density, octane number and miscibility) [47]. Several research groups have claimed no significant engine change in addition to increased engine performance when alcohols are added to gasoline [36]. Thus, these blends have attracted the attention of several investigators who explored the laminar flame speed of isooctane (as main gasoline surrogate) blended with different alcohols. For instance, Sileghem et al. [35] measured the laminar flame speed of methanol and ethanol blended with isooctane at atmospheric pressure and at temperatures ranging between 298 K and 358 K, and concluded that alcohol addition to isooctane has a stronger effect at stoichiometric and fuel rich conditions. Further studies are provided by Broustail et al. [36, 37], who reported laminar flame speed measurements of ethanol/isooctane and butanol/isooctane blends at pressures up to 10 bar and temperatures up to 423 K using outwardly-propagating spherical flames. In general, Broustail and his

research team claimed higher laminar flame speed when ethanol was the additive element as compared to butanol, as well as a stronger effect of alcohol addition to isooctane at fuel lean conditions compared with the results obtained by Sileghem et al. [35]. This might be explained by the differences in the experimental methodologies applied by both research teams. Experimental validation of the results previously described on butanol/isooctane blends was provided by Zhang et al. [47], who employed different temperature conditions ranging between 353 K and 433 K and atmospheric pressure, and found a complete agreement with their numerical flame speed at any blend concentration over the entire range of equivalence ratios (0.8-1.5).

A summary published data on laminar flame speed of biofuel blends is compiled in Table 2.2. It is possible to observe that most research efforts have focused on exploring dimethyl ether as a promising element of feasible multicomponent fuels, which have been numerically and experimentally explored at a wide range of temperatures, pressures and equivalence ratios. In a similar way, the laminar flame speed of different alcohol fuels (e.g. methanol, ethanol) blended with isooctane have been extensively reported at realistic combustion conditions. On the other hand, investigations on flame speed of biodiesel blends and their surrogates have been barely investigated, which provides a wide field for future research in liquid fuels, as well as further investigation about other oxygenated fuels (e.g. mono-alkyl esters, methylfuran blends).

Base fuels	ϕ	P [bar]	T [K]	Type of study	Type of flame	Regime	Ref.
Palm methyl ester/diesel Palm methyl ester/Jet-A1	0.7-1.4	1	298-470	Experimental	Stagnant planar	Laminar	[29]
2 Methylfuran/isooctane	0.7-1.4	1	333-393	Experimental	Spherical	Laminar	[32]
2,5 Dimethylfuran/isooctane	0.9-1.5	1-5	393-473	Experimental	Spherical	Laminar	[46]
Dimethyl ether/n-butane	0.6-1.7	1	300	Numerical/ Experimental	Spherical	Laminar	[20]
Dimethyl ether/methane	0.7-1.4	1-10	298	Numerical/ Experimental	Spherical	Laminar	[43]
Dimethyl ether/methane	0.7-1.6	1-7	303-453	Numerical/ Experimental	Spherical	Laminar	[42]
Dimethyl ether/syngas	0.6-2.0	1-5	298	Numerical/ Experimental	Spherical	Laminar	[44]
Dimethyl ether/N2 or CO2	0.7-1.8	1	293	Experimental	Spherical	Laminar	[28]
SPK*/Jet A-1	0.7-1.3	1	400	Experimental	Stagnant planar	Laminar	[45]
Ethanol/isooctane Methanol/isooctane	0.7-1.3	1	338	Experimental	Planar-heat flux method	Laminar	[35]
Butanol/isooctane Ethanol/isooctane	0.8-1.4	1	400	Experimental	Spherical	Laminar	[36]
Butanol/isooctane Ethanol/isooctane	0.7-1.4	1-10	423	Experimental	Spherical	Laminar	[37]
Butanol/isooctane	0.8-1.5	1-10	353-433	Experimental	Spherical	Laminar	[47]

***** Synthetic Paraffinic Kerosene (SPK)

Table 2.2 Summary of published test conditions adopted for determining (experimentally and/or numerically) laminar flame speed of biofuel blends

2.4 Flammability of fuels

Flammability is a combustion property that accounts for the concentration of fuel in air at which a propagating flame can take place. In order to quantify the allowable fuel/air concentrations to obtain a propagating deflagration, two limits are defined: the minimum and maximum concentrations of fuel in the mixture, which are normally named lower flammability limit (LFL) and upper flammability limit (UFL), and usually expressed in volumetric percentage of fuel in the mixture [51]. Different experimental methodologies

have been reported by many research teams, which are mainly based in the experimental configuration and procedures proposed by the ASTM E-681 [48], to establish a visual criterion for successful flames. One of the approaches consisted of:

- A 5 L glass chamber enclosed in an external insulated vessel
- A fuel supply and heated air inlets
- A 15 kV output ignition system composed by two 1/8" tungsten electrodes
- A stirring device that generate a homogeneous fuel/air mixture

As a way to cover flammable mixtures at high pressure and temperature conditions, the ASTM E-918 standard [49] accounts for a pressure criterion, based on a 7% minimum pressure increase for successful propagating flames. This approach uses:

- A metallic closed vessel of 1 L internal volume
- A pressure rating of 3000 psi
- A spark ignition system
- Two pressure transducers to measure the fuel partial pressure and total pressure inside the vessel

The most complete compilation of published flammability limits of different liquids and gaseous fuels was provided by Zabetakis [50], who grouped a wide-range of substances by chemical type (e.g. alkanes, aromatics, alcohols, ethers, esters) and presented their lower and upper flammability limits. In general terms, this compilation concluded that carbon content (heavier hydrocarbon structures) tends to decrease their lower and upper flammability limits, in addition to narrowing the flammable range [50]. Furthermore, cyclic hydrocarbons (e.g. benzene, toluene) shows similar flammability limits as compared to

certain gasoline surrogates (e.g. n-heptane, isooctane). In addition, some alcohols and dimethyl ethers fuels showed wider flammable ranges as compared to light hydrocarbons (e.g. methane, ethane). Some ester compounds, which resemble some biodiesel surrogates (e.g. methyl butanoate, methyl crotonate, methyl decanoate), showed lower flammable range compared to methyl ether fuels but close to some light alkane fuels (e.g. propane, butane) [50].

More recently, Coronado et al. [51, 52] grouped the flammability limits of many hydrocarbons and oxygenated fuels. In addition, they provided further experimental data on flammability limits of ethanol for aeronautical applications at sub-atmospheric and atmospheric pressures. They employed two different criteria (visual inspection and pressure rise) for determining the flammability limits.

The temperature effect on the flammability limits of several alkanes, unsaturated hydrocarbons, dimethyl ether and other compounds were reported by Kondo et al. [53] at temperatures ranging between 273 K and 373 K. They concluded that the temperature rise tends to slightly increase the upper flammability limit but has no effect on the lower flammability limit of any tested fuel. Further contribution on flammability limits based on the ASTM E-681 was provided by the same research group [54], who provided numerical and experimental data on the flammability limits of some alkanes, cyclic and halogenated (e.g. Cl, Br, F) hydrocarbons. Zhang et al. [55] reported flammability limits of dimethyl ether diluted with 5 different gases and Mishra and Rahman [56] provided databases of LPG/air mixtures. Brooks and Crowl [57] employed the pressure criterion summarized in the ASTM E-918 to determine the flammability limit of oxygenated fuels and aromatic compounds (e.g. methanol, ethanol and toluene). Van der Shoor and Verplaetsen [58]

reported results on the upper flammability limits of lower alkanes (e.g. methane, propane) and alkenes (e.g. ethylene, propylene) at elevated pressures and temperatures. A compilation of the different fuels and their flammability limits is given in Table 2.3, where the lower and upper flammability limits are expressed in percentage in volume (% vol) of fuel in the fuel/air mixture, as signaled in the standard procedure [48].

Compound	**Formula**	**Group**	**LFL [% vol]**	**UFL [% vol]**	**Ref.**
Methane	CH_4	Paraffin hydrocarbons	5	15	[50]
Ethane	C_2H_6	Paraffin hydrocarbons	3	12.4	[50]
Propane	C_3H_8	Paraffin hydrocarbons	2.1	9.5	[50]
n-Butane	C_4H_{10}	Paraffin hydrocarbons	1.8	8.4	[50]
n-Heptane	C_7H_{16}	Paraffin hydrocarbons	1.05	6.7	[50]
n-Octane	C_8H_{18}	Paraffin hydrocarbons	1	6.5	[51]
n-Decane	$C_{10}H_{22}$	Paraffin hydrocarbons	0.75	5.6	[50]
n-Dodecane	$C_{12}H_{26}$	Paraffin hydrocarbons	0.6	-	[50]
Ethylene	C_2H_4	Unsaturated hydrocarbons	2.7	36	[50]
Propylene	C_3H_6	Unsaturated hydrocarbons	2.4	11	[50]
Isobutylene	C_4H_8	Unsaturated hydrocarbons	1.8	9.6	[50]
Benzene	C_6H_6	Aromatic hydrocarbons	1.3	7.9	[50]
Toluene	C_7H_8	Aromatic hydrocarbons	1.2	7.1	[50]
Methanol	CH_3OH	Alcohols	6.7	36	[50]
Ethanol	C_2H_5OH	Alcohols	3.3	19	[50]
n-Butyl alcohol	C_4H_9OH	Alcohols	1.7	12	[50]
Dimethyl ether	C_2H_6O	Ethers	3.4	27	[50]
Diethyl ether	$C_4H_{10}O$	Ethers	1.9	36	[50]
Methyl formate	$C_2H_4O_2$	Esters	5	23	[50]
Methyl acetate	$C_3H_6O_2$	Esters	3.2	16	[50]
Methyl propionate	$C_4H_8O_2$	Esters	2.4	13	[50]
Diesel (gas oil)	-	Multicomponent	0.5	5	[51]
Gasoline	-	Multicomponent	1.3-1.4	6.0-7.6	[51]
Kerosene	-	Multicomponent	0.7	5	[51]

Table 2.3 Flammability limits of some fuels and representative compounds

Chapter 3 – Methodology

3.1 Introduction

The flame speed is defined as the velocity of the flame front relative to the unburned mixture in a direction normal to its surface [61, 62]. In order to measure this combustion property, different methodologies and experimental configurations have been developed and reported in the literature. These include the outwardly-propagating spherical, conical flames methodology, the planar flames or jet wall stagnation method, the counterflow jet configuration, and the heat flux method. However, only the method based on the spherical flame is described here, as it is the one that is adopted in the present research. Nonetheless, advantages and disadvantages of these different methods are provided in the next section.

3.2 Advantages and disadvantages of laminar flame speed measurement methods

The measurement of laminar flame speed based on outwardly-propagating spherical flames generated in a closed combustion vessel is, so far, the most widely applied and well established methodology for measuring this property, owing to its ability to closely reproduce realistic conditions in spark ignition, compression ignition, or jet engines (e.g., high levels of pressure and temperature) [60, 61, 66, 67, 74]. Due to its wide application, a vast collection of numerical and experimental database is available in the literature for different fuels at a wide-range of temperature, pressure and equivalence ratio conditions [63, 75]. In addition to these benefits, this methodology enables the generation of homogeneous shaped flames than can be accurately processed with minimum fuel consumption as compared to other methods that require a continuous flow of fuel to generate measurable flames [74]. However, certain drawbacks have been claimed that are

associated with this method, such as the strict requirements to configure a complicated apparatus, complicated processing steps (e.g., linear or non-linear extrapolation, image post processing), instabilities and distortions in the flame shape due to buoyancy effects especially at high pressure, distortions at the ignition period as well as wall effects when the flame approaches the chamber walls [61].

Flame speed based on planar-shaped flames is a straightforward methodology to determine the laminar flame speed where the use of LDV or PIV enables a direct measurement without the application of further mathematical formulation (e.g., radius evolution, stretch rate, Markstein number). However, linear or nonlinear extrapolation must be applied to determine non-stretched laminar flame speed [76]. Furthermore, the quasi adiabatic character of the flame makes it as an attractive methodology to measure flame speed as the conductive heat loss downstream of the flame front is eliminated and the strain effects in the flame can be avoided. Add to this, planar and adiabatic flame which can be obtained using the idealized approximation of one dimensional flow [77]. The main drawback of this method is that the flame is prone to instabilities as planar flames are difficult to maintain if a steady flow of fuel/air mixture is not achieved. Additionally, this method does not accurately reproduce most realistic conditions such as high pressure and temperature, which limits its application.

The heat flux method is another approach to realize an idealized case of one dimensional adiabatic flame that overcome the inherent difficulties observed in a stagnation planar and counterflow-jet flames. This method is a direct measurement of flame speed at zero-stretch conditions which also avoids any extrapolation and uncertainties. However, the required experimental setup is complicated as a zero-net heat flux condition must be

obtained at the burner plate; therefore, an additional mechanism that enables the balance of the heat flux obtained from the flame to the burner should be configured (e.g., cooling system or perforated plates). Add the difficulties associated with the ability to successfully tune the gas mixture flow that guarantees a zero-heat flux condition at the burner. Similarly to planar flames obtained by the stagnation planar or the couterflow-jet configurations, the heat flux methodology requires a fully developed homogeneous flow of fuel/air mixture that ensures stable flames [78].

The experimental estimation of laminar flame speed based on conical shaped flames is the easiest/simplest methodology to measure flame speed as its experimental setup consist only of a nozzle-type burner and a premixed fuel/air mixture system that guarantee a constant and homogeneous flow through the burner. The main inconvenience of this method is the inaccuracy of the measurements caused by irregularities of the flame front, leading to a poor estimation of the flame angle and consequently a poor estimation of flame speed [79]. Furthermore, this methodology does not allow reproducing realistic test conditions of pressure and temperature.

In conclusion, the measurement of laminar flame speed based on outwardly-propagating spherical flames is the most suitable approach to obtain realistic databases for spark ignition or compression engines, where high pressure and temperature are characteristic. In contrast, the methodologies based on planar and conical flames are only appropriate at atmospheric pressure.

3.3. Outwardly-propagating spherical flames

Laminar flame speed based on outwardly-propagating spherical flame is, so far, the most applied methodology. This is owing to its suitability to closely reproduce realistic combustion conditions of high pressure and temperature; in addition to its ability for testing the entire flammability limit range and the potential to measure and analyze other parameters (e.g., stretch rate, flame instabilities and ignition characteristics) [61, 63, 64, 65, 66, 67, 68, 69, 70, 71, 72, 73]. This methodology is based on the formation of a spherical-centered flame in a combustion bomb (spherical or cylindrical-shaped) when a fuel/air mixture is ignited at the center of the combustion vessel. The flame propagation is measured by applying an optical technique that captures the deflagration at a fixed sampling rate [64, 65]. The mathematical formulation of laminar flame speed suggests a linear relation for flame stretch rate and Markstein length, where the laminar flame speed at both stretched and non-stretched conditions are summarized as follows [61, 66, 67]:

$$S_b = S_b^0 - L_b k \tag{3.1}$$

where k is the stretch rate and is defined as

$$k = \frac{2}{r}\frac{dr}{dt} \tag{3.2}$$

L_b is the Markstein length, r is the spherical flame radius, S_b^0 is the unstretched laminar flame speed and S_b is the stretched flame speed. This equation provides a thermo-kinetic model for the laminar flame speed because the second right hand term of Eq. 3.1 is composed of two elements: the Markstein length (L_b) which accounts for thermal effects of the flame and the stretch rate (k) that characterizes the geometrical expanding effects on the

propagation of the flame [68]. Experimentally, the laminar flame speed based on an outwardly-propagating flame is obtained by tracking the radius evolution during its propagation according to [69]:

$$S_b = \frac{dr_u}{dt} \tag{3.3}$$

where r_u is the radius of the flame front. A few studies reported the corrected flame radius by correlating the experimental radius samples to other associated parameters in the flame, following the following expression [65, 69]:

$$r_u = r_{sch} + 1.95\delta_l \left(\frac{\rho_u}{\rho_b}\right)^{0.5} \tag{3.4}$$

where r_{sch} is the flame radius obtained from the experimental data using an imaging technique, δ_l is the flame thickness, ρ_u and ρ_b are the densities of the unburned and the burned fuel/air mixture.

In order to obtain the flame radius history of Eq. 3.3, high speed camera photographs are obtained by applying certain imaging techniques (e.g. Schlieren or shadowgraphic photographs), as shown in Fig. 3.1. The application of these methodologies allows the visualization of density changes originated by a temperature gradient between the flame front of the spherical flame and the fresh unburned gases. The resultant circular edge originated by the spherical flame's projected area is captured, recorded and post processed by an image processing code that detects that edge and calculates the radius of the flame. The velocity of propagation corresponds to the rate at which the detected flame's radius change with time *(i.e., dr_u/dt)*, according to the sampling rate provided by the camera [66].

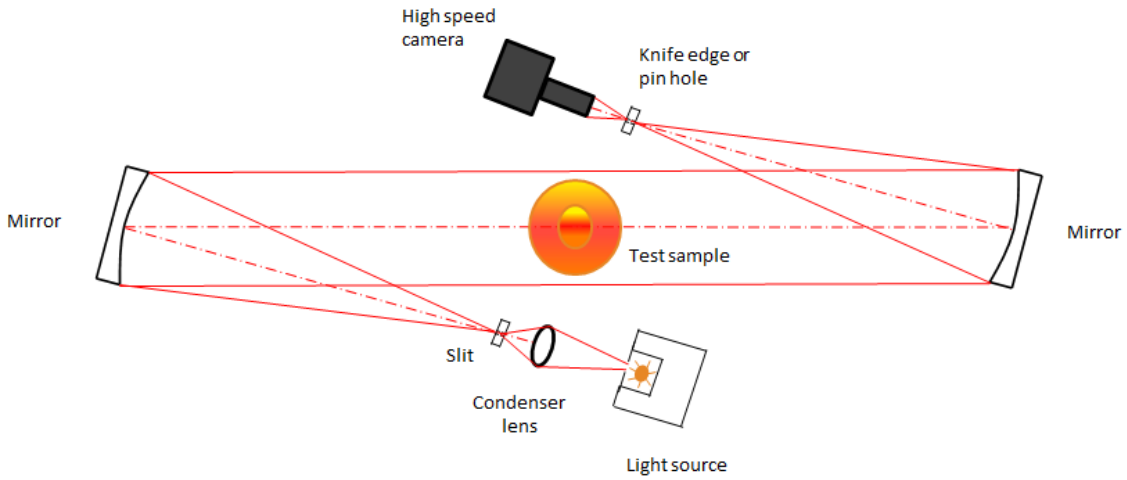

Figure 3.1. Z-type Schlieren configuration [80]

The laminar flame speed obtained by the analysis of the Schlieren photographs (Eq. 3.3) considers the stretch effects on the flame; that is, a velocity of the flame propagation that accounts for motion and curvature. As a way to quantify these effects, the laminar flame speed at zero stretch condition (S_b^0) is calculated by applying a linear extrapolation following what is expressed in Eq. 3.1 [66]. Even though the linear extrapolation has been demonstrated to be a reliable way to obtain the unstretched flame speed (S_b^0), several studies have developed non-linear methodologies as a more accurate way to obtain the flame speed at zero stretch conditions. For example, Kelley et al. [61, 70] performed a non-linear extrapolation of the laminar flame speed and obtained the following correlation:

$$\left(\frac{S_b}{S_b^0}\right)^2 ln\left(\frac{S_b}{S_b^0}\right)^2 = -2\frac{L_b}{S_b^0}k \qquad (3.5)$$

In their analysis they found three well-defined zones in the plot S_b vs k at which laminar flame speed behave differently. The first zone was obtained at stretch rate k < 150 s^{-1}, where the flame speed reduces due to wall effects; a second zone is obtained at stretch rate

150 s^{-1} < k < 235 s^{-1}, which is characterized by its quasi-steady flame speed behavior, and a third zone identified at k > 235 s^{-1}, where the initial ignition affects significantly the flame speed [70]. Additionally, other non-linear models have been suggested for the estimation of the laminar flame speed at zero stretch condition. For instance, Chen [64] developed a numerical analysis of the linear methodology expressed by Eq. 3.1 along with two alternative models that account for the Markstein length, as expressed in Eq. 3.6 and Eq. 3.7:

$$S_b = S_b^0 - S_b^0 L_b . \frac{2}{R_f} \tag{3.6}$$

$$ln(S_b) = ln(S_b^0) - S_b^0 L_b * \frac{2}{R_f} \tag{3.7}$$

In the first case, the stretched laminar flame speed S_b is linear to the flame curvature $2/R_f$, and consequently a linear extrapolation can be used to obtain the laminar flame speed at zero-stretch condition (S_b^0). In the second case, a non-linear relation between the stretched and non-stretched flame speeds developed.

Finally, the laminar burning speed (velocity) is the product of the ustretched laminar flame speed (S_b^0) and the density ratio of burned products (ρ_b) to fresh gaseous mixture (ρ_u) , which is expressed as follows:

$$u_l = S_b^0 \frac{\rho_b}{\rho_u} \tag{3.8}$$

Chapter 4 – Experimental Facility

4.1 Introduction

The experimental configuration to measure flame speed of different fuel/air mixtures is discussed in the present chapter. The complete setup is schematically shown in Figure 4.1. Only certain aspects of the spherical chamber are briefly mentioned here as it has already been described in [81, 82]. However, the other elements concerned with the measurement of flame speed including the imaging Schlieren technique are described in the following sections.

4.2 Spherical combustion chamber

The experimental setup for measuring the flame speed of the outwardly-propagating spherical flames consists mainly of a spherical combustion chamber which has been developed in the Energy and Combustion Laboratory (ECL) [81].

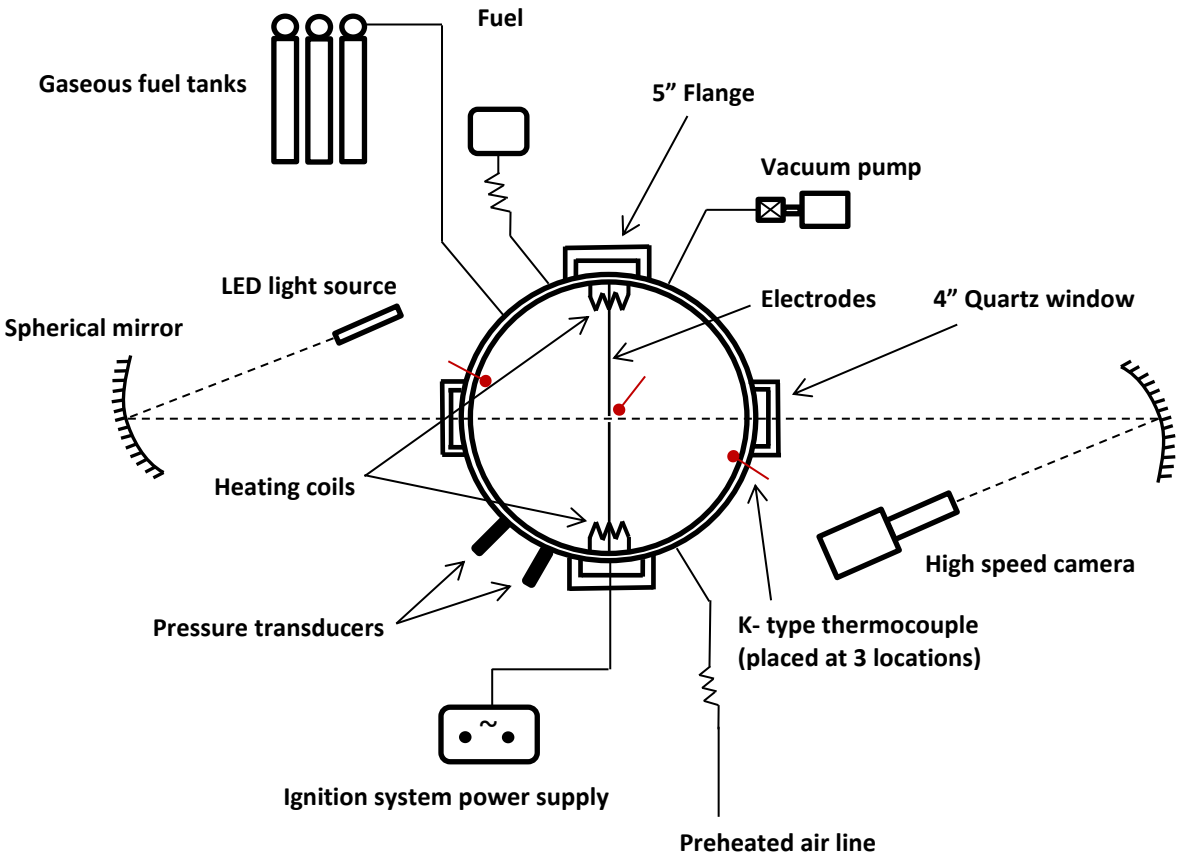

Figure 4.1. Schematic of the experimental setup

The spherical chamber, which was made of stainless steel, has an inner and outer diameter of 380 and 405 mm, respectively. It is equipped with 8 axial fans for the generation of isotropic homogeneous turbulence with zero-mean velocity and an anisotropy level less than 10% in the central region of the chamber [83]. In the present study, the fans are used only for stirring the fuel/air mixtures prior to ignition. Furthermore, the vessel is equipped with two pairs of visualization windows of 5” (127 mm) and 4” (101.6 mm) to provide optical access into the inside of the vessel. These two pairs of quartz windows are located at

90° from each other. In addition, the vessel is equipped with several ports, which can be summarized as follows [81]:

- Four main accessory ports with an inner diameter of 5/8” (15.875 mm) which are located 45° on the sphere’s equator line and separated at an angle of 90° between them. These ports have 2.5” (63.5 mm) outer threaded flanges.
- Four flanged sensor ports of 2.5” (63.5 mm) diameter that are located 67.5° above the equator line and 90° between each other.
- A 5/8” (15.875 mm) inner diameter port on the top of the chamber which has a 2.5” outer flange.
- A 5/8” (15.875 mm) exhaust port located in the bottom of the chamber, and has a 2.5” (63.5 mm) outer flange. This port is used for the drainage of any fluid or gas from the interior of the chamber.

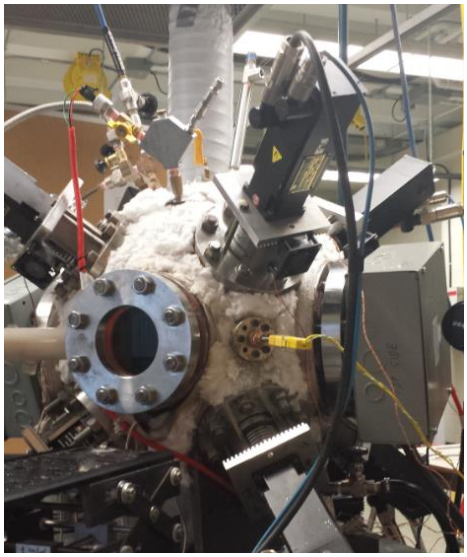

Figure 4.2. A photograph of the spherical combustion chamber

4.3 Fuel Supply System

In order to supply the correct amount of fuel to the combustion chamber, two different methodologies have been implemented: the fuel injection based on the partial pressure method and the volumetric method. A detailed description of each methodology and associated elements is discussed in the sub-sections below.

4.3.1 Fuel Injection by the partial pressure method

In order to generate an appropriate fuel/air mixture inside the combustion chamber, the Dalton's law of partial pressures (Eq. 4.1) and the ideal gas mixtures relation (Eq. 4.2) were applied to calculate the partial pressure of the fuel for a given fuel at different equivalence ratios [84]:

$$P_m = \sum_{i=1}^{k} P_i(T_m, V_m) \tag{4.1}$$

$$\frac{P_i}{P_m} = \frac{N_i}{N_m} \tag{4.2}$$

Where P_i is the partial pressure of the fuel and P_m is pressure of the mixture, N_i and N_m are the moles of the fuel and the mixture, T_m and V_m are the temperature and volume of the mixture.

In order to calculate the concentrations of all elements/components in the mixture, the ratio of fuel to air at both the actual combustion reaction and the theoretical chemical reaction must be determined. The parameter that accounts for these concentrations is named equivalence ratio (ϕ), which can be expressed as [85]:

$$\phi = \frac{\left({}^{m_F}/_{m_A}\right)_{actual}}{\left({}^{m_F}/_{m_A}\right)_{st}} \tag{4.3}$$

$$\left({}^{m_F}/_{m_A}\right)_{st} = \frac{\left(N_f . W_f\right)}{W_{air}\left((N_O . W_O)+3.76(N_N . W_N)\right)} \tag{4.4}$$

where m_F and m_A are the masses of fuel and air for the actual combustion reaction and the theoretical (stoichiometric) reaction, N_f, N_O, N_N are the moles of the fuel, oxygen and nitrogen respectively, and W_f, W_O, W_N are the molecular weights of the fuel components, oxygen and nitrogen respectively. In general, there are three different conditions for the equivalence ratio:

- $\phi = 1$ represents the theoretical (stoichiometric) chemical reaction
- $\phi < 1$ represents fuel lean conditions
- $\phi > 1$ represents fuel rich conditions

For combustion reactions different to the stoichiometric conditions, the ratio of partial pressures of the fuel and the mixture is given as:

$$\frac{P_f}{P_m} = \frac{N_f}{N_f + \frac{N_{air}}{\phi}} \tag{4.5}$$

As the partial pressure is of importance for a given fuel, the chemical reaction must be considered for determining the amount of moles in Eq. 4.4. In general, the chemical reaction of an oxygenated hydrocarbon is provided as [86]:

$$C_\alpha H_\beta O_\gamma + \left(\alpha + \frac{\beta}{4} - \frac{\gamma}{2}\right)(O_2 + 3.76N_2) \rightarrow \alpha CO_2 + \frac{\beta}{2} H_2O + 3.76\left(\alpha + \frac{\beta}{4} - \frac{\gamma}{2}\right) N_2 \tag{4.6}$$

For the present investigation, the fuels tested were methane, heptane and 1,3 dimethoxyoctane (DMO). A summary of these fuels with their associated chemical reaction is presented as follows:

- Methane (CH_4): $CH_4 + 2(O_2 + 3.76N_2) \rightarrow CO_2 + 2H_2O + 7.52N_2$
- Heptane (C_7H_{16}): $C_7H_{16} + 11(O_2 + 3.76N_2) \rightarrow 7CO_2 + 8H_2O + 41.36N_2$
- 1,3 DMO ($C_{10}H_{22}O_2$): $C_{10}H_{22}O_2 + 14.5(O_2 + 3.76N_2) \rightarrow 10CO_2 + 11H_2O + 54.52N_2$

The novel liquid biofuel was obtained from 1,3-octanediol, that was originated from methyl 3-hydroxyoctanoate reduced by sodium borohydride ($NaBH_4$). The substrate (1,3-octanediol) suspended in tetrahydrofuran (THF) was reacted with sodium hydride (NaH) and methyl iodile (CH_3I) to produce 95% pure 1,3 dimethoxyoctane. Further detail can be found in Birouk et al. [105].

In order to illustrate the mathematical procedure for calculating the amount of gaseous (or vapor) fuel required to generate a spherical flame, a methane/air mixture at p = 101.325 kPa, T = 298 K and ϕ = 0.8 is used here. The amount of fuel is calculated by applying Eq. 4.4 and 4.5 as follows:

$$\left({}^{m_F}/_{m_A}\right)_{st} = \frac{(1\,.12\,) + (4\,.1\,)}{2\big((2\,.16) + 3.76(2.14)\big)} \quad = \quad 0.05827$$

$$\frac{P_f}{P_m} = \frac{1}{1+\frac{2\ x\ 4.76}{0.8}} = 0.07752$$

The partial pressure of methane is:

$$P_f = 0.07752\ P_m = 0.07752 * 14.5 = 1.1238\ psi$$

A full collection of partial pressures of all tested fuels at different equivalence ratios and pressures is presented in table F.1 (Appendix F).

In order to accurately measure and control the pressure, the following sensors were selected and installed on the combustion chamber via a three way stainless steel manifold using ball valves for their protection from the combustion chamber when ignition occurs so that damage due to high pressure and temperature peaks can be prevented:

- A Kulite XTEL-190 pressure transducer rated at pressures between 0 and 5 psi with 0-10 VDC was connected to one of the manifold ports to measure the partial pressure of gaseous or vaporized liquid fuel at the selected equivalence ratio and mixture pressure (according to Table F.1).
- A P155-150G-E1A pressure transducer rated at pressures between 0 and 150 psi with 0-4.5 VDC was used through another manifold port to measure the mixture pressure (fuel partial pressure mixed with air), that is, the set pressure in the combustion chamber just before ignition

In order to inject liquid fuels, two small cylindrical vessels were configured so that liquid fuel can be deposited and then vaporized by heating its walls using an external heat source (wrap tape), as shown in Figure 4.4. In order to achieve this objective, liquid fuel is deposited inside the top storage vessel with a ball valve separating a lower closed vessel, where the liquid fuel is vaporized by the application of an external heat source provided by a heating tape. Once the vaporization chamber reaches a certain temperature, the chamber is vacuumed and the valve is open to allow liquid fuel flow into the vaporization chamber by the aid of gravity. Once the fuel is vaporized, a needle valve is opened to allow the fuel

vapor flow from the vaporization chamber to the vacuumed spherical chamber though a flexometallic hose until the fuel partial pressure for the selected equivalence ratio is reached. The main elements of the fuel supply system are shown in Figs. 4.4 and 4.5.

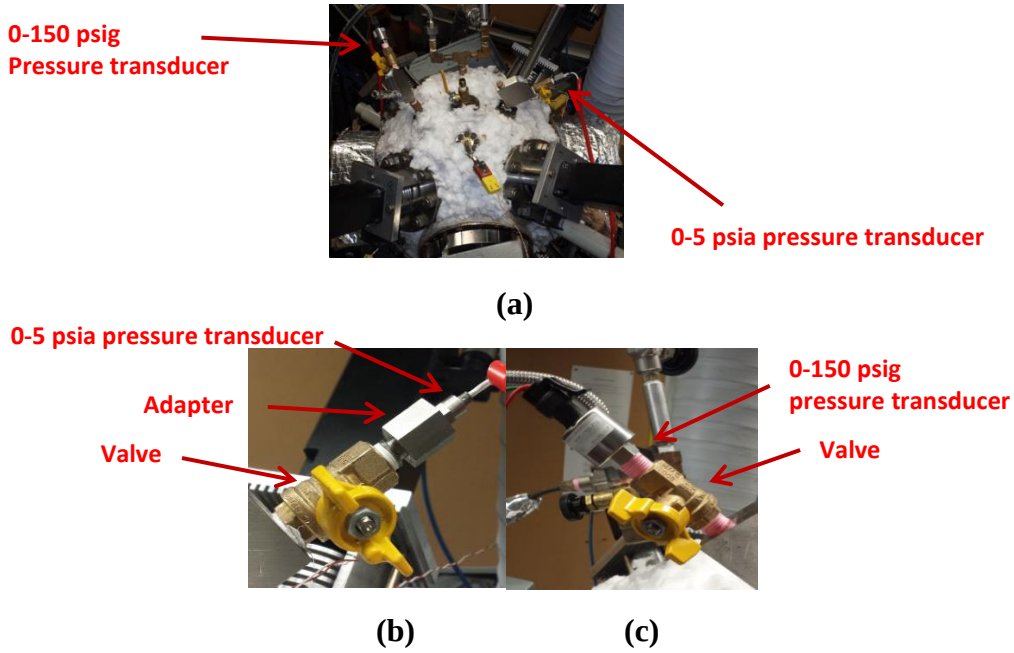

Figure 4.3. Pressure transducers

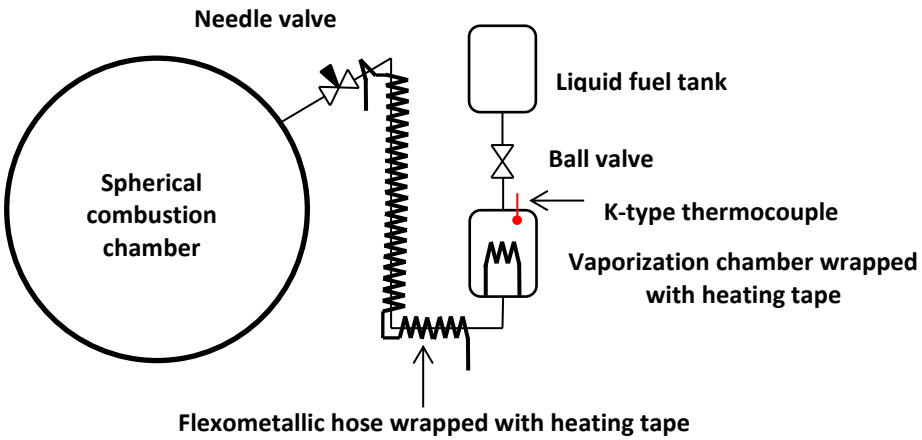

Figure 4.4. Schematic of the fuel supply system by the partial pressure methodology

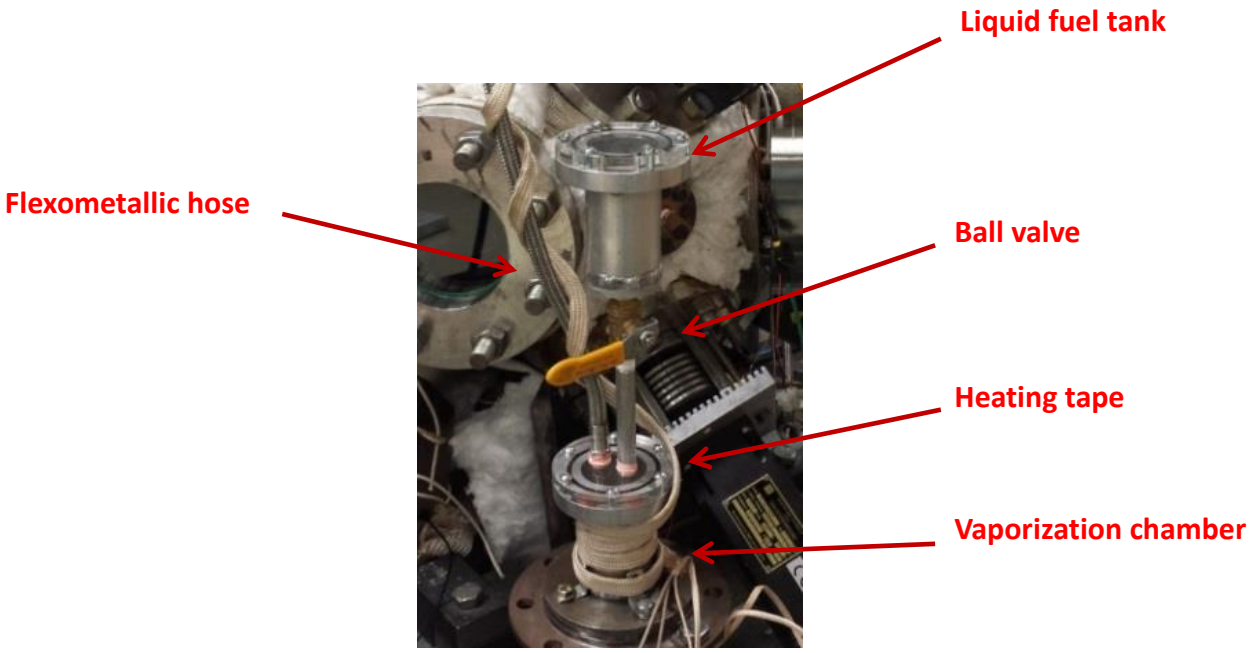

Figure 4.5. Photograph of the fuel supply system

4.3.2 Fuel Injection by the volumetric method

A second methodology was also implemented for liquid fuels. This method involves a direct injection of the liquid fuel directly into the combustion chamber through the top port using a 10 ml syringe (see Figures 4.6 and 4.7). Before injecting the liquid fuel, the corresponding air (based on using partial pressure) mass is first injected into the fully empty (vacuumed) chamber. The amount of liquid fuel injected must be measured so that only the exact amount that corresponds to the set equivalence ratio. Note that air injected into the chamber (prior to injecting the liquid fuel) is heated to a temperature at which the fuel vapor condensation can be prevented. Then, the air-fuel vapor mixture is stirred prior to ignition in order to ensure a completely homogeneous combustible mixture.

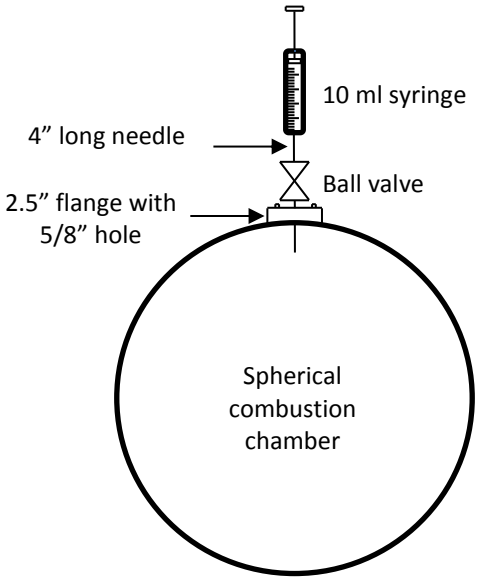

Figure 4.6. Schematic of the fuel supply system by the volumetric methodology

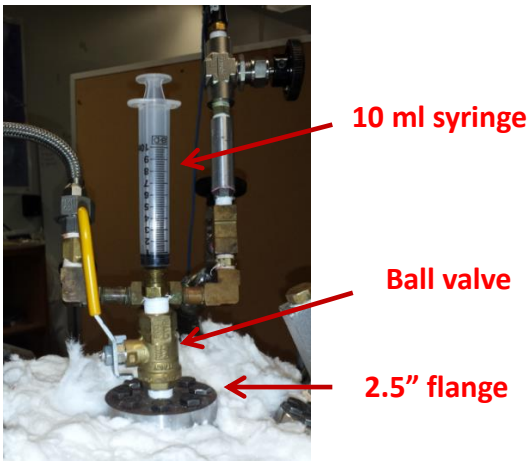

Figure 4.7. Photograph of the fuel supply system by the volumetric methodology

In order to calculate the fuel volume to be introduced at the set equivalence ratio and pressure, the ideal gas assumption is considered to estimate the required mass of air to fill the chamber as [84]:

$$m = \frac{PV}{RT} \quad (4.7)$$

To illustrate the mathematical procedure for determining the fuel volume at each test conditions, the required amount of heptane to generate an outwardly-propagating spherical flame at p=101.325 kPa, T=353 K and ϕ = 0.8 in an internal volume = 0.0287 m^3 is calculated as:

$$C_7H_{16} + 11(O_2 + 3.76N_2) \rightarrow 7CO_2 + 8H_2O + 41.36N_2$$

$$m_A = \frac{101.325 \text{ x } 0.0287}{0.287 \text{ x } 353} = 0.0287\ kg$$

In order to determine the amount of fuel mass, Eq. 4.3 and 4.4 are applied, taking into account the molecular weights of the different elements in the chemical reaction (given above) and the density of the fuel, which are summarized as:

- $W_C = 12\ g/mol$
- $W_O = 16\ g/mol$
- $W_N = 14\ g/mol$
- $\rho_{f,l}$ $\rho_{fuel,liquid}$ = 679.5 kg/m^3

$$\left({}^{m_F}/_{m_A}\right)_{st} = \frac{(7\,.12\,) + (16\,.1\,)}{11\big((2\,.16) + 3.76(2.\,14)\big)} = 0.06622$$

$$m_F = 0.06622 \text{ x } 0.8 \text{ x } 0.028 = 0.00152\ kg$$

$$V_f = \frac{m_f}{\rho_f} = \frac{0.00152\ kg}{679.5\ kg/m^3} = 2.237\text{x}10^{-6} m^3 = 2.237\ ml$$

The volumetric fuel employed at each equivalence ratio at a total pressure of 1 bar and different temperatures (see Table 4.1) is provided in Table F.2 (Appendix F).

	T [K]	ρ [kg/m³]
Heptane	353	679.5
1,3 DMO	423	825.95

Table 4.1. Fuel conditions

4.3.3 Vacuum system

A Busch PB 0004 B vacuum pump (Figure 4.8) is selected and purchased specifically for flame speed measurements. It is connected to one of the accessory ports of the combustion chamber, so vacuum can be induced inside the combustion chamber, allowing vaporized fuel to be injected inside it and then mixed with air to generate the appropriate mixture to be ignited. The main features of the vacuum pump are as follows:

- 4-4.8 m^3/h nominal suction capacity,
- 2 mbar ultimate capacity,
- 1.5 bar maximum allowable pressure,
- 0.1-0.12 nominal motor rating and
- 3000-3600 nominal speed.

Figure 4.8. Vacuum pump

In order to run an experiment, all the valves attached to the combustion chamber must be closed and all windows (4" and 5") must be appropriately tightened. After checking the lubricant level at the vacuum pump (visual inspection), the valve is opened and the pump is turned ON until the pressure reaches 3.0 psia (minimum allowable with the current pump), then, the valve is closed and the pump is turned OFF to carry out a 5-min vacuum test for verification of non-leakage condition at the chamber. A complete description of the operation of the vacuum pump is provided in section D.2.2 of Appendix D.

4.4 Combustion chamber pressure control

When flame speed measurements are performed at the set/initial pressures in a combustion bomb, the analysis of the flame propagation is carried out by assuming that the pressure during the experiment remains constant. In order to ensure that the pressure remains nearly constant once the fuel/air mixture ignites, three safety relief valves were selected and installed onto the combustion chamber. The valve was adjusted by setting a

target pressure at each valve and then verifying that the pressure relief at the combustion chamber corresponds to the pressure measured at the 0-150 psi pressure transducer. A complete description of the procedure is compiled in Appendix E.

The selected valves (Figure 4.9) for the present experiment were HY-LOK model RV1MF-4N-S316 that can be adjusted in a range of working pressures between 10-250 psig with an orifice of 0.19 in² (122.58 mm^2) and can operate as temperatures up to 204°C. As a way to afford higher operative temperatures, each relief valve was connected to a ¼" (6.35mm) x 8" (203.2 mm) length tubing that enable cooling the hot gases reaching the valves.

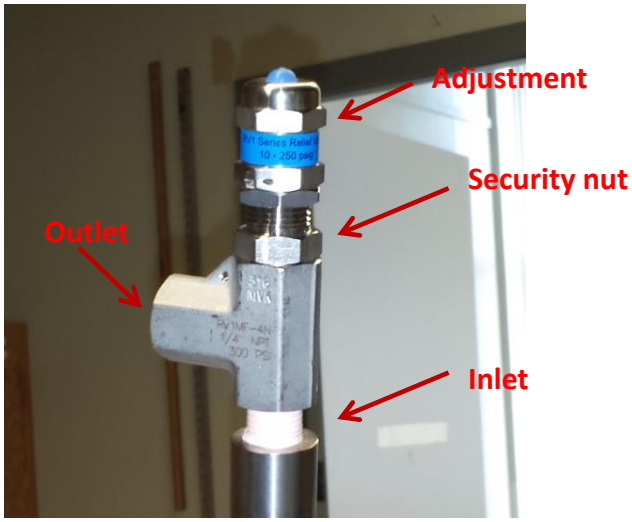

Figure 4.9. Relief valve

4.5 Heating system

Vaporization of the fuel is essential to generate a gaseous fuel/air mixture that can be ignited; then, a system that enables the vaporization of liquid fuels once the combustible is injected is required. In addition, condensation of vaporized fuel is a drawback during the

development of the experiments, then, the experimental setup must be configured to avoid this problem.

4.5.1 Fuel vaporization and condensation

Fuel vaporization for a liquid fuel depends on both pressure and temperature. In order to determine the temperature limit at which certain fuel changes from gaseous to liquid phase (that is, condenses), the Antoine equation which enables the correlation of temperature dependency on vapor pressure is expressed as [88]:

$$log(P_v) = A - \frac{B}{T+C} \quad (4.8)$$

Where P_v is the vapor pressure (in this case, the partial pressure of the fuel), T is the minimum temperature at which a liquid fuel vaporizes, A, B and C are experimental constants (see Table 4.2) that are specific for each substance. For the novel fuel (1, 3 DMO) constants were assumed as those of methyl octanoate ($C_9H_{18}O_2$) [22, 89, 90].

Fuel	A	B	C	Ref.
Methane (CH_4)	6.6956	405.42	267.777	[89]
n-Heptane (C_7H_{16})	6.8938	1264.37	216.63	[89]
1,3 DMO ($C_{10}H_{22}O_2$)	7.5703	1920.1	216.78	[22]

P [Torr], T[°C]

Table 4.2 Coefficients for the Antoine equation

As an illustrative example, the condensation temperature of 1,3 DMO is calculated at $\phi = 1.0$, which corresponds to a partial pressure of 0.2099 psi (10.86 Torr) is calculated using Eq. 4.8 as follows:

$$T = \frac{B}{A - log(P_v)} - C = \frac{1920.1}{7.5703 - log(10.86)} - 216.78$$

T = 77.063°C

A compilation of the different condensation temperatures is given in Table F.3 (Appendix F).

4.5.2 Heating coils

In order to prevent condensation of liquid fuel vapor, two heating-coil system was used on both optical windows of 5" (127 mm) of the combustion chamber [82]. A brief description of those system components, as shown in Figure 4.10, is provided as follows:

- A heating coil with 255 W power output with 0.246" (6.2484 mm) in diameter and 18" (457.2 mm) total length. It has a three-heating elements which are bent to increase the total heating surface. The system is powered from a 110 VAC electrical supply.
- A heating coil with 450 W power output with 0.375" (9.525 mm) diameter and 18" (457.2 mm) total length. It has three-heating elements which are bent to increase the total heating surface. It is powered from a 110 V electrical supply.
- Each heating coil is equipped with a heating control system which consists of a certified electrical box provided with a programmable digital controller (Omegaette CN4316-DC1-R2), a solid state with 24-280 VAC load power, and 3-32 VCD control voltage. Each controller is connected to a K thermocouple which monitors the gas temperature inside the chamber. The temperature of the gas is monitored in

the north and south sides of the combustion chamber in order to ensure the homogeneity of the temperature.

Figure 4.10. Heating coil

4.5.3 Vaporization chamber

As mentioned in section 4.3.1, the vaporization chamber requires an external heat source to vaporize the fuel, which is done by an ultrahigh temperature heating tape wrapping around the vaporization chamber and also the flexometallic hose connecting it to the combustion chamber, as shown in Fig. 4.11. The temperature is set by a manual temperature controller (Extech Instruments model 48 VFL) provided with a K-type thermocouple measuring the internal volume of the combustion chamber. Specifications of the heating tape include:

- Model: HTS Amptek ASR-051-060 DL
- Maximum operative temperature: 1400 F
- Power supply: 120 VAC
- Width: ½" (12.7 mm)

- Length: 6 ft (1.828 mm)

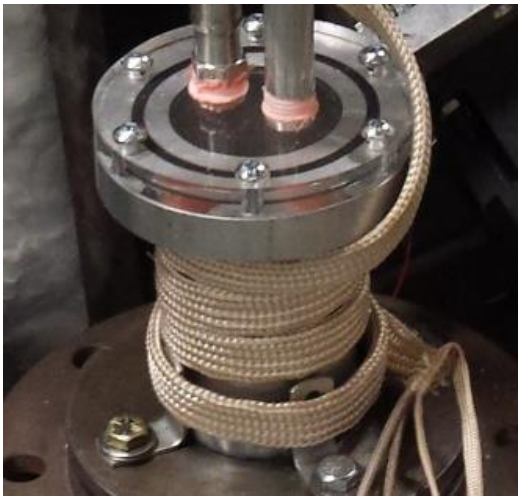

Figure 4.11. The vaporization chamber with the heating tape

4.5.4 Preheated air

Air is supplied from a centralized line at room temperature, which is then injected into the combustion chamber. To preheat the air before flowing into the combustion chamber, and thus avoid cooling the chamber and consequently triggering liquid fuel condensation, a ¼" (6.35 mm) copper tubing of length 25 ft (7.62 m) wrapped with an ultra-high temperature heating tape (the same as the one applied in the vaporization chamber) is connected to the air supply line and covered with insulation fiber to avoid heat transfer to the surrounding environment (Figure 4.12), providing a heating effective area of 239.38 in^2 (0.1544 m^2). The variable power supply controls the temperature at the heating tape.

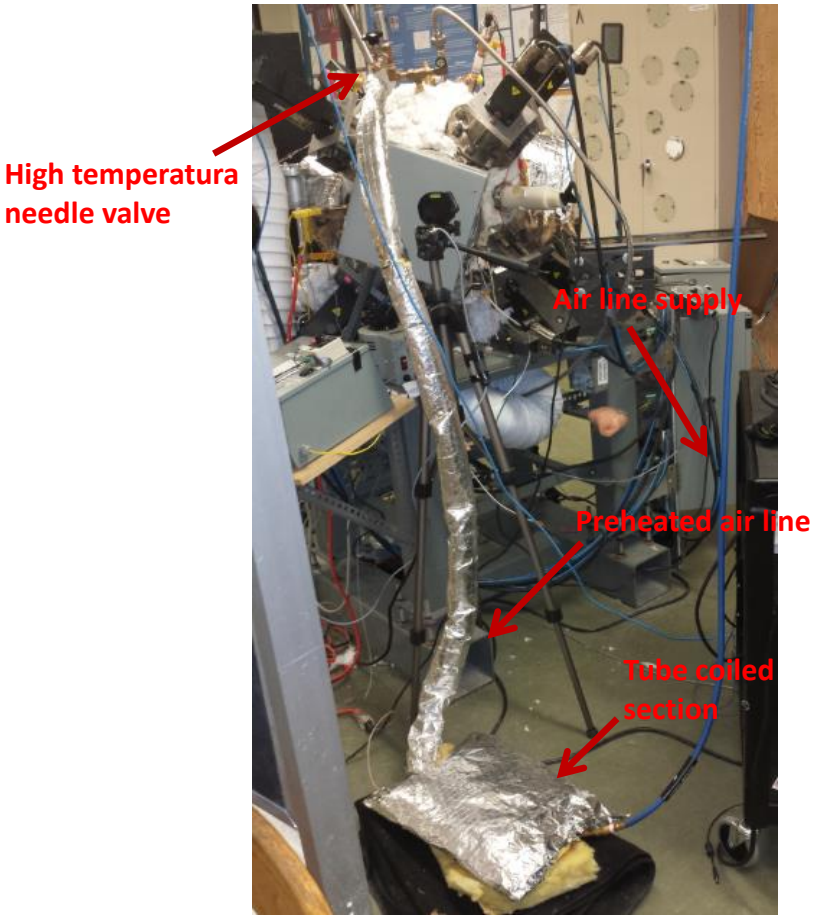

Figure 4.12. Preheated air line

4.6 Ignition system

The fuel/air mixture is ignited in the center point of the combustion chamber by two tungsten rod electrodes of 2 mm diameter and about 400 mm length with a spark gap of 1 mm, as shown in Figure 4.14. The electrodes are fixed to the combustion chamber by an electrode holder attached at each of the two lateral ports of the vessel (see Fig 4.15). To avoid any accidental electrical discharge on the wall of the vessel, the tungsten electrode was fully insulated at the flange to avoid any contact point between them. A complete schematic diagram of the ignition system is shown in Fig 4.13.

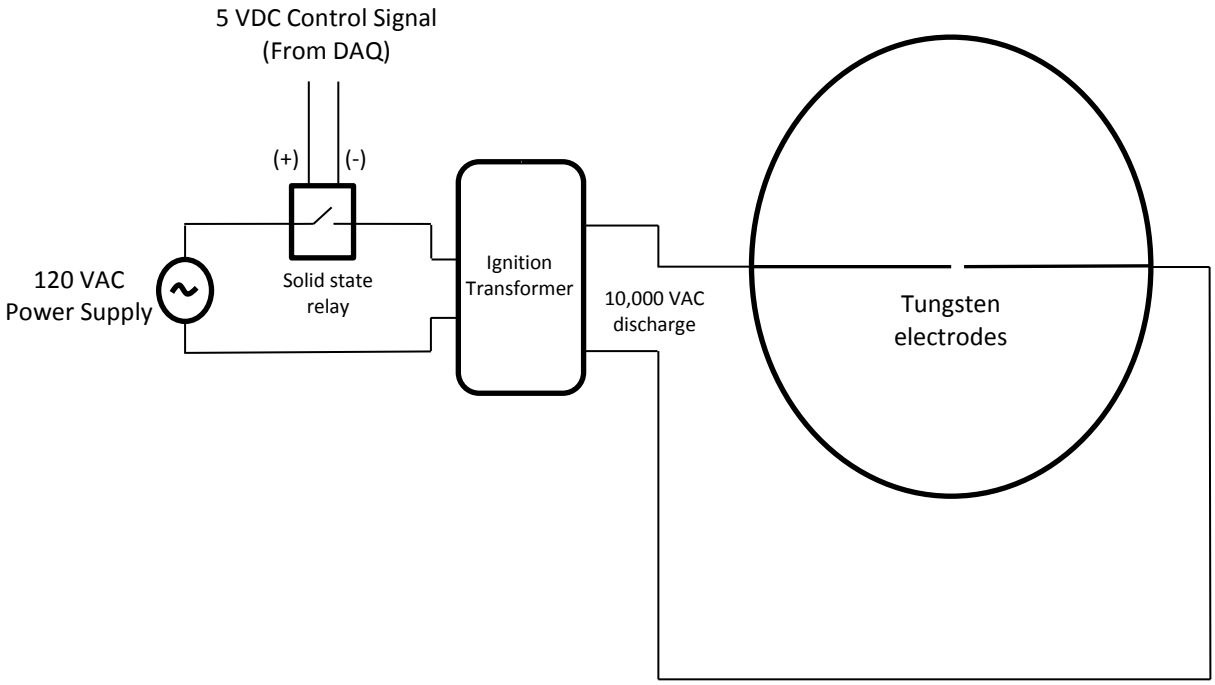

Figure 4.13. Schematic of the ignition system

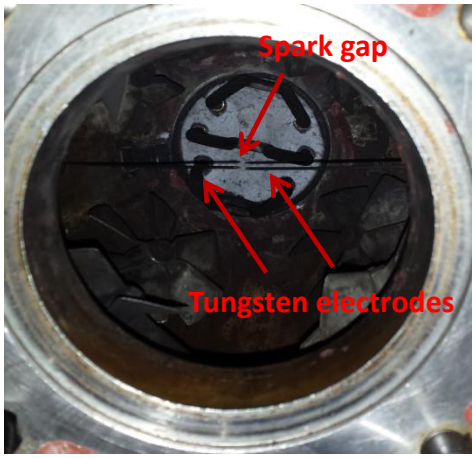

Figure 4.14. Spark gap between the two electrodes

Figure 4.15. Electrode holder

In order to supply a high voltage electrical discharge, an ignition transformer (model Franceformer 5 LAY 12) of 120 VAC power supply generates a 10000 VAC between the two electrodes in order to ignite the fuel/air combustible mixture. The electrical discharge is pulsed from the computer by activating a solid state relay (model RS3-1D10-51) of 120-240 VAC load power and 3-32 VCD control voltage (see Fig. 4.16) controlled from the data acquisition system connected to the computer, as shown in Fig 4.13.

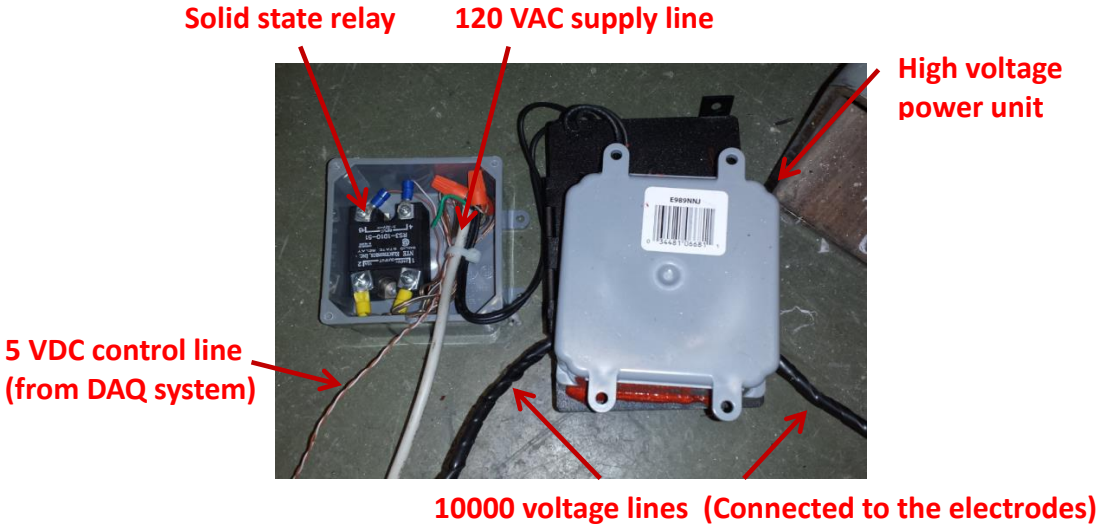

Figure 4.16. Ignition system power supply

4.7 Flame visualization and processing

An imaging technique is developed during the course of this thesis to capture the outwardly propagating flame which originates upon the ignition of the combustible mixture in the center of the combustion chamber. The recorded instantaneous spherical flames over the entire viewing window area are then recorded and post processed where the velocity of propagation of the flame deflagration is then calculated. The Schlieren imaging technique and its associated post processing techniques applied in the present investigation is described below.

4.7.1 Schlieren system

The Schlieren system is an image technique that enable visualization of phenomena in transparent media by ray light bending (refraction) generated by density changes of the visualized environment. For the present investigation, these density changes are caused by the temperature gradient at the flame front of the outwardly-propagating spherical flame, and consequently the flame edge can be visualized and tracked in a sequence of images recorded by a high speed camera [80]. The present methodology involves the generation of a concentrated light beam which falls onto a spherical mirror that reflects the ray through the test sample (in this case the outwardly-propagating spherical flame) to a second spherical mirror located at a distance equal to the focal length of the mirror (60 in). Then, the resulted image is reflected to the high speed camera for recording the test images captured at a given sample rate. For the case of the present experimental setup, a modified version of the Schlieren system suggested in Fig.3.1 was implemented, where the knife edge was removed as a proper focusing of the high speed camera allows the generation of a

clear flame edge (white colored), which does not require the contrast generated by the knife edge, obtaining a shadowgraphic photograph. A schematic of the zig-zag Schlieren technique configuration adopted in this research is given in Figure 4.17.

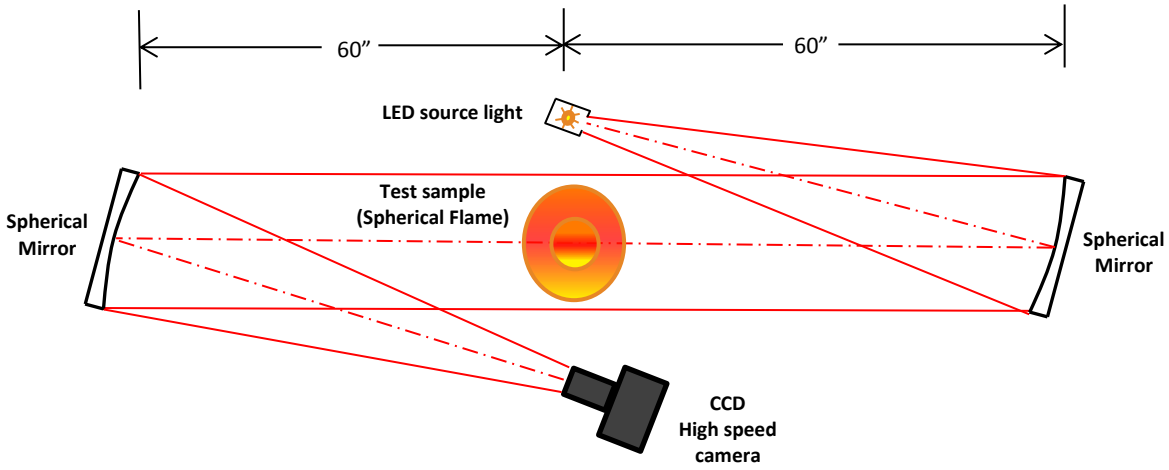

Figure 4.17. Schematic of the Schlieren system

The elements of the configured Schlieren system showed in Figures 4-18 to 4.20 are:

- 2 aluminized spherical mirrors of 6" (152.4 mm) diameter, 60" (1.524 m) focal point and λ/8 high surface accuracy (a measurement of the deviation between the actual and the intended shape of the optical surface).
- A single LED spot light source of 1.8 mW/cm^2: Advanced Illumination model SL4301-WHIIC providing white light with UV compatibility.
- A CMOS high speed camera Nanosense MK II capable of up to 1040 fps at full resolution of 1280 pixels x 1080 pixels.

Figure 4.18. Spherical mirrors

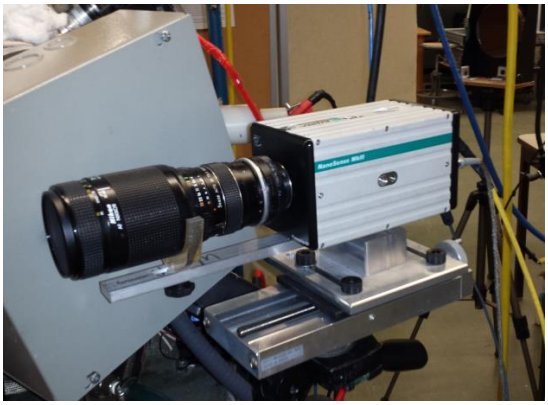

Figure 4.19. High speed camera

Figure 4.20. Light source

4.7.2 Image post processing

The Schlieren photographs in grayscale images captured at 1040 fps (maximum allowable rate at the camera), are recorded and stored in a PC using Motion Studio X64. Each picture consists of a 1280 x 1024 grayscale array of pixel ranging between 1 (black) and 255 (white), as shown in Fig 4.21.

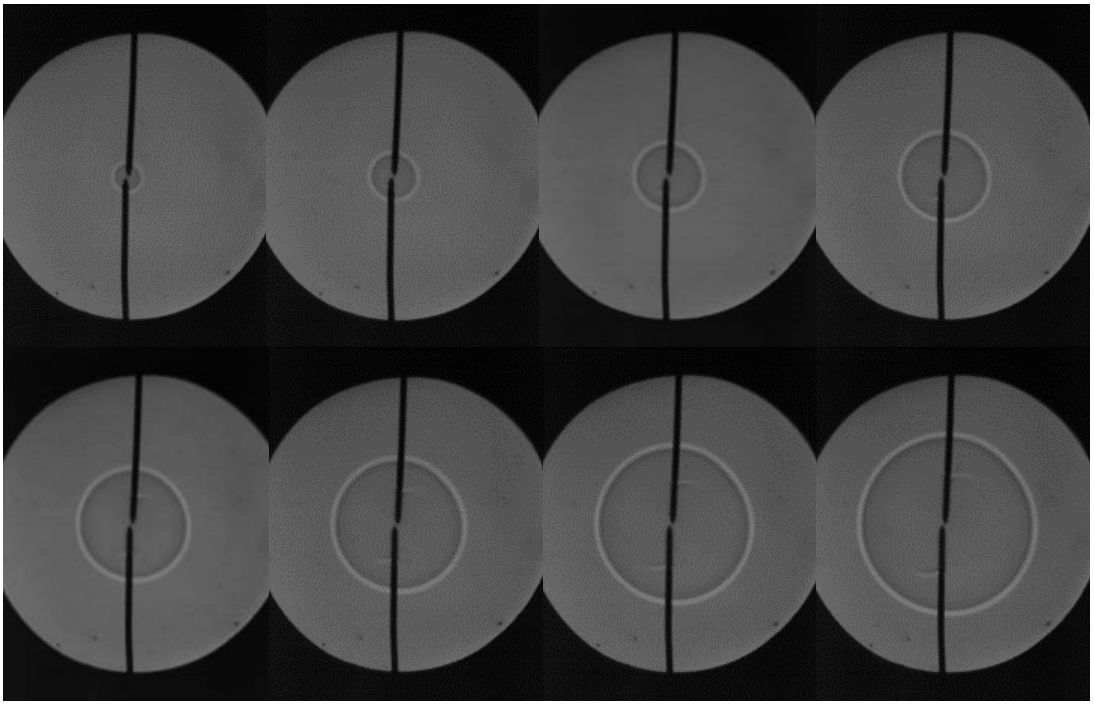

Figure 4.21. Schlieren flame edge photographs

The main objective of the image post-processing is to calculate the radius of the propagating flame at image frame, then, the temporal evolution of the flame can be determined as the camera operates at a fixed sample rate. In order to determine the flame radius, image segmentation, which consists of subdividing an image into its constituent regions, is applied to each photograph/image.

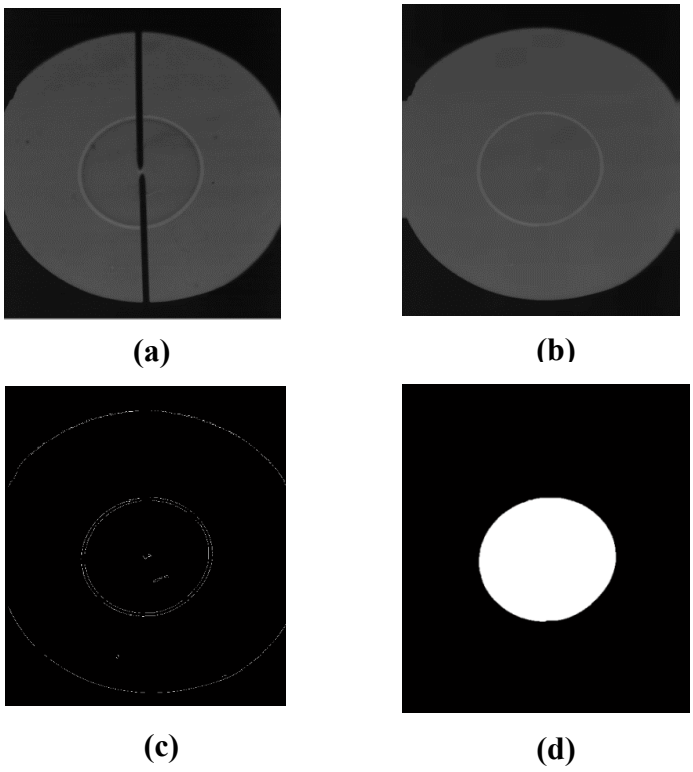

Figure 4.22. Post processing sequence

For the present case, image segmentation was applied following these steps [91]:

- The electrodes are removed from the image by changing their pixel values to grayscale values similar to the ones surrounding these electrodes, as shown in Fig 4.22 (b).
- Edge detection was applied to track the flame front (white edge) by applying Canny edge detector, which smooths the image with a Gaussian filter and then determines the local gradient and its direction at each point. An adjustable threshold sets the limit at which pixel values must be changed to white values (detected edge) and the remaining to black pixels (background, as shown in Fig. 4.22 (c).

- The area enclosed by the detected edge is changed to white pixels (flame region), as shown in Fig. 4.22 (d).
- The flame area is calculated by counting the total amount of white pixels and applying the corresponding scale factor. The scale factor was calculated based on the real electrode diameter (2.3876 mm) and the number of pixels (30) corresponding to this diameter in the Schlieren image, then, the image resolution = electrode pixel width/electrode diameter = 12.57 pixels/mm.

4.8 Instrumentation

Monitoring of the physical phenomena in the combustion chamber and the control of the associated elements of the experimental setup is possible by a configuration of a data acquisition system (DAQ), which enables the input signals coming from different sensors (e.g. thermocouples, pressure transducers, etc.) and the output signals controlling the ignition system and the high speed camera. In the present section, the different elements of instrumentation and their interaction with the data acquisition system are described.

4.8.1 Data acquisition system

The central element of the data acquisition system implemented for the present investigation is a modular hardware that enables the implementation of analog or digital modules in separate slots. The device implemented is a National Instruments compact USB data acquisition system (DAQ) model NI-cDAQ -9172 with a capacity for 8 module slots and linked to a computer by a USB port. The different modules attached to the data acquisition system are described as follows:

- A NI 9263 analog voltage output module provided with 4 channels operating at 16 bits in a range of voltage ± 10V (see Fig 4.23). This module provides 10 VDC signals to control the 8 axial fans servomotors.
- A second NI 9263 analog voltage output module provided with 4 channels operating at 16 bits in a range of voltage ± 10V to generate a 5 VDC pulsed signal that externally activates the high speed camera at a given sample rate (see Fig. 4.23).
- A NI 9205 analog voltage input module provided with 32 single-ended or 16 differential channels operating at 16 bits in a range of voltage ±200mV to ±10V. This module is used to receive the analog signal coming from the two pressure transducers described in section 4.3.1, which measure fuel partial pressure and total mixture pressure (see Fig. 4.23).
- A NI 9211 thermocouple analog input module provided with 4 input channels operating at 24 bits in a range of ± 80 mV, allowing multiple type of thermocouples (e.g. J, K, T, E, N, B, R, S type). The present module receives the signals of three K-type thermocouples placed at the top, north and south sides of the combustion vessel (see Fig. 4.23)
- A NI 9474 digital output module provided with 8 channels with a 5-30 VDC power source for a maximum current of 1A. This module provides a 10 VDC signal to the solid state relay that enables the activation of the ignition system (see Fig. 4.23).

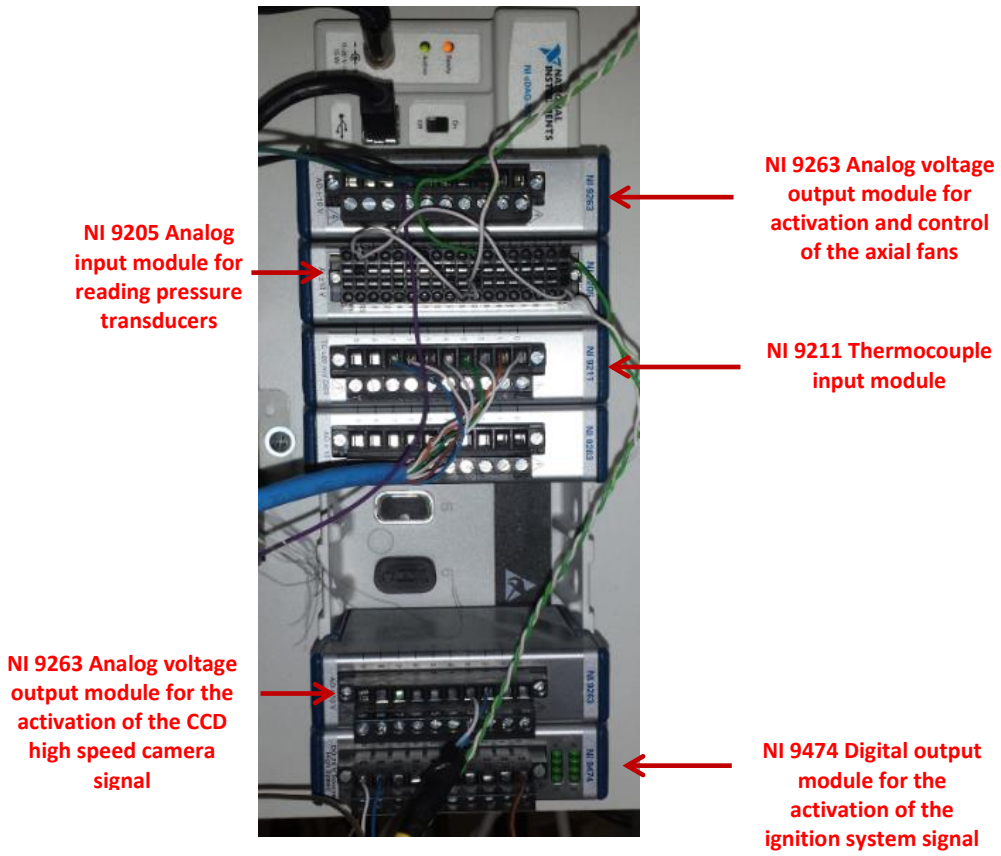

Figure 4.23. Data acquisition system

4.8.2 Voltage amplifier

Due to incompatibility between the operating voltage between the NI 9205 analog voltage input module (±200mV to ±10V) and the high accurate pressure transducer Kulite XTEL-190 (0-250 mV), a signal conditioner module (Fig. 4.24) was added to the test rig to amplify the output voltage supplied by the pressure transducer monitoring the fuel partial pressure. In order to provide the suitable voltage, a DC to DC isolated signal conditioner Omega DMD4380 was added to the data acquisition system, whose characteristics are:

- Power supply: 10-32 VAC
- Input ranges: Selectable inputs of 0-5 mVDC to 0-400 mVDC. For the present experimental setup, the signal conditioner was fixed at 0-250 mVDC.
- Output ranges: Selectable outputs of 0-1 VDC to 0-10VCD. For the present configuration, the signal conditioner was fixed at 0-10 VDC.

Figure 4.24. Voltage amplifier

4.8.3 Thermocouples

Three K-type thermocouples were placed at different locations (north and the south sides) to ensure homogeneous temperature inside the combustion chamber. A schematic of the location of each thermocouple is shown in Fig. 4.25, which corresponds to the top view of the combustion chamber.

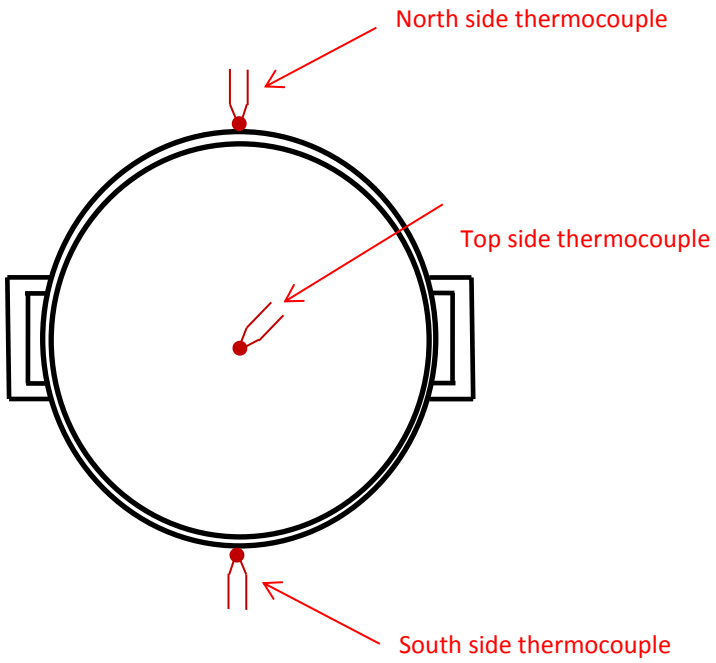

Figure 4.25. Locations of the thermocouples

4.8.4 User interface

A Labview user interface enables the reading of all sensors connected to the combustion chamber and controls the entire systems (e.g. axial fans, ignition system, and high speed camera), as shown in Figure 4.26. On the left side, an adjustable selector enables to set the speed of the axial fans (in RPM) with gradual increment of 20 rpm from the current to the target velocity. Additionally, three temperature displays show the current temperature at each thermocouple location, and the two lower displays the actual pressure measurements corresponding to the partial and total pressures inside the vessel. Finally, a camera frequency selector allows setting the sample rate at which the Schlieren photographs are taken and a waveform plot shows the camera signal once is generated at the ignition press button.

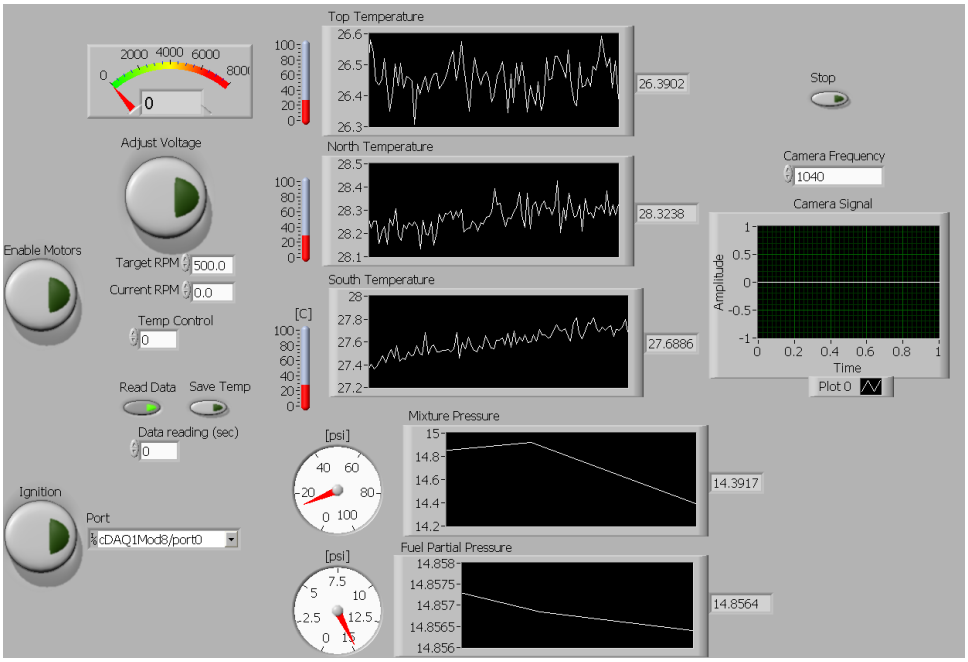

Figure 4.26. User interface

Chapter 5 – Results and discussion

5.1 Introduction

Results for laminar flame speed of a renewable liquid biofuel are presented in this section. Validation of the experimental setup and configuration was achieved by measuring the laminar flame speed of methane/air mixtures for the case of gaseous fuels and n-heptane/air mixtures for liquid fuels. Experimental results on the novel liquid biofuel; 1,3 dimethoxyoctane (referred to thereafter as 1,3-DMO) were obtained for different equivalence ratios tested at atmospheric pressure and 423 K.

5.2 Validation of the experimental setup and methodology

In order to validate the experimental test rig and methodology, laminar flame speed measurements of methane/air and n-heptane/air mixtures were performed at atmospheric pressure and different ambient temperatures.

5.2.1 Methane/air mixtures

Laminar flame speed measurements of methane/air mixtures tested at 298 K and 1 bar were obtained at different equivalence ratios ranging between 0.8 and 1.3. The partial pressure methodology was applied to determine the amount of fuel to inject in the combustion chamber as described in section 4.3.1 of chapter 4. The test conditions are summarized in Table 5.1. The obtained results were compared with published experimental data [96, 97, 98, 99, 100, 101], and showed good agreement between the present results and published data as shown in Figure 5.1. However, although the present experimental results nearly overlap those of Law et al. [98], they still show some differences in magnitude with

other published results, as seen in Fig. 5.1. The main reason of this discrepancy can be attributed to the difference in the way density ratio was determined (as shown in Figure 5.2), as it is required to determine the laminar flame speed of the fuel/air mixture. Lower density ratios lead to obtain relatively low laminar flame speed, especially at stoichiometric and fuel rich conditions, as shown by the databases reported by Gu et al. [96] and Bradley et al. [97]. Another reason for the differences between different databases might be attributed to the methodology adopted. For instance, the numerical results reported by Bradley et al. [97] under predict most experimental data including those presented by Law et al. [98]. The latter applied the counterflow flame methodology and obtained results which have a difference ranging between 5% and 20% compared to published data [96, 97, 99, 100], as shown in Table 5.2.

ϕ	**Fuel partial pressure [psi]**	**Mixture pressure [psi]**	**T [K]**
0.7	0.986	14.92	298
0.8	1.124	14.92	298
1	1.378	14.92	298
1.1	1.502	14.92	298
1.2	1.610	14.92	298
1.3	1.742	14.92	298

Table 5.1. Test conditions for methane/air mixtures

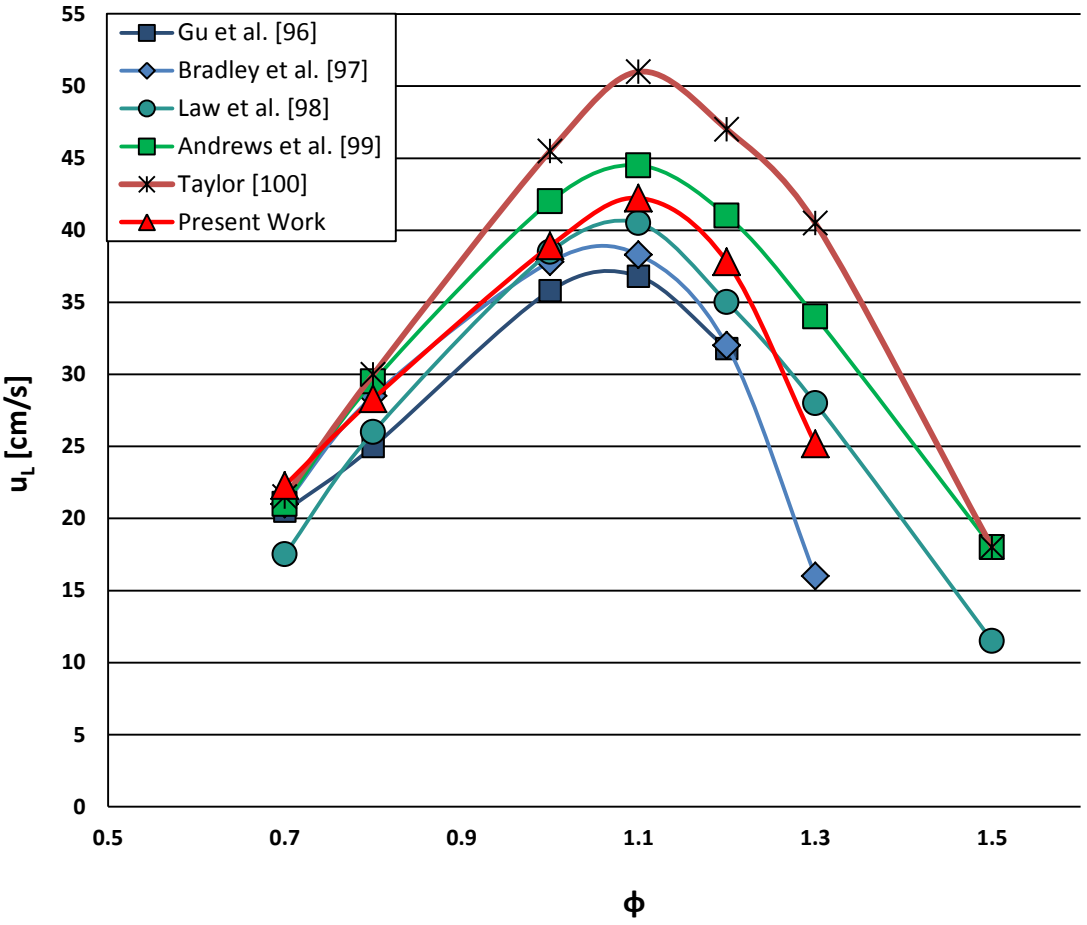

Figure 5.1. Laminar flame speed of methane/air mixtures

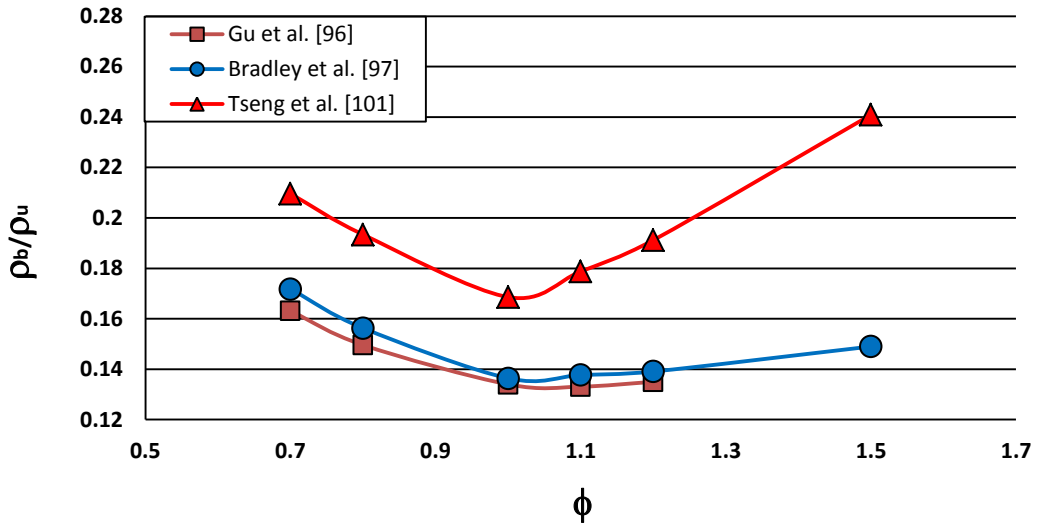

Figure 5.2. Density ratio for methane/air mixtures at 1 bar and 300 K

Fig 5.2 shows the density ratio of methane/air mixtures over an extended range of equivalence ratio. This ratio was used for determining laminar flame velocity (u_l) depicted in Fig. 5.1. It shows that, while the trend is similar between all these studies, the density ratio of Gu et al. [96] and Bradley et al. [97] is noticeably smaller than that of Tseng et al. [101] by as much as 15% to 25%. This could be attributed to fact that Gu et al. [96] and Bradley et al. [97] used a comprehensive numerical simulations which included all conservation equations (e.g. mass, momentum, energy, species), however Tseng et al. [101] relied simply on thermodynamic combustion properties (e.g. adiabatic flame temperature, partial pressure).

T [K]	P [bar]	ϕ	Type of study	Type of flame	Ref.
300-400	1	0.7-1.2	Experimental	Spherical Flame	[96]
300	1	0.7-1.3	Numerical	Spherical Flame	[97]
298	1	0.7-1.5	Experimental	Counterflow planar	[98]
298	1	0.7-1.5	Experimental	Spherical Flame	[99]
298	1	0.7-1.5	Experimental	Spherical Flame	[100]

Table 5.2. Published test conditions for determining laminar flame speed of methane/air mixtures

5.2.2 Heptane/air mixtures

Validation of the experimental setup and methodology for laminar flame speed of liquid fuels was achieved by measuring laminar flame speed of heptane/air mixtures for equivalence ratio ranging between 0.8 and 1.5 at 353 K and atmospheric pressure. These data along with published results are presented in Fig. 5.3. The test conditions are presented in Table 5.4. The present experiments were performed by adopting the volumetric fuel injection methodology described in section 4.3.2. Heptane/air mixture laminar flame speed was calculated using the density ratio of decane/air mixtures of planar flames reported by Singh [75], who developed a numerical simulation based on CHEMKIN package [59] assuming steady flow and calculated laminar burning speed of decane/air mixtures at atmospheric pressure and an initial temperature of 400 K. According to the numerical simulation of Gu et al. [96], a difference in the initial temperature of about 50 K can result in a difference in the density ratio ranging between 7% and 10 % [75].

Thermocouple Reading			**Average**
T_1[K]	T_2 [K]	T_3 [K]	T [K]
80.851	79.036	80.455	80.114

Table 5.3. Temperature reading in the combustion chamber

Comparing the present results to published experimental data **[**61, 102, 103, 104**]** showed reasonable agreement between them. The slight differences may be attributed to difference in the initial temperature. It is evident that laminar flame speed is highly sensitive to temperature variance, especially for liquid fuels, as flame speed tends to increase with

temperature (it is required to maintain the ambient temperature above the fuel boiling point to ensure complete vaporization). For the case of the present experimental results, it was important to record temperature in different regions of the spherical combustion chamber. Temperature readings at three different locations in the combustion chamber were taken and an initial temperature was taken as the average of these temperature readings. Two thermocouples are placed opposite to one another along the horizontally centerline plan, and the third from the top of the chamber along the vertical centerline. The thermocouples are positioned at a distance inside the chamber of about 40 mm. Typical temperatures are given in Table 5.3. Thus, this might be partly responsible for the differences of the present data with their counterpart published experimental results. The testing conditions of different literature sources are shown in Table 5.5.

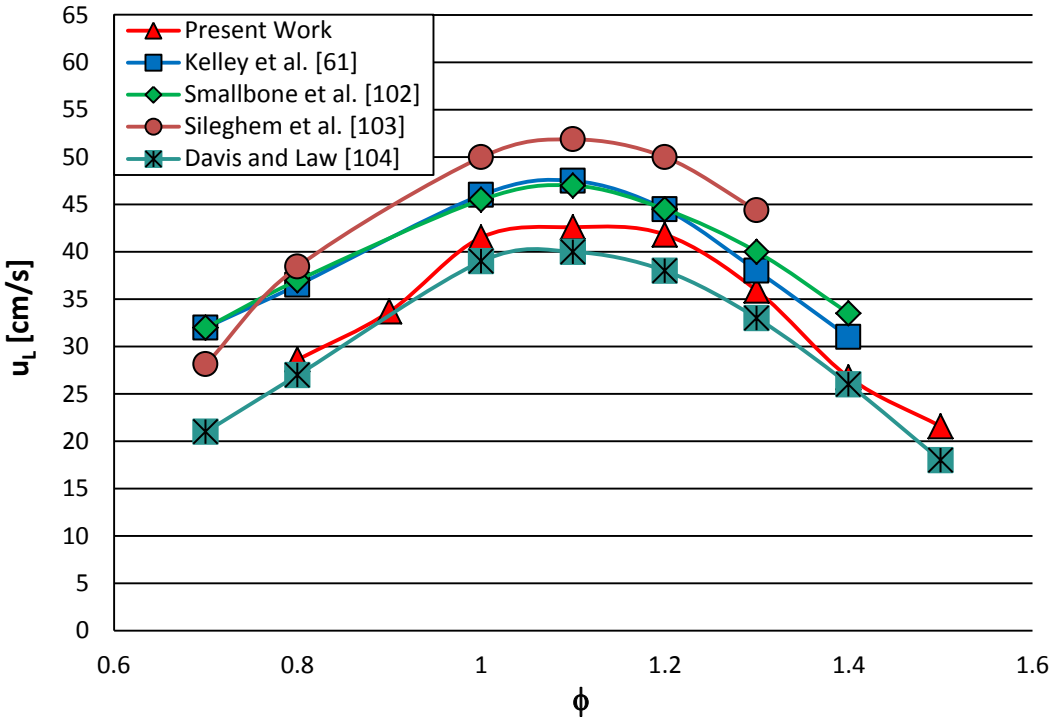

Figure 5.3. Laminar flame speed of n-heptane/air mixtures

ϕ	Fuel volume [ml]	Mixture pressure [psi]	T [K]
0.8	2.237	14.92	353
0.9	2.510	14.92	353
1	2.790	14.92	353
1.1	3.076	14.92	353
1.2	3.350	14.92	353
1.3	3.630	14.92	353
1.4	3.9158	14.92	353
1.5	4.195	14.92	353

Table 5.4. Test conditions for heptane/air mixtures

T [K]	P [bar]	ϕ	Type of study	Type of flame	Ref.
353	1	0.7-1.4	Experimental	Spherical Flame	[61]

350	1	0.7-1.4	Experimental	Counterflow planar	[102]
358	1	0.7-1.3	Experimental	Heat flux planar	[103]
298	1	0.7-1.5	Experimental	Counterflow planar	[104]

Table 5.5. Published laminar flame speed of n-heptane/air mixtures

5.3 Laminar flame speed of 1,3-DMO

Measurements of laminar flame speed of the novel liquid biofuel (i.e., 1,3 dimethoxyoctane; referred to as 1,3-DMO) were obtained at 423 K and atmospheric pressure for different equivalence ratios ranging between 0.7 and 1.6. The experiments were conducted using the volumetric injection methodology of fuel as summarized in Table 5.6 and described in section 4.3.2. The temporal evolution of the flame radius obtained using Schlieren images is shown in Figure 5.4, where the data for six different equivalence ratios are plotted. The radius evolution confirms the linear growing of the spherical flame at a radius greater than 6 mm for stoichiometric and fuel rich conditions. However, this novel fuel shows a particular behavior at lean condition where the flame propagation shows a greater initial increase caused by the ignition, followed by a slowdown and finally the typical linear trend though the remaining time. The slowdown duration becomes more evident as fuel conditions become leaner.

ϕ	**Fuel volume [ml]**	**Mixture pressure [psi]**	**T [K]**
0.8	1.774	14.92	423

0.9	2.027	14.92	423
1	2.534	14.92	423
1.1	2.788	14.92	423
1.2	3.041	14.92	423
1.3	3.290	14.92	423
1.4	3.54	14.92	423
1.5	3.802	14.92	423
1.6	4.050	14.92	423

Table 5.6. Test conditions for 1, 3-DMO/air mixtures

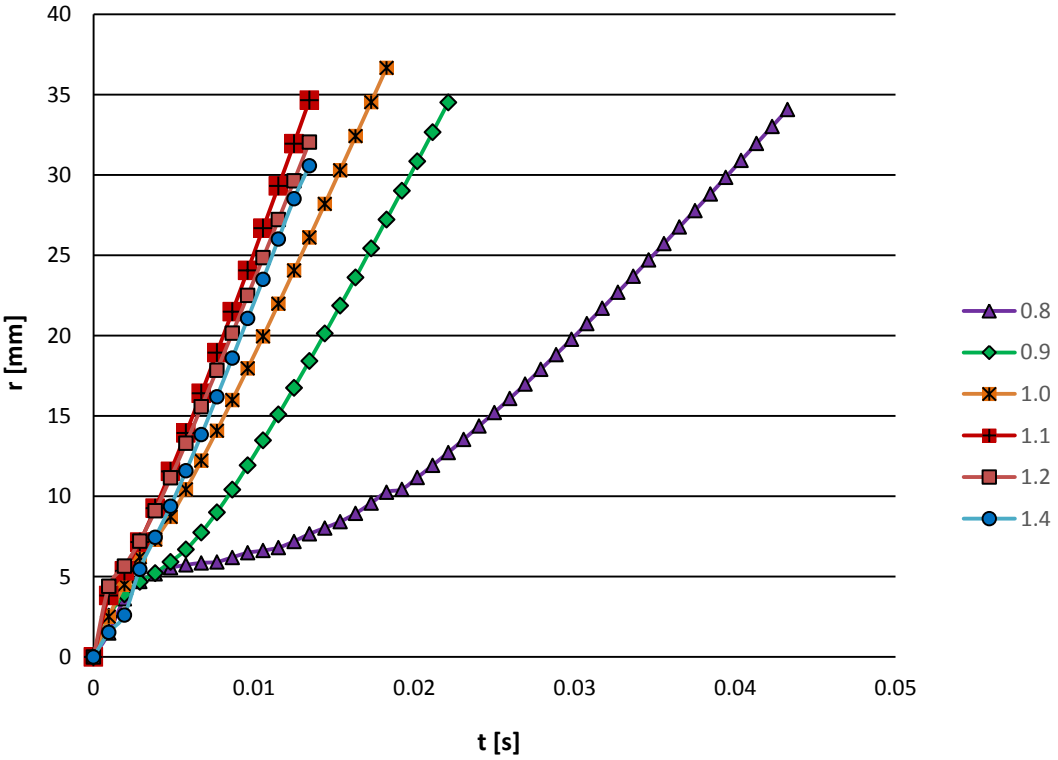

Figure 5.4. Flame radius temporal evolution of 1,3-DMO/air mixtures

The stretched laminar flame speed versus the stretch rate (calculated using Eq. 3.2 above) is presented in Fig. 5.5 for different equivalence ratios. Each plot in this figure accounts for the effect of strain and curvature of the spherical flame. A reference flame speed (at non-stretch conditions), representing the ideal case of planar zero-stretched flame,

is obtained by applying a linear extrapolation. The main observations about the present plots are summarized as follows: The characteristic of decreasing trend of laminar flame speed as stretch ratio increases is noticeably observable, in addition to the reduction of the stretch rate range at lower equivalence ratios in agreement with published results of hydrocarbon fuels (gaseous and liquids) and also other alternatives (e.g. methane, isooctane, dimethyl ether, methylfuran) [28, 32, 65, 96]. Furthermore, the novel fuel shows high reactivity at stoichiometric and fuel rich conditions, in contrast to a weak flame propagation at fuel lean condition.

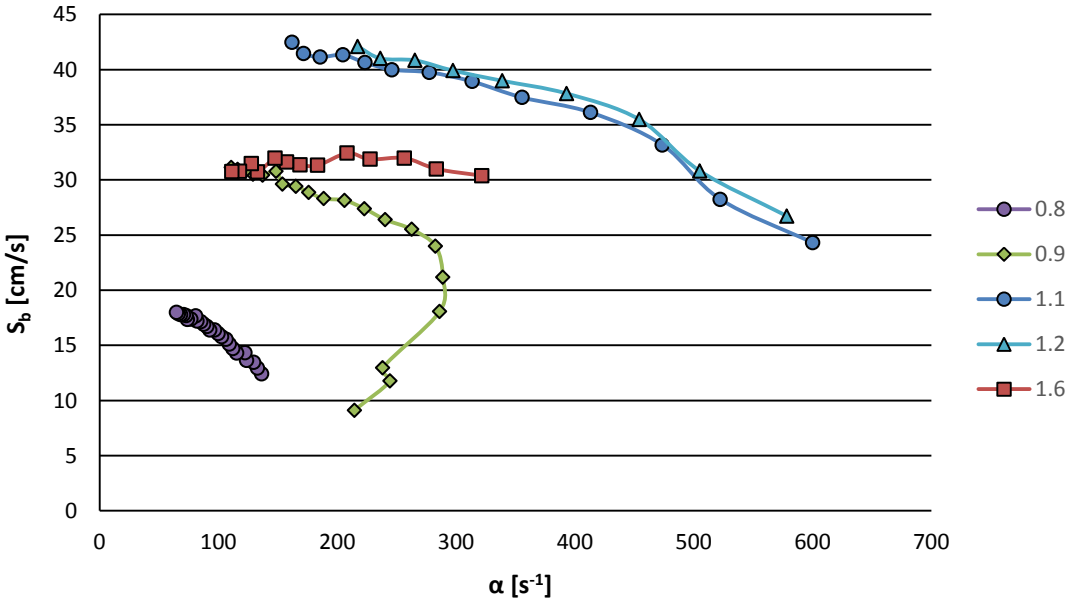

Figure 5.5. Laminar flame speed vs. stretch rate of 1,3-DMO/air mixtures

Fig 5.6 shows the Markstein length (L_b) versus the equivalence ratio plot of 1, 3 DMO, gasoline and h-heptane/air mixtures. It is obtained by determining the slope of the laminar flame speed versus stretch rate graph (calculated using Eq. 3.1 above), which represents the effect of curvature on localized burning velocity [28], according to what is shown in Eq. 3.1. The importance of the Markstein length in the analysis of flames resides

in its indication of the stability of the propagating deflagrations for a given fuel/air mixture; where higher Markstein lengths means more stable flames due to a higher response of laminar flame speed to flame stretch [30, 101]. The present results indicate a monotonic decreasing in Markstein length as the equivalence ratios increases for all given fuels, even though 1,3-DMO shows higher Markstein lengths at fuel rich conditions as compared to other fuels, which is an evidence of higher stability than n-heptane and gasoline; but lower at fuel lean and stoichiometric conditions. In general, both 1,3-DMO and n-heptane presents similar Markstein lengths over almost the equivalence ratio range (0.8-1.3), suggesting a similar hydrodynamic behavior, however n-heptane experiences a drastic stability drop at equivalence ratios above 1.3. It is importance to remark that the referenced fuels were tested at different temperatures (373 K for gasoline and 358 K for n-heptane) compared to the one of the present investigation (i.e., 423 K for 1,3-DMO), leading to under prediction of the Markstein lengths of the novel biofuel at similar conditions to these fuels, as the database reported by Tian et al. [30] suggests that Markstein length decreases as temperature raises. Thus, this suggests a higher Markstein length of the present data if the temperature conditions were similar to those referenced fuels (i. e., 358 K to 373 K).

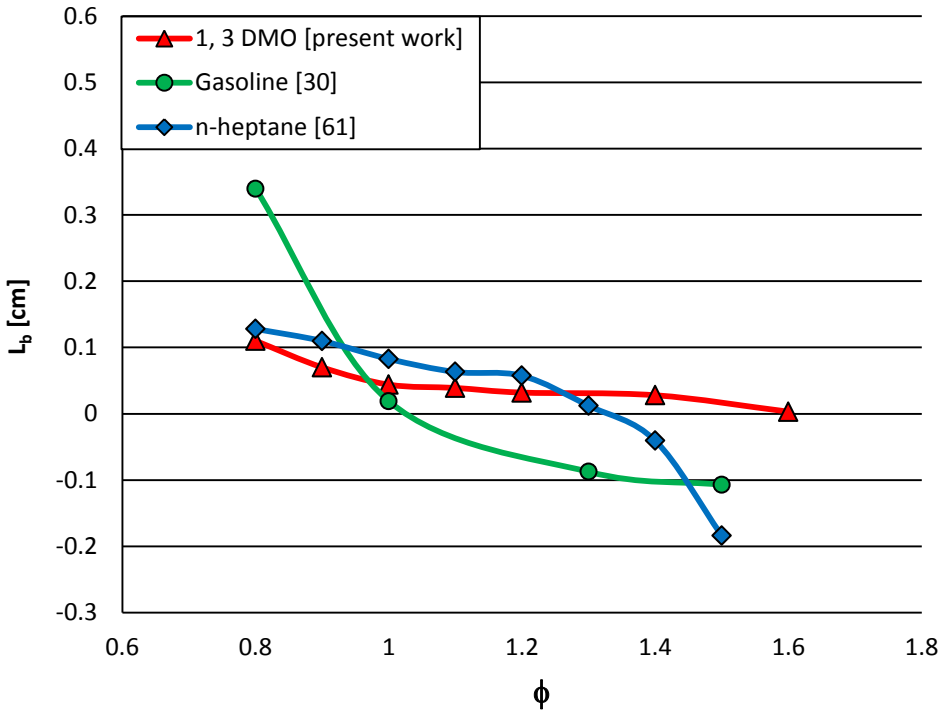

Figure 5.6. Markstein length vs. equivalence ratio

The laminar flame speed at different equivalence ratios ranging between 0.7 and 1.6 is presented in Fig 5.7, where the novel fuel 1,3-DMO is compared with the results of other methyl-alkyl biodiesel surrogates (e.g. butanoate, crotonate, decanoate). Similarly to section 5.2.2, laminar flame speed of 1,3-DMO was calculated using the density ratio of methylcyclohexane (MCH)/air mixtures simulated at 1 bar and an initial temperature of 400 K. This is because of the reactivity (referred to here as flame speed) of methylcyclohexane (MCH) was found to be similar to most biodiesel surrogates, as shown in Fig 2.1. Singh [75] reported numerically that the difference in the density ratio between decane/air mixture (reference for n-heptane) and methylcyclohexane/air mixture (reference for 1,3-DMO) is within 2%. Three main observations can be drawn from Fig 5.7. Firstly, the novel fuel, 1,3-

DMO, shows slightly lower but comparable reactivity (laminar flame speed) compared to that of biodiesel surrogates. However, this difference is substantial compared to diesel and palm methyl biodiesel due to the difference in the initial temperatures used in each study. Secondly, the fuel rich conditions of the novel fuel are an evidence of a strong reactivity at equivalence ratios up to 1.6 as compared to other fuels, which can be explained by the saturated fatty acid structures present in the novel fuel that promote higher flame temperatures and consequently increased flame speed [4, 5, 6]. Thirdly, the fuel lean condition shows a weak propagation, confirming the observations in Fig 5.4, where flame propagation shows low velocities and a deflagration slowdown at radius between 5 to 10 mm. The low reactivity at fuel lean conditions could be attributed to the fact that saturated fatty acids present in 1,3-DMO tend to inhibit fuel oxidation [6]. The uncertainty analysis presented in Appendix B estimates an error ranging between 4.85 and 9.3% in the measurements, as shown in Table 5.7.

ϕ	**U_{SL} [cm/s]**	**%**
0.7	1.22965	5.5166
0.8	1.50817	5.3273
1	1.93623	4.9762
1.1	2.05181	4.8587
1.2	1.98968	5.2623
1.3	2.34131	9.302

Table 5.7. Uncertainty of laminar flame speed measurements

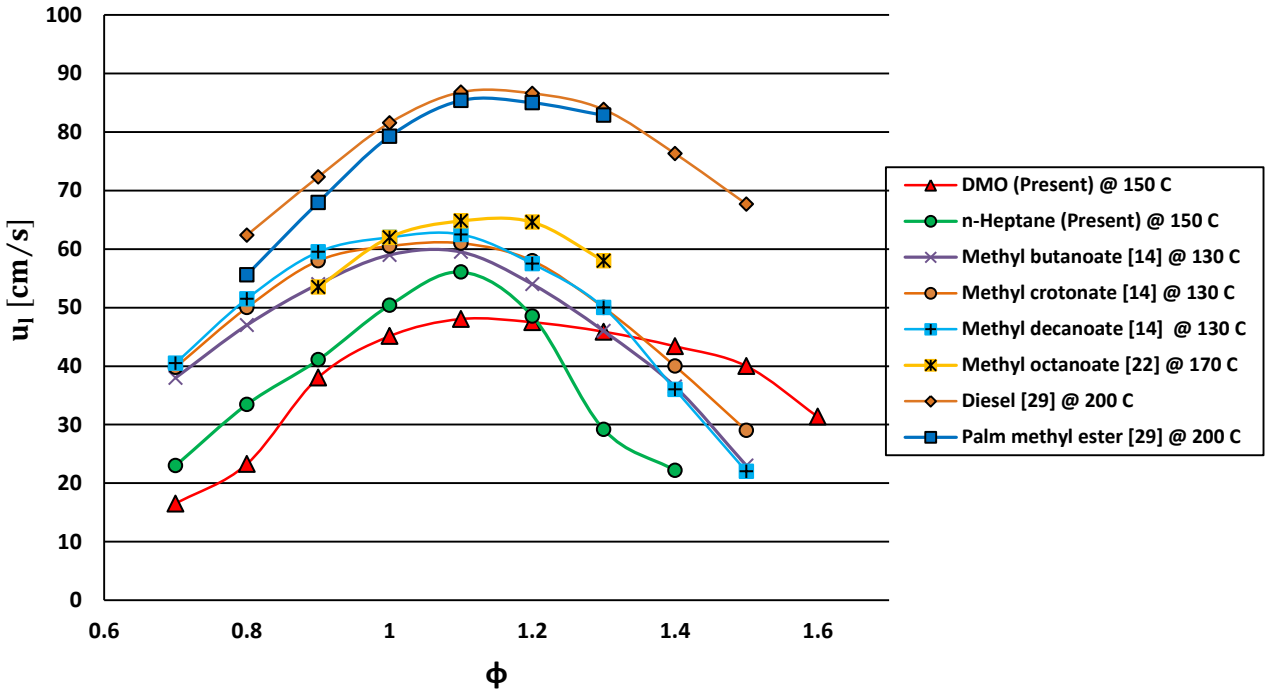

Figure 5.7. Laminar flame speed vs. equivalence ratio of 1, 3-DMO/air mixtures

5.4 Flammability limits of 1,3-DMO fuel

In order to further investigate the newly developed liquid biofuel (1,3-DMO), its lower and upper flammability limits (LFL and UFL) were explored by applying the visual

criterion of ASTM E-681 described in section 2.4 of chapter 2. Determination of each flammability limit was performed by averaging the fuel volume for a successful flame and that of its consecutive non-successful flame at both the lower and upper limits, as shown in Table 5.8.

		Non - successful flame	Successful flame	Average
Fuel Lean Condition	**[% vol]**	0.7197	1.0078	0.863
	ϕ	0.6	0.7	0.65
Fuel Rich Condition	**[% vol]**	14.24	13.42	13.836
	ϕ	1.8	1.7	1.75

Table 5.8. Measured fuel samples/quantities for determining flammability limits of 1,3-DMO

The experimental results for the flammability limits of the present fuel are presented in Table 5.9, where these results are given in % volume of fuel in the fuel/air mixture and its corresponding equivalence ratio.

LFL		**UFL**	
[% vol]	**ϕ**	**[% vol]**	**ϕ**
0.863	0.65	13.836	1.75

Table 5.9. Flammability limits of 1,3-DMO

Figure 5.8 presents a comparative chart of the flammability limits between the present fuel and other/published fuels [50, 51]. Results presented in this figure/chart shows flammability limits of 1,3-DMO fuel similar to those of light alkane fuels (e.g., methane,

ethane), but considerably higher than those of common liquid alkanes (e.g., n-heptane, isooctane, decane) and multicomponent combustibles (e.g. diesel, gasoline, kerosene).

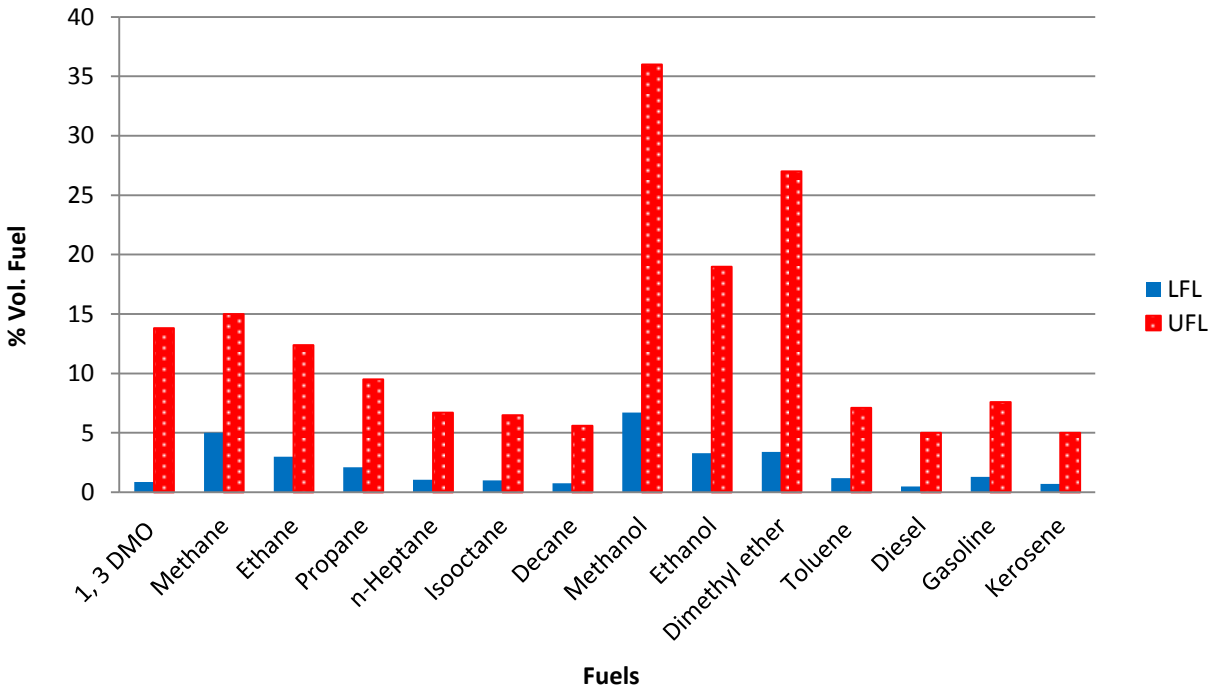

Figure 5.8. Flammability limits of fuels

Chapter 6 – Conclusions and Recommendations

6.1 Conclusions

An experimental method was developed in the present thesis to measure laminar flame speed of fuel/air mixtures at different equivalence ratios. The optical technique implemented in this study for imaging flame propagation was the Schlieren technique. A Matlab code was developed for processing flame propagation images of spherical flames. Validation of the experimental setup and methodology was done for gaseous fuel by measuring the laminar flame speed of methane/air mixtures and for liquid fuels by testing heptane/air mixtures and comparing with published databases.

Laminar flame speed of the novel liquid biofuel (i.e., 1, 3 dimethoxyoctane (1,3-DMO)) has shown to be a feasible surrogate of biodiesel fuels owing to its comparable reactivity to gaseous and liquid hydrocarbon fuels at any equivalence ratio. The present findings concerning the laminar flame speed of this liquid biofuel follows the common parabolic behaviour of laminar flame speed as a function of equivalence ratio. However, its laminar flame speed tends to be relatively higher at fuel rich conditions in contrast to its weak reactivity at fuel lean conditions. The analysis of the Markstein length of the 1,3-DMO fuel revealed relatively low stability in flame propagation at fuel lean and stoichiometric conditions but high stability at fuel rich conditions when compared to heavy hydrocarbon fuels. Additionally, its flammability range is wider than most common liquid hydrocarbon fuels (e.g, n-heptane, isooctane, decane) and closer to gaseous hydrocarbon counterparts (e.g. methane, ethane).

This suggests that this novel biofuel might be used in internal combustion engines (e.g., compression ignition, homogeneous charge compression engines) owing to its

competitive reactivity as compared to common hydrocarbon surrogates (e.g. isooctane, n-heptane). However, the possibility to implement this fuel as a stand-alone fuel should be subjected to further investigations in order to determine other combustion characteristics

6.2 Recommendations for future work

During the development of the present investigation, different opportunities for further research and some recommendations for improving the experimental setup and methodology have emerged, especially to obtain flame speed measurements of different fuel/air mixtures over a much wider test conditions. These recommendations can be summarized in this section.

Recommendations for further research

- Investigation of turbulent flame speed of different fuel/air mixtures can be developed by the current experimental configuration. This is especially to benefit from the existence of 8 axial fans which enable the generation of isotropic and homogeneous conditions at the central region of the spherical test vessel. These are ideals test conditions for determining turbulent flame speed.
- Further research on laminar flame speed of gaseous fuels such as biogas mixtures and their blends (e.g., hydrogen addition), and also other pure and blended liquid fuels (e.g., 1,3-DMO and its blend with biodiesel or diesel). In order to perform this study, the current heating system of the test rig must be improved to achieve higher initial temperatures of the content of the combustion chamber.
- In the case of the liquid fuels already tested, the phenomenon of condensation should be explored beyond the extents of the present work as the reported

predictions of condensation temperatures are based on available experimental databases of surrogates having similar chemical structure to the new biofuel tested in the present thesis.

- Investigating the effects of pressure and temperature variation on the laminar flame speed of fuel/air mixtures of 1,3 dimethoxyoctane to ensure a comprehensive characterization of this fuel at engine relevant conditions

Recommendations for improvements of the experimental setup

- In order to obtain more reliable data from the imaging technique, a high speed camera having higher frame rate is necessary to fulfill the velocity requirements of outwardly-propagating spherical deflagrations occurring within a time range of 50 ms; laminar flame speed measurements of fuel/air mixtures at velocities higher than 60 cm/s (e.g. decane, n-heptane above 443 K) might be inaccurate because only less than 10 images could be analyzed.
- Improving the current post processing code by refining the already implemented techniques (e.g., edge detection, filtering) to reduce the measurement uncertainties caused by image processing (e.g., image noise, poor edge detection). In order to process turbulent flames, the methodology for flame area calculation must be modified as the one developed in the present investigation is based on the circumferential area of spherical laminar flames.
- Integrate (use a single, upgraded/faster PC) the operation of the data acquisition system and the image capturing software in order to obtain faster response from the different input and output devices of the spherical chamber (e.g. thermocouples, pressure transducers, ignition system). Consequently, pressure and temperature

recording can be obtained at higher rates, and a better synchronization between the ignition system and the camera signal can be achieved so that the entire operation of the test rig can be controlled from a single computer.

- Improving the liquid fuel injection system; that is the volumetric injection methodology (described in section 4.3.2) which allows fuel droplet deposition to ensure complete vaporization. For instance, the use of a syringe pump connected to a thinner needle will enable accurate control of fuel deposition/injection rate.
- Provide a better insulation of the combustion chamber to prevent/minimize heat transfer/loss to the surroundings environment.
- Upgrade the two electrode holders of the ignition system to improve its functionality at high pressure (prevent leakage, and prevent the system from releasing any of its components).
- Develop the relief valves system in order to keep constant the combustion pressure so that higher initial test pressures can be examined. In addition, a thinner duct (e.g., 3” flexible or semi-rigid duct) should be installed at the outlet port of the vacuum pump to prevent gas accumulation near the test rig and optimize space.

References

[1] A. Demirbas, Progress and recent trends in biofuels, Progress in Energy and Combustion Science 33 (2007) 1-18.

[2] A. Demirbas, Importance of biodiesel as transportation fuel, Energy Policy 35 (2007) 4661-4670.

[3] U.S Energy Information Administration, International energy outlook, DOE/EIA-0484(2014), http://www.eia.gov/forecasts/ieo/pdf/0484(2014).pdf,

[4] G. Liu, Development of low-temperature properties on biodiesel fuel: a review, International Journal of Energy Research 39(2015) 1295-1310.

[5] J. Park, D. Kim, J. Lee, S. Park, Y. Kim and J. Lee, Blending effects of biodiesel on oxidation stability and low temperature flow properties, Bioresource Technology 99(2008) 1196-1203.

[6] M. Serrano, R. Oliveros, M. Sanchez, A. Moraschini and M. Martinez, Influence of blending vegetable oil methyl esters on biodiesel fuel properties: Oxidative stability and cold flow properties, Energy 65(2014) 109-115.

[7] B.K. Sharma, P.A.Z. Suarez, J.M. Perez and S.Z. Erhan, Oxidation and low temperature properties of biofuels obtained from pyrolysis and alcoholysis of soybean oil and their blends with petroleum diesel, Fuel Processing Technology 90(2009) 1265-1271.

[8] H.S. Zhen, C.W. Leung, C.S. Cheung and Z.H. Huang, Characterization of biogas-hydrogen premixed flames using Bunsen burner, International Journal of Hydrogen Energy 39 (2014) 5083-5097.

[9] S.A. Shahir, H.H. Masjuki, M.A. Kalam, A. Imran, I.M. Rizwanul Fattah and A. Sanjid, Feasibility of diesel-biodiesel-ethanol/bioethanol blend as existing CI engine fuel: An assessment of properties, material compatibility, safety and combustion, Renewable and Sustainable Energy Reviews 32(2014) 379-395.

[10] W.J. Pitz and C.J. Mueller, Recent progress in the development of diesel surrogate fuels, Progress in Energy and Combustion Science 37(2011) 330-350.

[11] M.H. Hakka, P.A. Glaude, O. Herbinet and F. Battin-Leclerc, Experimental study of the oxidation of large surrogates for diesel and biodiesel fuels, Combustion and Flame 156(2009) 2129-2144.

[12] L. Coniglio, H. Bennadji, P.A. Glaude, O. Herbinet and F. Billaud, Combustion chemical kinetics of biodiesel and related compounds (methyl and ethyl esters): Experiments and modelling-Advances and future refinements, Progress in Energy and Combustion Science 39(2013) 340-382.

[13] T.A. Semelsberger, R.L. Borup and H.L. Greene, Dimethyl ether (DME) as an alternative fuel, Journal of Power Sources 156(2006) 497-511.

[14] Y.L. Wang, Q. Feng, F.N. Egolfopoulos and T.T. Tsotsis, Studies of C_4 and C_{10} methyl ester flames, Combustion and Flame 158(2011) 1507-1519

[15] W. Liu, A.P. Kelley and C.K. Law, Non-premixed ignition, laminar flame propagation and mechanism reduction of n-butanol, iso-butanol and methyl butanoate, Proceedings of the Combustion Institute 33(2011) 995-1002.

[16] V.I. Golovitchev and J. Yang, Construction of combustion models for rapeseed methyl ester bio-diesel fuel for internal combustion engine applications, Biotechnology Advances 27(2009) 641-655.

[17] S. Dooley, M. Uddi, S.H. Won, F.L. Dryer and Y. Ju, Methyl butanoate inhibition of n-heptane diffusion flames through an evaluation of transport and chemical kinetics, Combustion and Flame 159(2012) 1371-1384.

[18] D. Alviso, J.C. Rolon, P. Scouflaire and N. Darabiha, Experimental and numerical studies of biodiesel combustion mechanisms using laminar counterflow spray premixed flame, Fuel 153(2015) 154-165.

[19] P. Dievart, S.H, Won, S. Dooley, F.L. Dryer and Y. Ju, A kinetic model for methyl decanoate combustion, Combustion and Flame 159(2012) 1793-1805.

[20] H. Wu, E. Hu, H. Yu, Q. Li, Z. Zhang, Y. Chen and Z. Huang, Experimental and numerical study on the laminar flame speed of n-Butane/Dimethyl Ether-Air mixtures, Energy & Fuels 28(2014) 3412-3419.

[21] G. Dayma, F. Halter, F. Foucher, C. Togbe, C. Mounaim-Rousselle and P. Dagaut, Experimental and detailed kinetic modeling study of Ethil Pentanoate (Ethyl Valerate) oxidation in a jet stirred reactor and laminar burning velocities in a spherical combustion chamber, Energy and Fuels 26(2012) 4735-4748.

[22] B. Rotavera, A.J. Vissotsky, M.C. Krejci and E.L. Petersen, Laminar flame speed measurements of methyl octanoate, n-nonane and methylcyclohexane, 51st AIAA Aerospace Sciences Meeting Including the New Horizons Forum and Aerospace Exposition, 07-10 January 2013, Grapevine (Dallas/Ft.Worth Region), Texas, USA, 2013.

[23] Z. Zhao, A. Kazakov and F.L. Dryer, Measurements of dimethyl ether/air mixture burning velocities by using particle image velocimeter, Combustion and Flame 139(2004) 52-60.

[24] X. Qin and Y. Ju, Measurements of burning velocities of dimethyl ether and air premixed flames at elevated pressures, Proceedings of the Combustion Institute 30(2005) 233-240.

[25] J. de Vries, W.B. Lowry, Z. Serinyel, H.J. Curran and E.L. Petersen, Laminar flame speed measurements of dimethyl ether in air at pressures up to 10 atm, Fuel 90(2011) 331-338.

[26] C.A. Daly, J.M. Simmie, J. Wurmel, N. Djebaili and C. Paillard, Burning velocities of dimethyl ether and air, Combustion and Flame 125(2001) 1329-1340.

[27] Z. Huang, Q. Wang, J. Yu, Y. Zhang, K. Zeng, H. Miao and D. Jiang, Measurement of laminar burning velocity of dimethyl ether-air premixed mixtures, Fuel 86(2007) 2360-2366.

[28] Z. Chen, L. Wei, Z. Huang, H. Miao, X. Wang and D. Jiang, Measurement of laminar burning velocities of dimethyl-ether-air premixed flames with N_2 and CO_2 dilution, Energy & Fuels 23(2009) 735-739.

[29] C.T. Chong and S. Hochgreb, Measurements of laminar flame speeds of liquid fuels: Jet-A1, diesel, palm methyl esters and blends using particle imaging velocimetry (PIV), Proceedings of the Combustion Institute 33(2011) 979-986.

[30] G. Tian, R. Daniel, H. Li, H. Xu, S. Shuai and P. Richards, Laminar burning velocities of 2.5 dimethylfuran compared with ethanol and gasoline, Energy & Fuels 24(2010) 3898-3905.

[31] X. Wu, Z. Huang, C. Jin, X, Wang, B, Zheng, Y. Zhang and L. Wei, Measurements of laminar burning velocities and Markstein lengths of 2,5 dimethylfuran-air-diluent premixed flames, Energy & Fuels 23(2009) 4355-4362.

[32] X. Ma, C. Jiang, H. Xu, H. Ding and S. Shuai, Laminar burning characteristics of 2-methylfuran and isooctane blend fuels, Fuel 116(2014) 281-291.

[33] Y. Tsutsumi, K. Hoshina, K. Iimima and H. Shoji, Analysis of the combustion characteristics of a HCCI engine on DME and methane, SAE Technical paper 2007-32-0041, 2007.

[34] A.A. Konnov, R.J. Meuwissen and L.P.H. de Goey, The temperature dependence of the laminar burning velocity of ethanol flames, Proceedings of the Combustion Institute 33(2011) 1011-1019.

[35] L. Sileghem, V.A. Alekseev, J. Vancoillie, E.J.K. Nilsson, S. Verhelst and A.A. Konnov, Laminar burning velocities of primary reference fuels and simple alcohols, Fuel 115(2014) 32-40.

[36] G. Broustail, P. Seers, F. Halter, G. Moreac and C. Mounaim-Rousselle, Experimental determination of laminar burning velocity of butanol and ethanol iso-octane blends, Fuel 90(2011) 1-6.

[37] G. Broustail, F. Halter, P. Seers, G. Moreac and C. Mounaim-Rousselle, Experimental determination of laminar burning velocity for butanol/iso-octane and ethanol/iso-octane blends for different initial pressures, Fuel 106(2013) 310-317.

[38] M. Tat and J.H. Van Gerpen, The specific gravity of biodiesel and its blends with diesel fuel. Journal of the American Oil Chemists' Society 77(2000) 115-119.

[39] M. Tat and J.H. Van Gerpen, The kinematic viscosity of biodiesel and its blends with diesel fuel. Journal of the American Oil Chemists' Society 76(2000) 1511-1113.

[40] P. Benjumea, J. Agudelo and A. Agudelo, Basic properties of palm oil biodiesel-diesel blends, Fuel 87(2008), 2069-2075.

[41] Y. Roman-Leshkov, C.J, Barret, Z.Y. Liu and J.A. Dumesic, Production of dimethylfuran for liquid fuels from biomass-derived carbohydrates, Nature 447(2007) 982-985.

[42] H. Yu, E. Hu, Y. Cheng, X. Zhang and Z. Huang, Experimental and numerical study of laminar premixed dimethyl ether/methane-air flame, Fuel 136(2014) 37-45.

[43] W.B Lowry, Z. Serinyel, M.C. Krejci, H.J. Curran G. Bourque and E.L. Petersen, Effect of methane-dimethyl ether fuel blends on flame stability, laminar flame speed and Markstein length, Proceedings of the Combustion Institute, 33(2011) 929-937.

[44] W.S. Song, S.W. Jung, J. Park, O.B. Kwon, Y.J. Kim, T.H. Kim, J.H. Yun and S.I. Keel, Effects of syngas addition on flame propagation and stability in outwardly propagating spherical dimethyl ether-air premixed flames, International Journal of Hydrogen Energy 38(2013) 14102-14114.

[45] J.D. Munzar, B.M. Denman, R. Jimenez, A. Zia, and J.M. Bergthorson, Flame speed and vapor pressure of biojet fuel blends. Proceedings of ASME Turbo Expo 2013: Turbine Technical Conference and Exposition, June 3-7. 2013, San Antonio, Texas, USA.

[46] X. Wu, Q. Li, J. Fu, C. Tang, Z. Huang, R. Daniel, G. Tian and H. Xu, Laminar burning characteristics of 2,5-dimethylfuran and iso-octane blend at elevated temperatures and pressures. Fuel 95(2012) 234-240.

[47] X. Zhang, C. Tang, H. Yu, Q. Li, J. Gong and Z. Huang, Laminar flame characteristics of iso-octane/n-butanol blend-air mixtures at elevated temperatures, Energy & Fuels 27(2013) 2327-2335.

[48] ASTM E681, Standard Test for Concentration Limits of Flammability of Chemicals (Vapors and Gases), American Society for Testing and Materials (ASTM), West Conshohocken, PA, 2001

[49] ASTM E981, Standard Practice for Determining Limits of Flammability of Chemicals at Elevated Temperature and Pressure, American Society for Testing and Materials (ASTM), Washington Office, 2011.

[50] M.G. Zabetakis, Flammability characteristics of combustible gases and vapors, Vol. 627, US Bureau of Mines Bulletin, 1965.

[51] C.J.R. Coronado, J.A. Carvalho Jr, J.C. Andrade, E.V. Cortez, F.S. Carvalho, J.C. Santos and A.Z. Mendiburu, Flammability limits: A review with emphasis in ethanol for aeronautical applications and description of the experimental procedure, Journal of Hazardous Materials 241(2012) 32-54.

[52] C.J.R. Coronado, J.A. Carvalho Jr, J.C. Andrade, A.Z. Mendiburu, E.V. Cortez, F.S. Carvalho, B. Goncalvez, J.C. Quintero, E.I. Gutierrez Velazquez, M.H. Silva, J.C. Santos and M.A.R. Nascimento. Flammability limits of hydrated and anhydrous ethanol at reduced pressures in aeronautical applications, Journal of Hazardous Materials 280(2014) 174-184.

[53] S. Kondo, K. Takisawa, A. Takahashi and K. Tokuhashi, On the temperature dependence of flammability limits of gases, Journal of Hazardous Materials 187(2011) 585-590.

[54] S. Kondo, K. Takisawa, A. Takahashi and K. Tokuhashi, Measurement and numerical analysis of flammability limits of halogenated hydrocarbons, Journal of Hazardous Materials A109(2004) 13-21.

[55] K. Zhang, X. Meng and J. Wu, Flammability limits of binary mixtures of dimethyl ether with five diluent gases, Journal of Loss Prevention in the Process Industries 29(2014) 138-143

[56] D.P. Mishra and A. Rahman, An experimental study of flammability limits of LPG/air mixtures, Fuel 82(2003) 863-866.

[57] M.R. Brooks and D.A. Crowl, Flammability envelopes for methanol, ethanol, acetonitrile and toluene, Journal of Loss Prevention in the Process Industries 20(2007) 144-150

[58] F. Van der Shoor and F. Verplaetsen, The upper explosion limit of lower alkanes and alkenes in air at elevated pressures and temperatures, Journal of Hazardous Materials A128(2006) 1-9.

[59] R.J. Kee, J.K. Grcar, M.D. Smooke and J.A. Miller, A FORTRAN program for modelling steady laminar one-dimensional premixed flames, Sandia Report SAND85-8240 (1985), Sandia National Laboratories.

[60] O.D. Buckley, Development of a spherical combustion chamber for measuring laminar flame speeds in navy bulk fuels and biofuel blends, MSc Thesis, Naval Postgraduate School, Department of Mechanical and Aerospace Engineering, Monterey, California, USA, 2011.

[61] A.P. Kelley, A.J Smallbone, D.L. Zhu and C.K. Law, Laminar flame speed of C_5 to C_8 n-alkanes at elevated pressures: Experimental determination, fuel sensitivity and stretch sensitivity. Proceedings of the Combustion Institute 33(2011) 963-970

[62] A.N. Lipatnikov and J. Chomiak, Turbulent flame speed and thickness: Phenomenology, evaluation, and application in multi-dimensional simulations, Progress in Energy and Combustion Science 28(2002) 1-74

[63] D. Bradley, M. Lawes and M.S. Mansour, Correlation of turbulent burning velocities of ethanol-air, measured in a fan-stirred bomb up to 1.2 MPa, Combustion and Flame 158(2011) 123-138

[64] Z. Chen, On the extraction of laminar flame speed and Markstein length from outwardly propagating spherical flames, Combustion and Flame 158(2011) 291-300

[65] D. Bradley, R.A. Hicks, M. Lawes, C.G.W Sheppard and R. Woolley, The measurement of laminar burning velocities and Markstein numbers for Iso-octane-Air and Iso-octane-n-heptane-Air mixtures at elevated temperatures and pressures in an explosion bomb, Combustion and Flame 115(1998) 126-144.

[66] N. Bouvet, C. Chauveau, I. Gökalp, and F. Halter, Experimental studies of the fundamental flame speeds of syngas (H2/CO)/air mixtures, Proceedings of the Combustion Institute, 33(2011) 913-920.

[67] T. Tahtouh, F. Halter and C. Mounaïm-Rousselle, Measurement of laminar burning speeds and Markstein lengths using a novel methodology, Combustion and Flame 156(2009) 1735-1743.

[68] Z. Chen, M.P. Burke and Y. Ju, Effects of Lewis number and ignition energy on the determination of laminar flame speed using propagating spherical flames, Proceedings of the Combustion Institute 32(2009) 1253-1260.

[69] S.Y. Liao, D.M. Jiang and Q. Cheng, Determination of laminar burning velocity for natural gas, Fuel 83(2004) 1247-1250.

[70] A.P. Kelley and C.K. Law, Nonlinear effects in the extraction of laminar flame speeds from expanding spherical flames, Combustion and Flame 156(2009) 1844-1851.

[71] F. Halter, F. Foucher, L. Landry and C. Mounaïm-Rousselle, Effect of dilution by Nitrogen and/or Carbon Dioxide on Methane and Iso-octane air flames, Combustion, Science and Technology 181(2009) 813-827.

[72] C. Liu, S.S. Shy, M. Peng, C. Chiu and Y. Dong, High pressure burning velocities measurements for centrally-ignited premixed methane/air flames interacting with intense near-isotropic turbulence at constant Reynolds number, Combustion and Flame 159(2012) 2608-2619.

[73] C. Chiu, Y. Dong and S.S. Shy, High-pressure hydrogen/monoxide syngas turbulent burning velocities measured at constant turbulent Reynolds numbers, International Journal of Hydrogen Energy 37(2012) 10935-10946.

[74] N. Bouvet, Experimental and numerical studies of the fundamental flame speeds of methane/air and syngas (H_2/CO)/air mixtures, PhD Thesis, Universite D'Orleans, Ecole Doctorale Sciences et Technologies, Orleans, France, 2009.

[75] D. Singh, Study of surrogates for conventional and synthetic aviation fuel jets, PhD Thesis, Purdue University, Department of Aeronautics and Astronautics, West Lafayette, Indiana, USA, 2009.

[76] A. K. Das, K. Kumar and C. Sung, Laminar flame speeds of moist syngas mixtures, Combustion and Flame. 158(2011) 345-353.

[77] C.M. Vagelopoulos, F.N. Egolfopoulos, Direct experimental determination of laminar flame speeds, Symposium (International) on Combustion. 27(1998) 513-519.

[78] K.J. Bosschaart, Analysis of the heat flux method for measuring burning velocities, Ph.D dissertation. Technische Universiteit Endhoven, The Netherlands, 2002.

[79] N. Bouvet, C. Chauveau, I. Gökalp, S. Lee and R.J. Santoro, Characterization of syngas laminar flames using the Bunsen burner configuration, International Journal of Hydrogen Energy 36(2011) 992-1005.

[80] G. Settles, Schlieren and Shadowgraphic Techniques: Visualizing Phenomena in Transparent Media. Springer-Verlag Berlin Heidenberg 2001.

[81] S. Fabbro, An experimental test facility for studying the effects of turbulence on the evaporation of fuel droplets at elevated pressure and temperature conditions. M.Sc Thesis, Department of Mechanical Engineering. University of Manitoba, Winnipeg, MB, Canada, 2012

[82] S.L. Toth, Experimental study of droplet vaporization and combustion of diesel, biodiesel and their blends in a turbulent environment at elevated pressure and temperature

conditions. M.Sc Thesis, Department of Mechanical Engineering. University of Manitoba, Winnipeg, MB, Canada, 2014.

[83] M. Birouk and S. Fabbro, Droplet evaporation in a turbulent atmosphere at elevated pressure – Experimental data, Proceedings of the Combustion Institute. 34 (2013) 1577-1584.

[84] Y. Cengel and M. Boles, Thermodynamics: An engineering approach, Sixth edition, McGraw Hill, ISBN 978-0-07-352921-9, 2008.

[85] J. Heywood, Internal Combustion Engine Fundamentals. McGraw Hill. ISBN 0-07-028637-X, 1998.

[86] B.E. Milton and J.C Keck, Laminar burning velocities in stoichiometric hydrogen and hydrogen-hydrocarbon gas mixtures, Combustion and Flame 58(1984) 13-22.

[87] ASME Standard 2010 Section VIII Div.1, "Rules for Construction of Pressure Vessels". ASME International, Three Park Avenue, New York, NY, 2010.

[88] W. Yuan, A.C. Hansen and Q. Zhang, Vapor pressure and normal boiling point predictions for pure methyl esters and biodiesel fuels, Fuel 84(2005) 943-950.

[89] C.L. Yaws and H.C. Yang, To estimate vapor pressure easily. Antoine coefficients relate vapor pressure to temperature for almost 700 major organic compounds, Hydrocarbon Processing 68(1989) 65-68.

[90] A. Rose and W.R. Supina, Vapor pressure and vapor-liquid equilibrium data for methyl esters of the common saturated normal fatty acids, Journal of Chemical & Engineering Data 6(1961) 173-179.

[91] R.C. Gonzalez and R.E. Woods, Digital image processing using Matlab, Second edition, Gatesmark Publishing, ISBN 978-0-9820854-0-0, 2009

[92] H.W. Coleman and W. Steele, Experimentation and uncertainty analysis for engineers, First edition, John Wiley & Sons, ISBN 0-471-63517-0, 1989

[93] R.J. Moffat, Describing the uncertainties in experimental results, Experimental Thermal and Fluid Science 1(1988) 3-17

[94] R. Lyman Ott and M. Longnecker, An introduction to statistical methods and data analysis, Sixth Edition, Brooks/Cole Cengage Learning, ISBN 978-0-495-01758-5, 2010

[95] M. Elia, M. Ulinski and M. Metghalchi, Laminar burning velocity of methane-air diluent mixtures, Transactions of ASME 123 (2001) 190-196.

[96] X.J.Gu, M.Z. Haq, M. Lawes and R. Woolley, Laminar burning velocity and Markstein lengths of methane-air mixtures, Combustion and Flame 121(2000) 42-48.

[97] D. Bradley, P.H. Gaskell and X.J. Gu, Burning velocities, Markstein lengths, and flame quenching for spherical methane-air flames: A computational study, Combustion and Flame 104(1996) 176/198

[98] C.K. Law, D.L. Zhu and G. Yu, Propagation and extinction of premixed flames, Proceedings of Combustion Institute Twenty-First Symposium (International) 1986, pp.1419.

[99] G. Andrews and D. Bradley, The burning velocity of methane-air mixtures, Combustion and Flame 19(1972) 275-288.

[100] S.C. Taylor, Burning velocity and the influence of flame stretch, PhD. thesis, Department of Fuel and Energy, University of Leeds, Leeds, United Kingdom, 1991.

[101] L.K. Tseng, M.A. Ismail and G.M. Faeth, Laminar burning velocities and Markstein numbers of hydrocarbon/air flames, Combustion and Flame 95(1993) 410-426.

[102] A.J Smallbone, W. Liu, C.K. Law, X.Q. You and H. Huang, Experimental and modeling study of laminar flame speed and non-premixed counterflow ignition of n-heptane, Proceedings of the Combustion Institute 32(2009) 1245-1252.

[103] L. Sileghem, V.A. Alekseev, J. Vancoillie, K.M. Van Geem, E.J.K. Nilsson, S. Verhelst and A.A. Konnov, Laminar burning velocity of gasoline and the gasoline surrogate components iso-octane, n-heptane and toluene, Fuel 112(2013) 355-365.

[104] S.C. Davis and C.K. Law, Laminar flame speeds and oxidation kinetics of iso-octane air and n-heptane air flames, Twenty-Seventh Symposium (International) on Combustion/The Combustion Institute 1998 pp. 521-527.

[105] M. Birouk, A.I. Chowdhury, D. Levin, M. Sailer and J. Sorensen, On the combustion characteristics of a novel biofuel: heat of combustion and vaporization rate, 25th International Colloquium on the Dynamics of Explosions and Reactive Systems, August 2-7, 2015, Leeds, UK.

[106] S. Gordon and B.J. McBride, Coefficients for calculating thermodynamic and transport properties for individual species, NASA report SP-273 (1971), Washington DC, USA.

Appendix A – Instrumentation

The following is the list of all instrumentation and supplementary devices applied for measuring laminar flame speed with their features.

Pressure Measurement Devices:

- Miniature high temperature pressure transducer Kulite® for measuring fuel partial pressure.
    - Model XTEL-190M-5A
    - Rated pressure: 5 psia (15 psia max. allowable)
    - Rated electrical excitation: 10 VDC (15 VDC max. allowable)
    - Full scale output (FSO): 100 mV nominal (250 mV max. allowable)
    - Sensitivity: 18.498 mV/psia
    - Operating temperature range: -55ºC to 273ºC
    - Combined non-linearity, hysteresis and repeatability: ±0.1% FSO BFSL (typical); ±0.5% FSO (max)
- Stainless steel pressure transducer Kavlico® for measuring fuel/air mixture pressure.
    - Model P155-150G-F1A
    - Rated pressure: 1-150 psig
    - Rated electrical excitation: 4.50 VDC to 5.50 VDC
    - Output voltage: Zero/null pressure 0.50±0.08 VDC

      Full pressure 4.50±0.08 VDC
    - Total error band: <2.0% of span

Temperature Measurement Devices:

- K-type thermocouples from Omega Engineering Inc. placed at the bottom and central region of the spherical combustion chamber.
    - Model: KQXL-18G-[**], where [**] refers to the length of the thermocouple probe. Length of 6 inches were used.
    - Accuracy: ±2.20 °C or 0.75% of the rated temperature range.

Signal Conditioning for high accurate pressure measurements

- Voltage amplifier of the pressure transducer (for fuel partial pressure) from Omega Engineering Inc.
    - Model DMD4059
    - External power supply range: 9-30 VDC / 10-32 VAC
    - Input range: minimum 0 to 5 mV range - 0.5 mV/V sensitivity
      maximum 0 to 400 mV range - 40 mV/V sensitivity
    - Excitation voltage: switch selectable 0.10 VDC in 1V increments
    - Maximum output: 10 VDC at 120 mA
    - Zero offset (tare): ±100% of span in 15% increments
    - Output linearity, ripple and noise: <0.1% of span

Test Rig Data Acquisition System (DAQ) for input (pressure, temperature) and output (camera, axial fans, ignition system) signals.

- DAQ National Instruments NI-cDAQ -9172 main module
    - Input voltage range: 11 VDC to 30 VDC
    - Maximum required Input power: 15 W
    - Analog input
        - Sample rate: 3.2 MS/s (maximum), 0 S/s
        - Time accuracy: 50 ppm of sample rate
        - Timing resolution: 50 ns
    - Analog output
        - Maximum update rate: 1.6 MS/s
        - Timing accuracy: 50 ppm of sample rate
        - Timing resolution: 50 ns
- NI 9205 analog input module
    - Nominal input ranges: ±10 VDC, ±5 VDC, ±1 VDC, ±0.2 VDC
    - Maximum working voltage: ±10.4 VDC
    - ADC resolution: 16 bits
    - Conversion time: 192.3 kS/s
    - Overvoltage protection: ± 30 VDC
    - Operative temperature: -40 ºC to 70 ºC
    - Gain error: 476 ppm
    - Offset error: 139 ppm
    - Noise uncertainty: 72 μVDC

- NI 9263 analog voltage output module
    - Nominal input ranges: ±10 VDC
    - Maximum working voltage: ±11VDC
    - ADC resolution: 16 bits
    - Output impedance : 0.1 Ω
    - Percentage or error: 0.75% (range of ±10.7 VDC)
    - Operative temperature: -40 ºC to 70 ºC
- NI 9211 analog input module
    - Number of channels: 4 thermocouple channels
    - ADC resolution: 24 bits
    - Voltage measurement range: ±80 mVDC
    - Input current: 50 nA
    - Offset error: 20 μVDc max
    - Gain error source impedance: 0.06%
    - Operative temperature: -40 ºC to 70 ºC
- NI 9474 digital output module
    - Number of channels: 8 digital output channels
    - Supply voltage range: 5 – 30 VDC
    - Output voltage: $V_{sup} – (I_0 . R_0)$
    - Output impedance (R_0): 0.13 Ω
    - Continuous output current (I_0): 1 A max per channel

Appendix B – Uncertainty analysis

B.1 Formulation

The total uncertainty of measurements is basically a summation of the contribution of two different uncertainty sources: the systematic (bias) and the random (precision) errors. The systematic errors cannot be estimated by statistic methods alone as they are caused by inherent inaccuracies in the measurement methodology and its associated components (e.g. non-repeatability, non-linearity, hysteresis) that introduce the same errors at any test. On the other hand, random errors are determined by the application of statistical methodologies of repeated measurements at the same conditions [92].

In order to determine the total bias uncertainty (B_{SL}) of laminar flame speed measurements, the following expression is applied [93]:

$$B_{SL} = \sqrt{\sum_{i=1}^{N} \left(\frac{\partial S_L(x_i)}{\partial x_i} B_i \right)^2} \quad \text{(B.1)}$$

where B_i is the elemental bias uncertainties generated by each component in the experiment (pressure transducers, thermocouples, Schlieren system), x_i is any variable that laminar flame speed is dependent upon (pressure, temperature, equivalence ratio) and $\frac{\partial S_L(x_i)}{\partial x_i}$ is the sensitivity of laminar flame speed to this variables (p, T, ϕ). Each of the elemental bias uncertainties is listed in table B.1, and was obtained from the technical datasheets provided by the instrumentation suppliers.

Similarly, the total random uncertainty is calculated based on the sensitivity of laminar flame speed and the contribution of individual random uncertainties as [93]:

$$P_{SL} = \sqrt{\sum_{i=1}^{N} \left(\frac{\partial S_L(x_i)}{\partial x_i} P_i \right)^2} \quad \text{(B.2)}$$

where P_i is the elemental precision (random) uncertainty originated by the measurement devices (referenced in table B.1). The precision uncertainty is determined based on the standard deviation (S_i) of N measurements (corresponding to ν = N-1 degrees of freedom) obtained at the same conditions as:

$$P_i = \frac{S_i}{\sqrt{N}} \quad \text{(B.3)}$$

Device	**Elemental source of error**	**Bias (B_i)**	**Random (P_i)**	**Degrees of freedom (ν)**
Pressure transducer (0-15 psia)	Combined non-linearity, hysteresis and repeatability	± 0.1%		
	Display reading [psi]		0.001036	20
Pressure transducer (0-150 psig)	Combined non-linearity, hysteresis and repeatability	± 2%		
	Display reading [psi]		0.532602	20
Thermocouple K-type # 1	Accuracy [K]	2.2		
	Display reading [K]		0.077064	20
Thermocouple K-type # 2	Accuracy [K]	2.2		
	Display reading [K]		0.05861	20
Thermocouple K-type # 3	Accuracy [K]	2.2		
	Display reading [K]		0.061596	20
Schlieren system	Optical aberrations - spatial [cm]		0.005015	15
High speed camera	Resolution [cm]	0.00795		
Experimental setup	Experimental repeatability [cm/s]		1.042316	4

Table B.1. Elemental uncertainties contributing to the total uncertainty

The elemental bias uncertainty contributed by the pressure transducers and K-type thermocouples were obtained from the manufacture's technical datasheets and the one from the high speed camera was obtained by the observable 1 pixel error band in the electrode width registered by the Schlieren photographs (corresponding to a 0.00795 cm/pixel). The image scale was determined by measuring the electrode diameter (0.23875 cm) and its corresponding pixel width (30 pixels). On the other hand, each elemental random error was calculated by a set of N measurements corresponding to the degrees of freedom (ν) listed in table B.1.

Then, the total uncertainty of measurements is determined by the application of the student's t multiplier as [93]:

$$(U_{SL})_{95} = \sqrt{(B_{SL})^2 + (t.P_{SL})^2} \quad \text{(B.4)}$$

For a 95% confidence level and ν = 4 degrees of freedom (5 measurements), the student's t multiplier corresponds to 2.132, according to table 2 of appendix in ref. [94].

The application of Eq. B.1 and B.2 requires a functional relationship between the laminar flame speed and the different variables affecting its measurement (pressure, temperature, equivalence ratio, etc.), in order to determine its sensitivity to the change of these variables. As a way to determine this relationship, Elia et al. [95] suggested a general expression for laminar flame speed, which can be summarized as follows:

$$S_L = f(\phi)\left(\frac{T}{T_0}\right)^{\alpha}\left(\frac{P}{P_0}\right)^{\beta} \quad \text{(B.5)}$$

where T and T_0 are the test and room temperatures, P and P_0 are the test and atmospheric pressures and ϕ is the equivalence ratio of the fuel/air mixture. According to [95], for

methane/air mixtures, the experimental coefficients were found $\alpha = 1.857$ and $\beta = -0.435$. In addition, the validation of the experimental methodology presented in section 5.2.1 enable the deduction of a 4th grade fitting polynomial that characterizes the laminar flame speed as function of equivalence ratio, then, a hybrid equation for the present experimental results was obtained as:

$$S_L = \left(-401\phi^4 + 1196.6\phi^3 - 1321.1\phi^2 + 697.68\phi - 132.86\right)\left(\frac{T}{T_0}\right)^{1.857}\left(\frac{P}{P_0}\right)^{-0.435} \quad \text{(B.6)}$$

B.2 Calculation

Once the laminar flame speed function has been established, the equation B.1 is applied for each of the partial derivatives, in order to determine the total bias uncertainty as follows:

$$\frac{1}{S_L}\frac{\partial S_L}{\partial \phi}B_\phi = \frac{-1604\phi^3+3589.8\phi^2-2642.2\phi+697.68}{-401\phi^4+1196.6\phi^3-1321.1\phi^2+697.68\phi-132.86}B_\phi \quad \text{(B.7)}$$

$$\frac{1}{S_L}\frac{\partial S_L}{\partial T}B_T = \frac{1.857}{T}B_T \quad \text{(B.8)}$$

$$\frac{1}{S_L}\frac{\partial S_L}{\partial P}B_P = \frac{-0.435}{P}B_P \quad \text{(B.9)}$$

Where B_ϕ, B_T *and* B_P are the elemental bias uncertainties listed in table B.1. Experimentally, the sensitivity of laminar flame speed to flame radius was determined as $S_L = 1.9565\,r$ by tracing the S_L vs r plot from experimental data. Then, the bias uncertainty contribution from flame imaging is given by:

$$\frac{1}{S_L}\frac{\partial S_L}{\partial r}B_r = rB_r \quad \text{(B.10)}$$

Where B_r is the elemental bias uncertainty listed in table B.1.

The total bias uncertainty is calculated as:

$$\left(\frac{B_{SL}}{S_L}\right)^2 = \left(\frac{1}{S_L}\frac{\partial S_L}{\partial \phi}B_\phi\right)^2 + \left(\frac{1}{S_L}\frac{\partial S_L}{\partial T}B_T\right)^2 + \left(\frac{1}{S_L}\frac{\partial S_L}{\partial T}B_T\right)^2 + \left(\frac{1}{S_L}\frac{\partial S_L}{\partial P}B_P\right)^2 + \left(\frac{1}{S_L}\frac{\partial S_L}{\partial r}B_R\right)^2 \qquad \text{(B.11)}$$

and the random uncertainty is determined by:

$$\left(\frac{P_{SL}}{S_L}\right)^2 = \left(\frac{1}{S_L}\frac{\partial S_L}{\partial \phi}P_\phi\right)^2 + \left(\frac{1}{S_L}\frac{\partial S_L}{\partial T}P_T\right)^2 + \left(\frac{1}{S_L}\frac{\partial S_L}{\partial T}P_T\right)^2 + \left(\frac{1}{S_L}\frac{\partial S_L}{\partial P}P_P\right)^2 + \left(\frac{1}{S_L}\frac{\partial S_L}{\partial r}P_R\right)^2 \qquad \text{(B.12)}$$

Where P_ϕ, P_T, P_P and P_r are the elemental random uncertainties listed in table B.1.

As illustrative example, the bias uncertainty is determined for the following conditions:

- Φ = 1.0
- S_L= 38.91 cm/s
- T=298 K
- P=101.325 Kpa
- r = 3.475 cm (for maximum uncertainty)

Then, Eq. B.11 and B.12 are applied as:

$$\frac{B_{SL}}{S_L} = \sqrt{\left(\frac{41.28}{39.32}\,x\,0.001\right)^2 + \left(\frac{1.857}{298}\,x\,2.2\right)^2 + \left(\frac{-0.435}{101.325}x\,0.021\right)^2 + (3.475\,x\,0.00795)^2} = 0.03251$$

$$B_{SL} = 1.26\,cm/s$$

$$\frac{P_{SL}}{S_L} = \sqrt{\left(\frac{41.28}{39.32}\,x\,0.001036\right)^2 + \left(\frac{1.857}{298}\,x\,0.1972\right)^2 + \left(\frac{-0.435}{101.325}x\,0.5336\right)^2 + (3.475\,x\,0.005015)^2} = 0.017669$$

$P_{SL} = 0.68\ cm/s$

Then, by applying Eq.B.4, the total uncertainty of the measurement of laminar flame speed at 95 % confidence is obtained as:

$$(U_{SL})_{95} = \sqrt{(1.2651)^2 + (2.132x0.6875)^2} = 1.9362\ cm/s$$

A complete summary of the total uncertainties at different equivalence ratios is presented in table B.2

ϕ	B_{SL} [cm/s]	P_{SL} [cm/s]	U_{SL} [cm/s]	S_L [cm/s]	%
0.7	0.891	0.3975	1.22965	22.29	5.5166
0.8	1.0601	0.5032	1.50817	28.31	5.3273
1	1.2651	0.6875	1.93623	38.91	4.9762
1.1	1.2995	0.7448	2.05181	42.23	4.8587
1.2	1.3822	0.6713	1.98968	37.81	5.2623
1.3	2.0978	0.4877	2.34131	25.17	9.302

Table B.2. Total uncertainty of laminar flame speed

Appendix C – Image Processing Code

C.1. Introduction

A Matlab was developed to determine the flame radius obtained from Schlieren images taken at known time intervals using CCD high speed camera. Initially, all info/constants are given at the beginning of the code (e.g. threshold, filename), then each image (based on a grayscale from 0 to 255 pixel values) is read and converted to a 1280 x 1024 pixel matrix that is filtered to reduce noise. After image filtering, the ignition electrodes are removed and the flame's edge is detected by applying the Canny edge detector, which basically applies a Gaussian filter to reduce noise and a local gradient at each point in the image fixed at a given threshold. Once the flame's edge is clearly detected, its contour is clearly marked to enclose the flame's area, in order to convert it to white pixels and the rest to dark pixels. Finally, the total area is calculated by counting all white pixels and applying the appropriate scale (referenced in section 4.7.2 as 12.5649 pixels/mm) and the radius is determined assuming circumferential area.

C.2. Matlab code

```
close all
clc
clear

%%%%%%%%%%%%%%%%%%%%%%%%%%%%%%%%%%%%%%%%%%%%%%%%%%%%%%%%%%%%%%%%%%%%%%%%%
%%%%%%%%%%%%%%%%%%%%%%%%%%%%%%%%%%%%%%%%%%%%%%%%%%%%%%%%%%%%%%%%%%%%%%%%%
%%%%%%%%
                           %  Initial Parameters  %

electrode_width_pix = 30;          % Pixels for electrode width -sizing
electrode_width_real = 2.3876;     % Real electrode width in mm
t=0.07;                            % Threshold for mask edge detection
firstpic = 508;                    % Number of first picture
lastpic = 527;                     % Number of last picture


%%%%%%%%%%%%%%%%%%%%%%%%%%%%%%%%%%%%%%%%%%%%%%%%%%%%%%%%%%%%%%%%%%%%%%%%%
%%%%%%%%%%%%%%%%%%%%%%%%%%%%%%%%%%%%%%%%%%%%%%%%%%%%%%%%%%%%%%%%%%%%%%%%%
%%%%%%%%
                         %  Reading File and Filtering  %
tic
for k=firstpic:1:lastpic
    kk=num2str(k);
    filename=strcat('N:\TestSession_216d\Cam_1306060055_000',kk,'.tif');

    a = imread(filename);           % Reading of the picture from file
name
    %figure,imshow(a)

    s1 = 1:1126; s2 = 5:1014;       % Visualization window
    b = a(s1,s2);
    K = medfilt2(a,[10 10]);        % Picture filtering
    %figure,imshow(K)


%%%%%%%%%%%%%%%%%%%%%%%%%%%%%%%%%%%%%%%%%%%%%%%%%%%%%%%%%%%%%%%%%%%%%%%%%
%%%%%%%%%%%%%%%%%%%%%%%%%%%%%%%%%%%%%%%%%%%%%%%%%%%%%%%%%%%%%%%%%%%%%%%%%
%%%%%%%%
                          %   Image Processing %

    seg = strel('square',40);       %%%%%% Electrode Removal
    gc = imclose(K,seg);            %%%%%%%%%%%%%%%%%%%%%%%%
    %figure,imshow(gc)

    BWg = edge(gc,'canny_old',t);   % Edge detection using Canny mask
    s21 = 1:1120; s22 = 5:1000;
    ccg = BWg(s21,s22);
    %figure,imshow(ccg)

    segg = strel('disk',4);         % Morfological edge shaping (disk)
    BW2g = imdilate(ccg,segg);      % Dilation filter
```

```
    %figure,imshow(BW2g)

    IM1g=imfill(BW2g,'holes');      % Fill internal holes as white
regions
    %figure,imshow(IM1g)

    seo = strel('disk',14);
    IM2g = imopen(IM1g,seo);        % Removing white pixels in the
background
    %figure,imshow(IM2g)

%%%%%%%%%%%%%%%%%%%%%%%%%%%%%%%%%%%%%%%%%%%%%%%%%%%%%%%%%%%%%%%%%%%%%%%%%%%%%%%%
%%%%%%%%%%%%%%%%%%%%%%%%%%%%%%%%%%%%%%%%%%%%%%%%%%%%%%%%%%%%%%%%%%%%%%%%%%%%%%%%
%%%%%%%%
                      % Flame Area and Radius Calculation %

    kkk=k-firstpic+1;
    TOT(kkk)=sum(sum(IM2g));                          % Counting white
pixels
    sf=electrode_width_pix/electrode_width_real;      % Scaling picture
    Area=TOT;
    radius=(Area/(pi*(sf)^2)).^(0.5);                 % Area calculation

    toc
end


%%%%%%%%%%%%%%%%%%%%%%%%%%%%%%%%%%%%%%%%%%%%%%%%%%%%%%%%%%%%%%%%%%%%%%%%%%%%%%%%
%%%%%%%%%%%%%%%%%%%%%%%%%%%%%%%%%%%%%%%%%%%%%%%%%%%%%%%%%%%%%%%%%%%%%%%%%%%%%%%%
%%%%%%%%
                      % Storage Data in External File %

TOT1 = radius';
tag='Flame Area';
csvwrite('data.csv',TOT1,1,1);
```

Appendix D – Procedure of operation

D.1. Components

In order to conduct the flame speed experiment, the components that must be configured are the following:

- A spherical combustion chamber which includes several components (e.g. flanged windows, thermal insulation, heating coils, pressure relief valves)
- Fuel supply system for liquid fuels (high temperature control valve, gas fuel tank, fuel hose, manifold valve)
- Fuel supply system for liquid fuels (using the volumetric methodology) composed by several elements (e.g. 1 and 10 ml syringes, 3” long needle, ball control valve.
- Fuel supply system for liquid fuels (using the partial pressure methodology) including several elements (e.g. liquid fuel tank, vaporization vessel, ball control valve, needle valve, flexometallic hose, high temperature heating tape, temperature controller).
- 8 Axial fans including the main control box, cooling fans, computer control panel, etc
- Pressure measurement configured with two different sensors (e.g. 0-150 psi and 0-15 psi pressure transducers).
- Temperature measurement based on three K-type thermocouples placed at different locations of the combustion vessel.

- A data acquisition system which encompasses by several devices (e.g. a main module NI cDAQ 9172, I/O modules and a signal conditioner)
- An ignition system including tungsten electrodes and their holders, high voltage cables and power supply.
- A preheated air line using a heating system and a flow control valve.
- An image flame visualization technique composed of several elements (e.g. spherical mirrors, high speed camera, LED light source, tripods, PC for image recording and processing).
- Vacuum pump provided with a high temperature hose and a needle valve

D.2. Procedure

D.2.1. Preliminary activities

D.2.1.1 Computers and power supply

1. Turn on both computers for image processing (left side) and data acquisition system (right side) respectively
2. Turn on the variable power supply, which activates a 5 VCD supply for high pressure transducer (0-150 psi) and the 12 VDC supply for the ignition system's solid state relay
3. Turn on the NI cDAQ 9172 data acquisition main module which controls the operation of the National Instruments acquisition system used to control all the instrumentation of the spherical combustion chamber.

D.2.1.2 Schlieren system

1. Turn on the Motion Studio software (using the main computer)
2. Place both mirror tripods at the locations marked on the floor (focal point of each mirror).
3. Turn on the LED light source
4. Connect the high speed camera as follows: yellow cable at the Sync in port, gray cable at the USB port and black cable at the power port
5. Turn on the high speed camera
6. Activate the IDT Motion Studio software (using the main computer) for image recording
7. Verify the alignment of the Schlieren system before running experiments. This can be achieved as follows:
    - Place both mirrors at a distance equal to the focal length (60”), which is the distance between the combustion chamber center and mirror
    - The LED source light must be placed at the left side of the combustion chamber (see top view of Fig. 4.17 in chapter 4)
    - The LED source light must reflect the light beam concentric onto the optical window from the spherical mirror located at the north side of the vessel (see Fig. 4.17)
    - The south side mirror (camera side) must be aligned by focusing the reflected light beam onto the camera’s lens.

- Adjust the image by moving the camera (vertically and slightly twisting horizontally) as required and simultaneously checking the obtained Schlieren image in Motion Studio (such as the image shown in Fig 4.21)

D.2.1.3 Combustion chamber

1. Perform a visual inspection of the windows to verify that they are clean. If not, remove and clean them up (refer to the procedure of removal and cleaning optical windows)
2. Once the optical windows have been cleaned and installed, they should be covered with thermal insulation to avoid heat leakage/loss and thus avoid condensation on the inner surface of the windows
3. Close all the valves attached to the combustion chamber
4. Perform a pressure test (usually at 20 psig) for a period of 5 minutes to make sure that the windows are placed correctly with no leakage

D.2.1.4 Axial fans

1. Turn on the cooling fans of the eight axial fans (red switch at the lower right side of the spherical chamber table)
2. Switch ON the control box of the axial fans (turning right the selector)
3. Press the GREEN BUTTON to activate the operation
4. At the control panel (Labview user interface) select the following:
    a. Current RPM = 0
    b. Target RMP = Desired value

5. Pulse ENABLE MOTORS and ADJUSTABLE VOLTAGE press buttons from the user interface in Labview

D.2.1.5 Heating system

1. Turn on both switches at each of the heating system control boxes
2. Select the desired temperature at each temperature controller
3. Turn on the variable power supply of the air heater
4. Tune 70% at the variable selector of the power supply

D.2.1.6 Ignition system

1. Verify the alignment of both tungsten electrodes by visual inspection where a gap of 1 mm should be observed - checked by a small ruler.
2. Verify that both electrode wires are connected to the electrode holders
3. Connect the power supply of the ignition system to the power strip OFF mode to prevent any electrical shock

D.2.2. Experiments

D.2.2.1 Gaseous fuels

1. Open the gaseous fuel tank
2. Open the ball valve at the manifold to allow the fuel to flow to the combustion chamber
3. Verify at the user interface (Labview) that the desired temperature at the combustion chamber has been achieved

4. Vacuum the combustion chamber until the maximum allowable vacuum pressure (around 3.0 psia) is achieved. The vacuum pressure was set 3.0 psia as this is the minimum allowable vacuum pressure generated by the vacuum pump
5. Open slightly the air valve to allow preheated air to fill the combustion chamber until reach 13 psia (read by the 0-15 psia pressure transducer) and then close it
6. Open slightly the gaseous fuel valve to allow the fuel to fill the chamber until the target/desired partial pressure is achieved (measured by the 0-15 psia pressure transducer)
7. Close the ball valve of the 0-15 psia pressure transducer to protect it from high pressure peaks
8. Open the high pressure transducer (0-150 psig)
9. Complete the preheat air filling until reaching the fuel/air mixture target/set pressure (measured with the 0-150 psig pressure transducer)
10. Allow 5 minutes for fuel/air stirring time. Fuel/air mixture stirring is generated by setting the axial fans at 500 rpm
11. Turn on the power strip at which the ignition system is connected
12. Turn off the fans by setting in the user interface (Labview):
    a. Selecting Target RPM = 0
    b. Pressing ADJUSTABLE VOLTAGE
13. Once the fuel/air mixture is ready to be ignited, press the record button at IDT Motion Studio interface (left computer), followed by the IGNITION button at the Labview user interface (right computer)

14. Once the fuel/mixture is ignited and flame propagation is recorded, turn OFF the power strip of the ignition system.
15. Open the exhaust and the preheated air valves in order to flush the burnt gases from previous combustion experiments.
16. Close both valves (exhaust and preheated air) and open the vacuum pump valve
17. Turn on the vacuum pump to vacuum the combustion chamber (until reaching 3.0 psia)
18. Fill in the chamber with preheated air until atmospheric pressure
19. Repeat three (3) times steps 15 to 18 in order to flush and vacuum the chamber at least three times, ensuring complete removal of burnt gases.

D.2.2.2 Liquid fuels

D.2.2.2.1 Volumetric methodology

1. Prepare the fuel to be injected by filling in the syringe with the desired fuel volume to be injected inside the combustion chamber. In order to accurately measure the fuel volume, a 1 ml syringe (0.01 ml scale resolution) is used to fill a 10 ml syringe (0.1 ml resolution).
2. Select a temperature of about 40 ºC higher than the desired/test temperature of the experiment (this should be done with both heating coil control boxes in order to reach the test target temperature)
3. Once the temperature reaches this level, turn off the control boxes of the heating coils to allow the heating element to cool down during about 6 minutes so that the

desired/test initial temperature is reached. Typical example is shown in in Fig. D.1 where the test temperature is indicated by the plateau

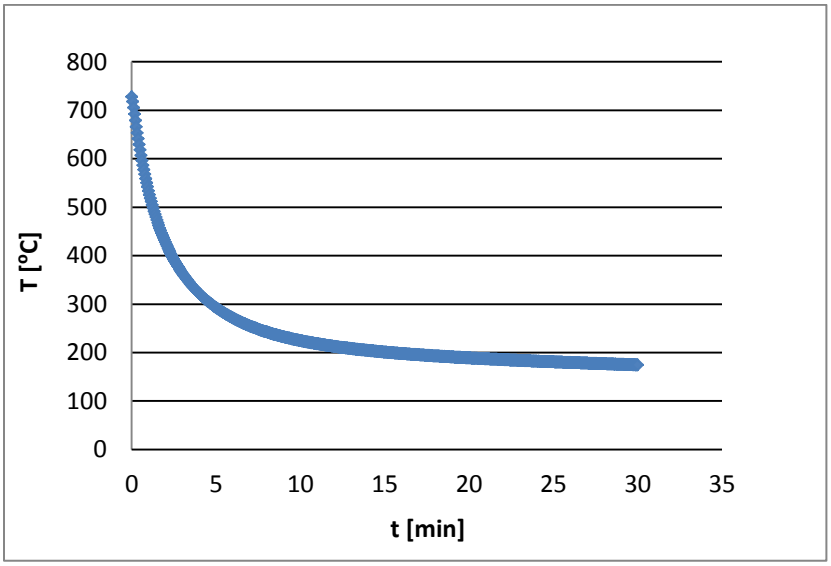

Figure D.1. Change in heating coil temperature when turning off the heating elements

4. Vacuum the combustion chamber up to about 3.0 psia (pressure allowable by the vacuum pump)
5. Once the chamber is vacuumed, turn off the vacuum pump and close its needle valve
6. Place the 10 ml syringe at the top of the combustion chamber as shown in Fig. 4.7.
7. Open the ball valve at the top to allow the fuel to be injected into the chamber
8. Once the fuel is injected, remove the syringe and close the ball valve
9. Fill in the vessel with preheated air until reaching the total combustion air pressure
10. Allow the fans to stir the fuel/air mixture until the experimental temperature is achieved (about 5 minutes)
11. Turn on the power strip at which the ignition system is connected

12. Turn off the fans by setting in the user interface (Labview):
    a. Selecting Target RPM = 0
    b. Pressing ADJUSTABLE VOLTAGE
13. Turn ON the power strip connected to the ignition system power supply
14. Once the fuel/air mixture is ready to be ignited, press the record button at IDT Motion Studio interface (left computer), followed by the IGNITION button at the Labview user interface (right computer)
15. Once the fuel/mixture is ignited and flame propagation images are recorded, turn OFF the power strip of the ignition system.
16. Open the exhaust and the preheated air valves in order to flush the burnt gases from previous combustion experiments.
17. Close both valves and open the vacuum pump valve
18. Turn on the vacuum pump to vacuum the combustion chamber (until reaching the allowable vacuum pressure of 3.0 psia)
19. Turn off the vacuum pump and close its needle valve
20. Fill the chamber with preheated air until atmospheric pressure, in order to prepare the next sequence of flushing and vacuuming
21. Repeat three (3) times steps 16 to 20 at least three times, in order to remove burnt gases from previous experiments.

D.2.2.2.2 Partial pressure methodology (this methodology hasn't been used in the present test as further improvements are required in order to make it fully operational)

1. Wrap the vaporization chamber and the flexometalic hose with the high temperature heating tape.
2. Ensure the thermocouple is attached to the vaporization chamber and connected to the temperature controller placed at the right side of the chamber's table
3. Turn ON the temperature controller and set the desired temperature for the vaporization chamber
4. Ensure all valves attached to the spherical combustion chamber are closed.
5. Ensure both valves (the ball valve between both cylindrical vessels and the needle valve between vaporization and combustion chambers) are closed
6. Wait until the internal volume of the vaporization chamber reached the fixed temperature (registered by the K-type thermocouple attached to the vaporization vessel)
7. Open the ball valve of the high accurate pressure transducer (0-15 psia)
8. Vacuum the combustion chamber (until reaching 3.0 psia)
9. Fill in with liquid fuel the cylindrical tank (at the top of both cylindrical vessels)
10. Open the ball valve to allow liquid fuel flow from the cylindrical tank
11. Close the ball valve when the liquid fuel reaches the vaporization chamber
12. Wait 5 minutes to allow complete vaporization of the liquid fuel. The 5-minute period is based on n-heptane experiments, however, this time may vary depending the fuel; where heavier hydrocarbons (e.g. decane, dodecane) or biodiesel

surrogates (e.g. 1,3 DMO) are expected to require longer periods for ensuring complete vaporization.

13. Open slightly the needle valve to allow the vaporized fuel to flow to the combustion chamber until reaching the desired fuel partial pressure
14. Close the needle valve from the vaporization chamber
15. Close the ball valve of the high accurate pressure transducer (0-15 psia), in order to protect it from peak pressures
16. Open the ball valve of the high pressure transducer (0-150 psig)
17. Fill with preheated air the chamber until reaching the desired total pressure at the combustion chamber
18. Close the preheated air valve
19. Allow 5-minute stirring time of the fuel/air mixture
20. Turn on the power strip at which the ignition system is connected
21. Turn off the fans by setting in the user interface (Labview):
    a. Selecting Target RPM = 0
    b. Pressing ADJUSTABLE VOLTAGE
22. Turn ON the power strip connected to the ignition system power supply
23. Once the fuel/air mixture is ready to be ignited, press the record button at IDT Motion Studio interface (left computer), followed by the IGNITION button at the Labview user interface (right computer)
24. Once the fuel/mixture is ignited and flame propagation images are recorded, turn OFF the power strip of the ignition system.

25. Open the exhaust and the preheated air valves in order to flush the burnt gases from previous combustion experiments.
26. Close both valves and open the vacuum pump valve
27. Turn on the vacuum pump to vacuum the combustion chamber (until maximum allowable vacuum pressure of 3.0 psia)
28. Fill the chamber with preheated air until atmospheric pressure
29. Repeat three (3) times steps 25 to 28 in order to flush and vacuum the chamber at least three times, ensuring complete removal of gases.

Appendix E – Calibration of relief valves

In order to determine the required number of valves that can safely release peak pressures so that the set pressure remains constant, the criteria shown in section UG-131 and mandatory appendix 11 of ASME VIII Div.1 standard was followed, where a maximum operating pressure at the combustion chamber of 290 psi was considered as the critical condition because this is the higher pressure capacity of the combustion chamber. The criteria accounts for the following expression for effective discharge area [87]:

$$A_r = \frac{W\sqrt{TZ}}{CKPK_b\sqrt{M}} \tag{E.1}$$

where the number of required valves can be expressed as:

$$N = \left\lfloor \frac{A_r}{A_v} \right\rfloor + 1 \tag{E.2}$$

Table E.1 summarizes the terms in Eq. E.1 and Eq. E.2:

Variable	Description	Units	Value
W	Required flow through device	lb/h	8465
C	Coefficient determined by k=Cp/Cv (see Fig 11-1 in Mandatory Appendix 11)	--	355
T	Inlet gas temperature	R	959.67
Z	Compresibility factor	--	1 (ideal gas assumption)
K	Coefficient of discharge (ratio of actual to theoretical flow)	--	0.975
P	Pressure	Psi	290
M	Gas molecular weight	g/mol	296
Av	Valve effective discharge area (From valve supplier)	in^2	0.19
Ar	Required effective discharge area (obtained from Eq. 4.6)	in^2	To determine
N	Number of required valves	--	3

Table E.1. Parameters of Eq. E.1 and E.2

The selected valve for the present investigation is a HY-LOK model RV1MF-4N-S316 that can be adjusted in a range of working pressures between 10-250 psig with an orifice of 0.19 in^2 and can operate as temperatures up to 204°C. In order to afford higher temperatures at the combustion chamber, the relief valve was connected to a tubing (¼" x 8" length) attached to the vessel, in order to allow cooling the gases at the valve.

In order to adjust the set pressure before operating the relief valve, the following steps must be followed:

1) Rotate the adjustment nut to the desired set pressure (clockwise rotation increases set pressure) at each of the 3 relief valves
2) Tighten the lock nut against the adjustment nut of each valve
3) Measure the pressure at the combustion chamber by using the 0-150 psi pressure transducer at atmospheric pressure
4) Pressurize the vessel at the set pressure
5) Verify that measured and relief pressures match
6) If relief and set pressures do not match, rotate the adjustment nut in the appropriate direction to allow correspondence.

Repeat steps 2 to 5 until calibration is achieved

Appendix F – Tables

Fuel Partial Pressure [psi]			Mixture partial Pressure		ϕ
Methane	Heptane	1,3 DMO	[psi]	[bar]	
1.123895	0.2175	0.166025	14.5	1	0.8
1.378225	0.267815	0.20996	14.5	1	1
1.502264	0.298265	0.227418	14.5	1	1.1
1.6095	0.3248	0.25636	14.5	1	1.2
1.742146	0.35119	0.268	14.5	1	1.3
2.24779	0.435	0.33205	29	2	0.8
2.75645	0.53563	0.41992	29	2	1
3.004528	0.59653	0.454836	29	2	1.1
3.219	0.6496	0.51272	29	2	1.2
3.484292	0.70238	0.536	29	2	1.3
5.619475	1.0875	0.830125	72.5	5	0.8
6.891125	1.339075	1.0498	72.5	5	1
7.511321	1.491325	1.13709	72.5	5	1.1
8.0475	1.624	1.2818	72.5	5	1.2
8.71073	1.75595	1.34	72.5	5	1.3
7.867265	1.5225	0.830125	101.5	7	0.8
9.647575	1.874705	1.0498	101.5	7	1
10.51585	2.087855	1.13709	101.5	7	1.1
11.2665	2.2736	1.2818	101.5	7	1.2
12.19502	2.45833	1.34	101.5	7	1.3
11.23895	2.175	1.66025	145	10	0.8
13.78225	2.67815	2.0996	145	10	1
15.02264	2.98265	2.27418	145	10	1.1
16.095	3.248	2.5636	145	10	1.2
17.42146	3.5119	2.68	145	10	1.3

Table F.1. Partial pressure of tested fuels

Fuel Volume			Mixture partial Pressure		ϕ
[ml]			[psi]	[bar]	
Heptane at 80ºC	Heptane at 150ºC	1,3 DMO at 150ºC			
1.95	1.63	1.774	14.5	1	0.7
2.23	1.867	2.027	14.5	1	0.8
2.79	2.33	2.534	14.5	1	1
3.076	2.56	2.788	14.5	1	1.1
3.35	2.8	3.041	14.5	1	1.2
3.63	3.03	3.295	14.5	1	1.3
3.9	3.26	3.548	29	2	0.7
4.46	3.734	4.054	29	2	0.8
5.58	4.66	5.068	29	2	1
6.152	5.12	5.576	29	2	1.1
6.7	5.6	6.082	29	2	1.2
7.26	6.06	6.59	29	2	1.3
9.75	8.15	8.87	72.5	5	0.7
11.15	9.335	10.135	72.5	5	0.8
13.95	11.65	12.67	72.5	5	1
15.38	12.8	13.94	72.5	5	1.1
16.75	14	15.205	72.5	5	1.2
18.15	15.15	16.475	72.5	5	1.3
13.65	11.41	12.418	101.5	7	0.7
15.61	13.069	14.189	101.5	7	0.8
19.53	16.31	17.738	101.5	7	1
21.532	17.92	19.516	101.5	7	1.1
23.45	19.6	21.287	101.5	7	1.2
25.41	21.21	23.065	101.5	7	1.3
19.5	16.3	17.74	145	10	0.7
22.3	18.67	20.27	145	10	0.8
27.9	23.3	25.34	145	10	1
30.76	25.6	27.88	145	10	1.1
33.5	28	30.41	145	10	1.2
36.3	30.3	32.95	145	10	1.3

Table F.2. Fuel volumes

Condensation Temperature [C]			ϕ	Mixture Pressure [bar]
Methane (CH_4)	**n-Heptane (C_7H_{16})**	**Methyl octanoate ($C_{19}H_{18}O_2$)**		
-188.631	-7.406	64.004	0.5	1
-186.498	-2.282	70.081	0.7	
-185.561	-0.233	72.548	0.8	
-184.057	3.167	77.063	1	
-182.876	6.416	81.015	1.2	
-181.272	9.654	84.769	1.5	
-183.689	3.564	76.933	0.5	2
-181.278	9.246	83.59	0.7	
-180.216	11.522	86.296	0.8	
-178.512	15.574	91.253	1	
-177.163	18.582	95.599	1.2	
-175.334	22.54	99.733	1.5	
-176.124	19.961	95.971	0.5	5
-173.252	26.534	103.53	0.7	
-171.983	29.174	106.609	0.8	
-169.94	33.882	112.259	1	
-168.317	37.388	117.222	1.2	
-166.109	42.01	121.953	1.5	
-172.993	26.612	103.596	0.5	7
-169.918	33.565	111.533	0.7	
-168.557	36.361	114.769	0.8	
-166.363	41.352	120.71	1	
-164.619	45.072	125.934	1.2	
-162.242	49.98	130.916	1.5	
-169.432	34.084	112.096	0.5	10
-166.117	41.477	120.465	0.7	
-164.647	44.454	123.88	0.8	
-162.276	49.772	130.156	1	
-160.386	53.741	135.679	1.2	
-157.807	58.983	140.951	1.5	

Table F.3. Condensation Temperatures

Appendix G – Drawings

G.1 – Ignition electrode holder

G.1.1 – Exploded view

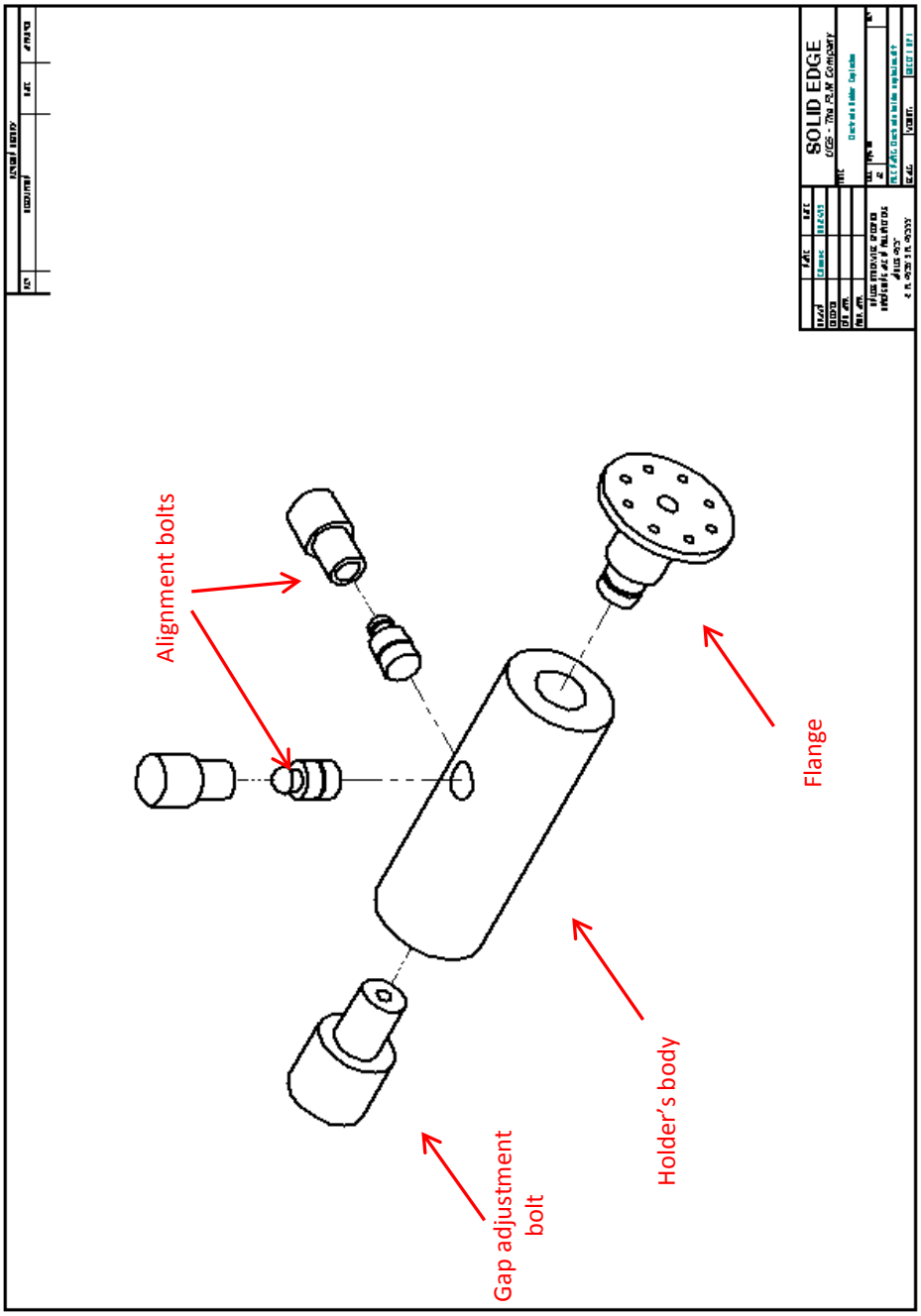

G.1.2 – Holder's body

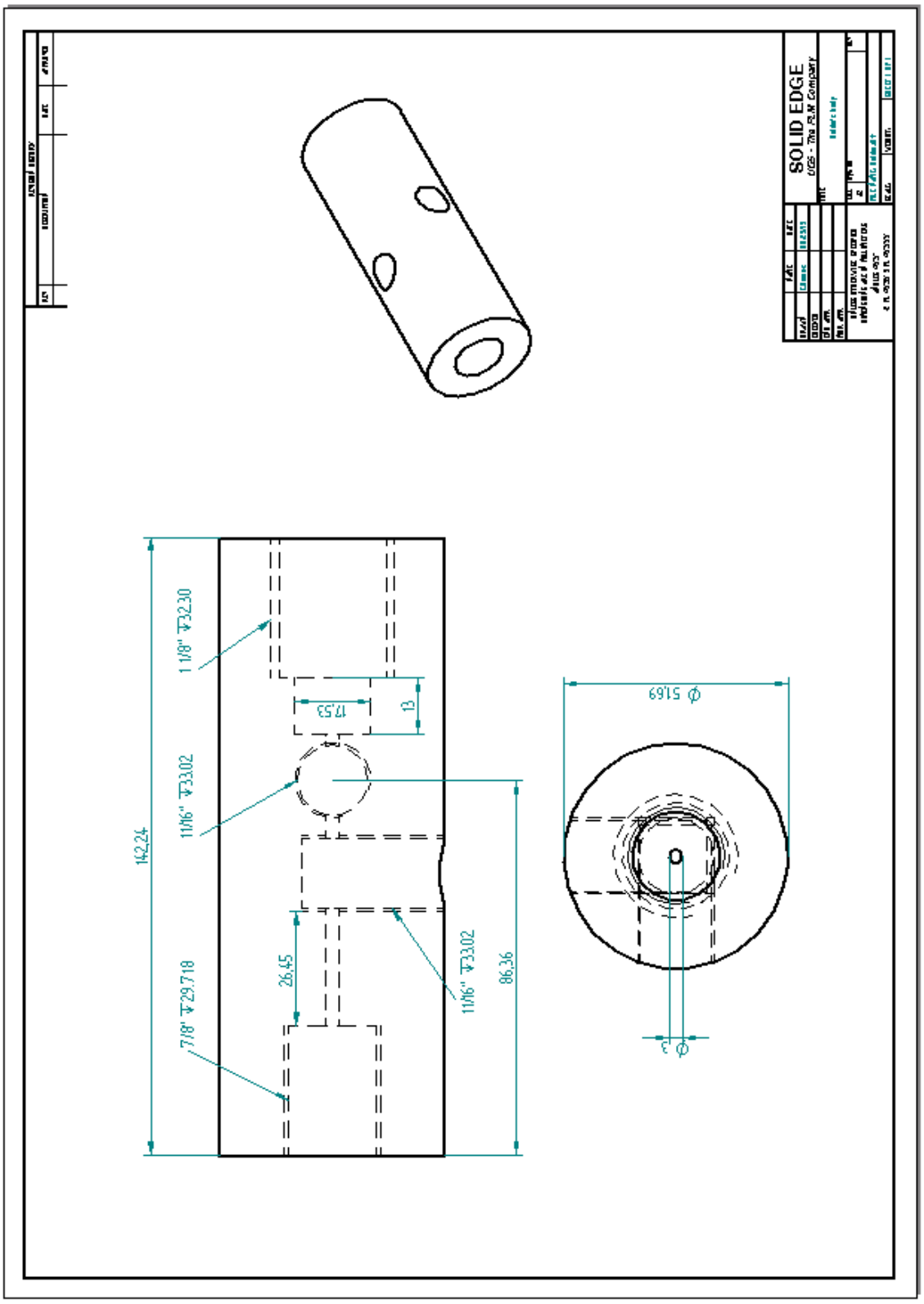

G.1.3 – Gap adjustment bolt

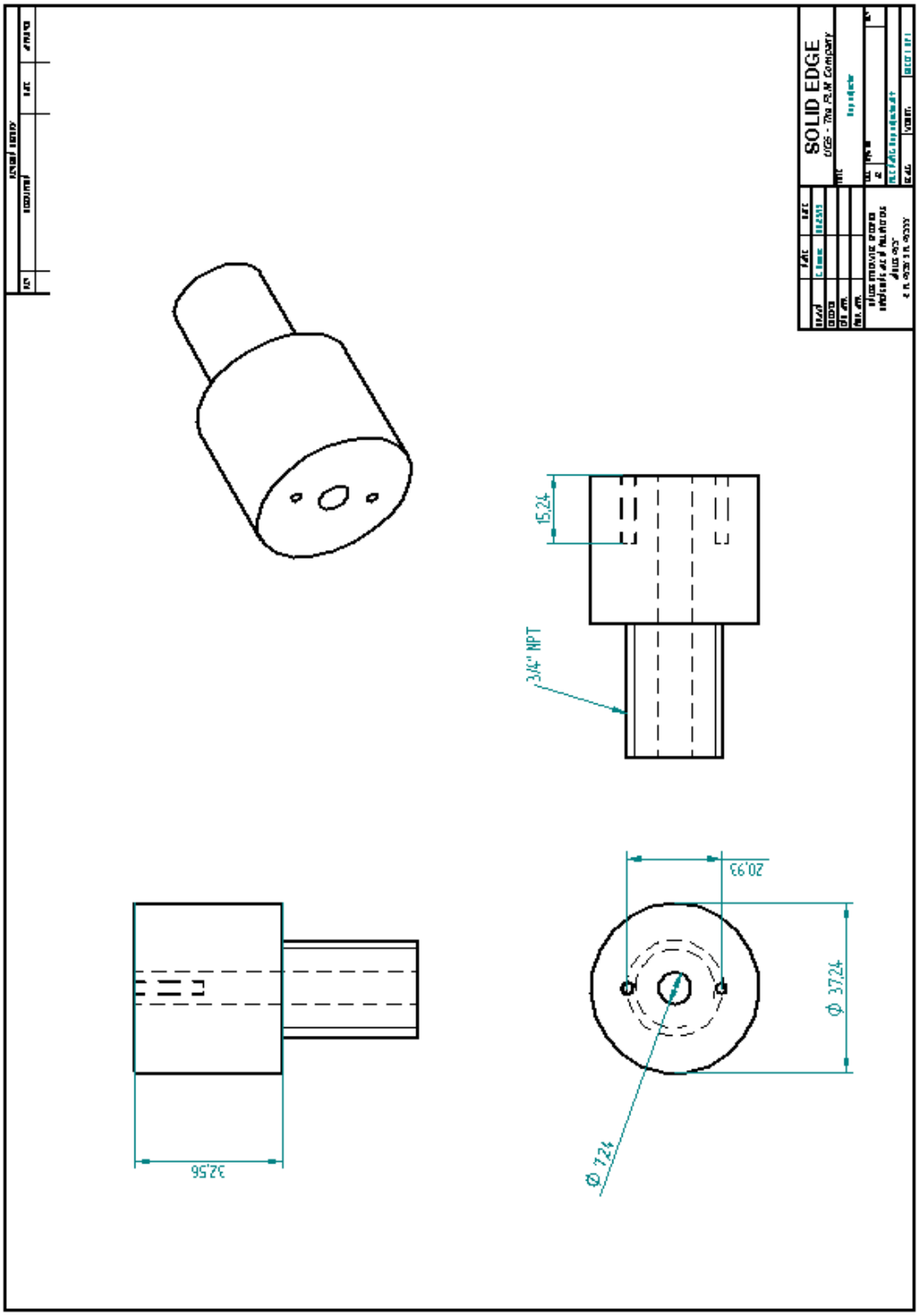

G.1.4 – Alignment bolt

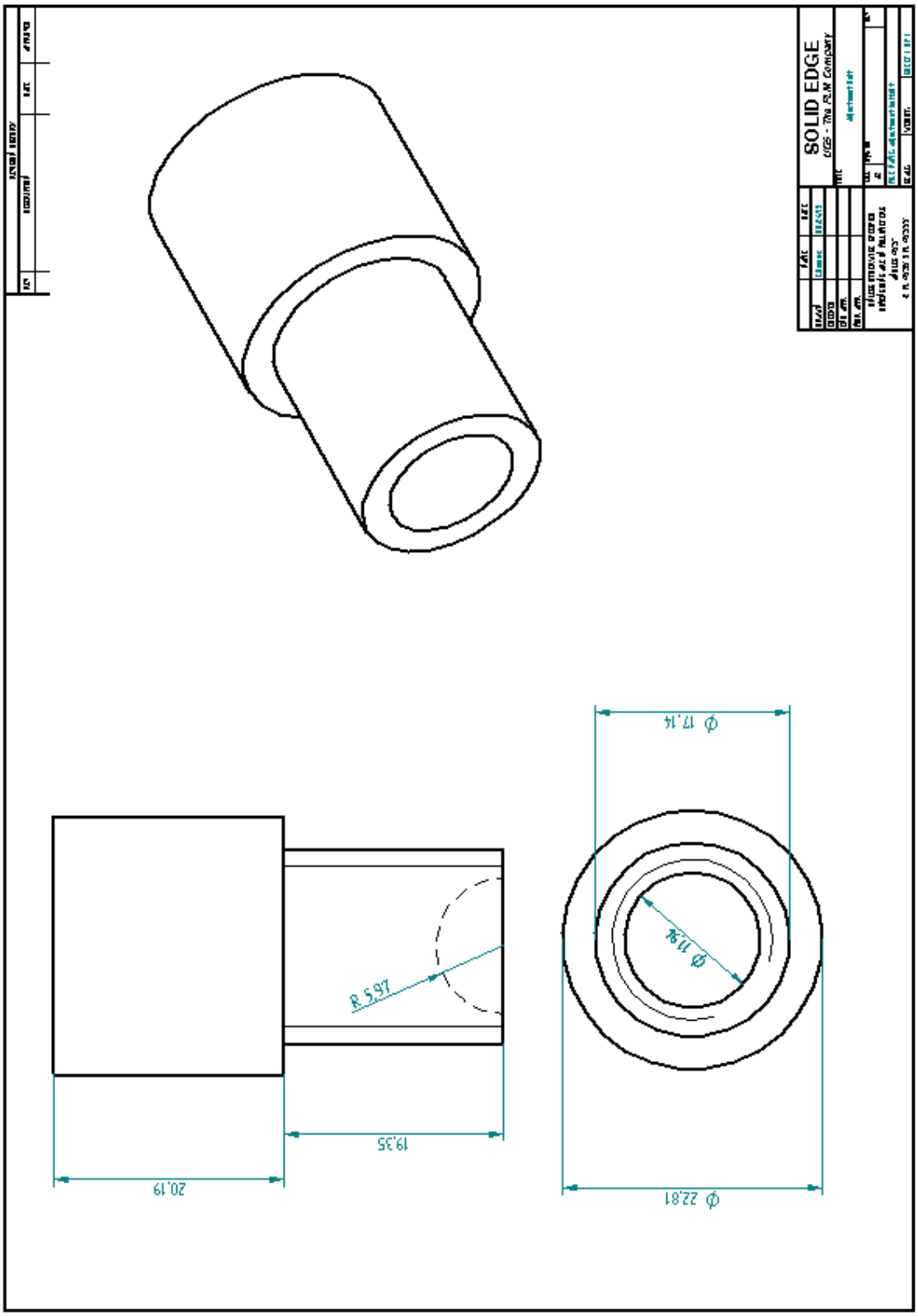

G.1.5 – Alignment bolt end

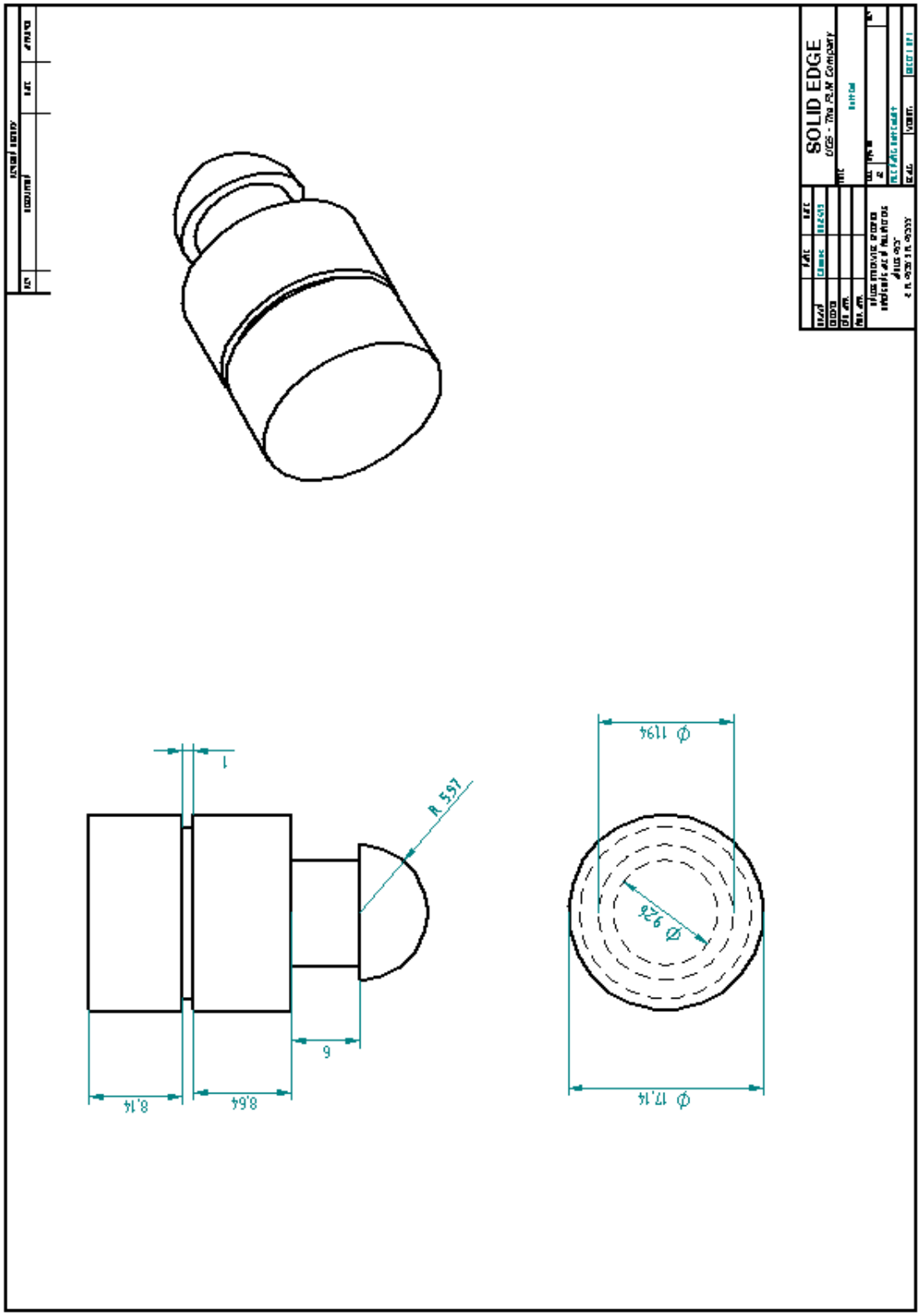

G.2 – Vaporization system

G.2.1 – Liquid fuel tank

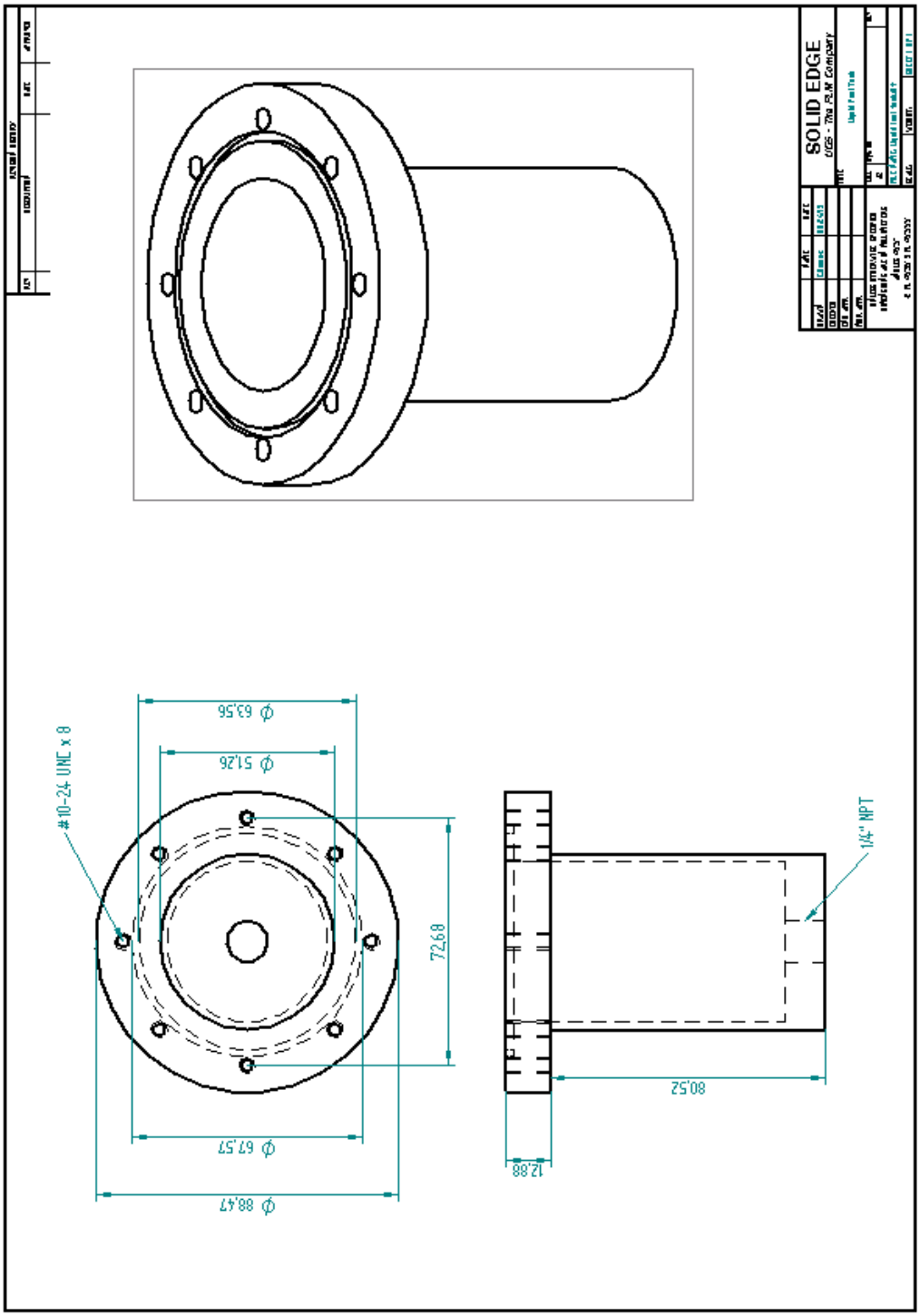

G.2.2 – Liquid fuel tank cap

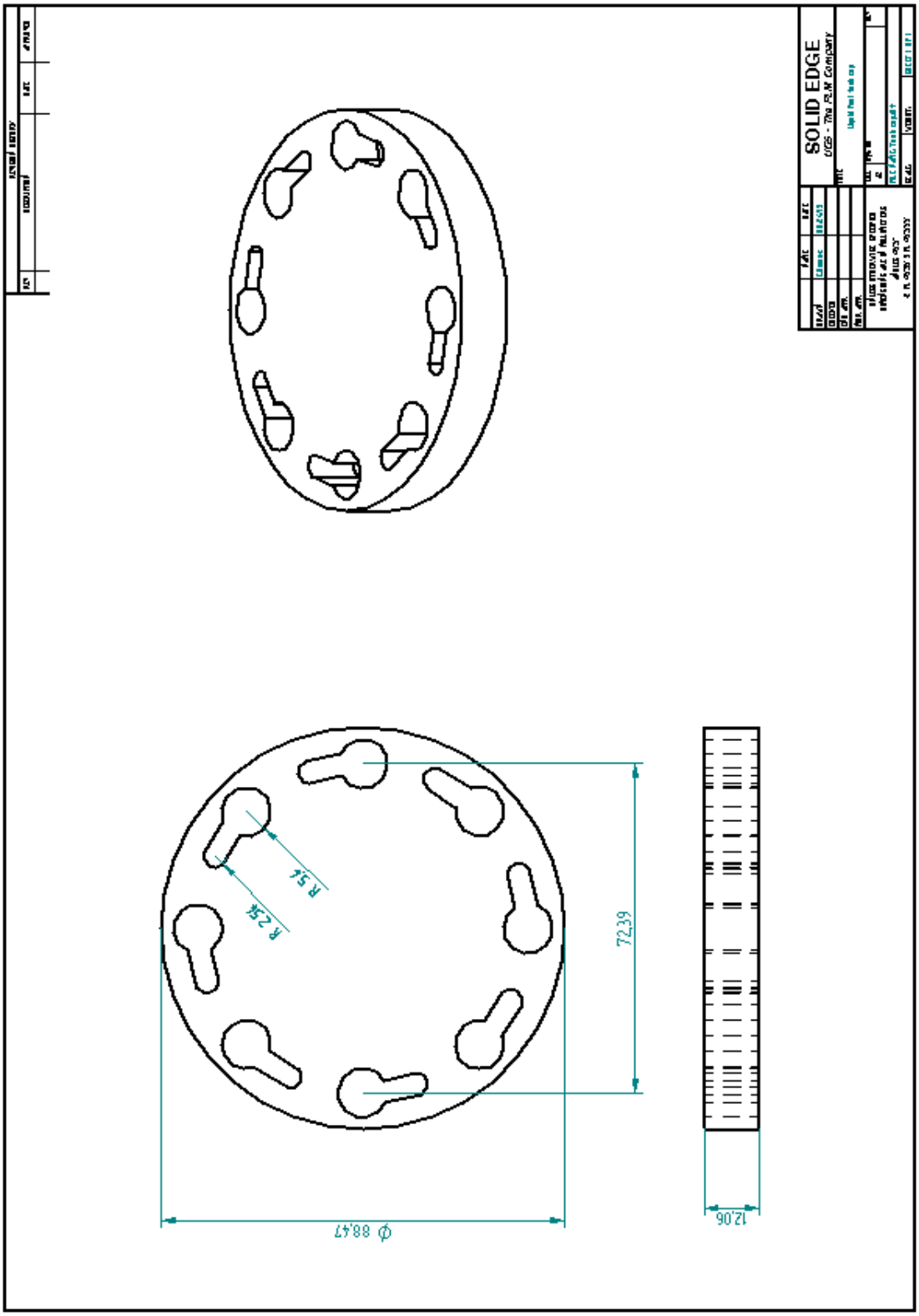

G.2.3 – Vaporization chamber

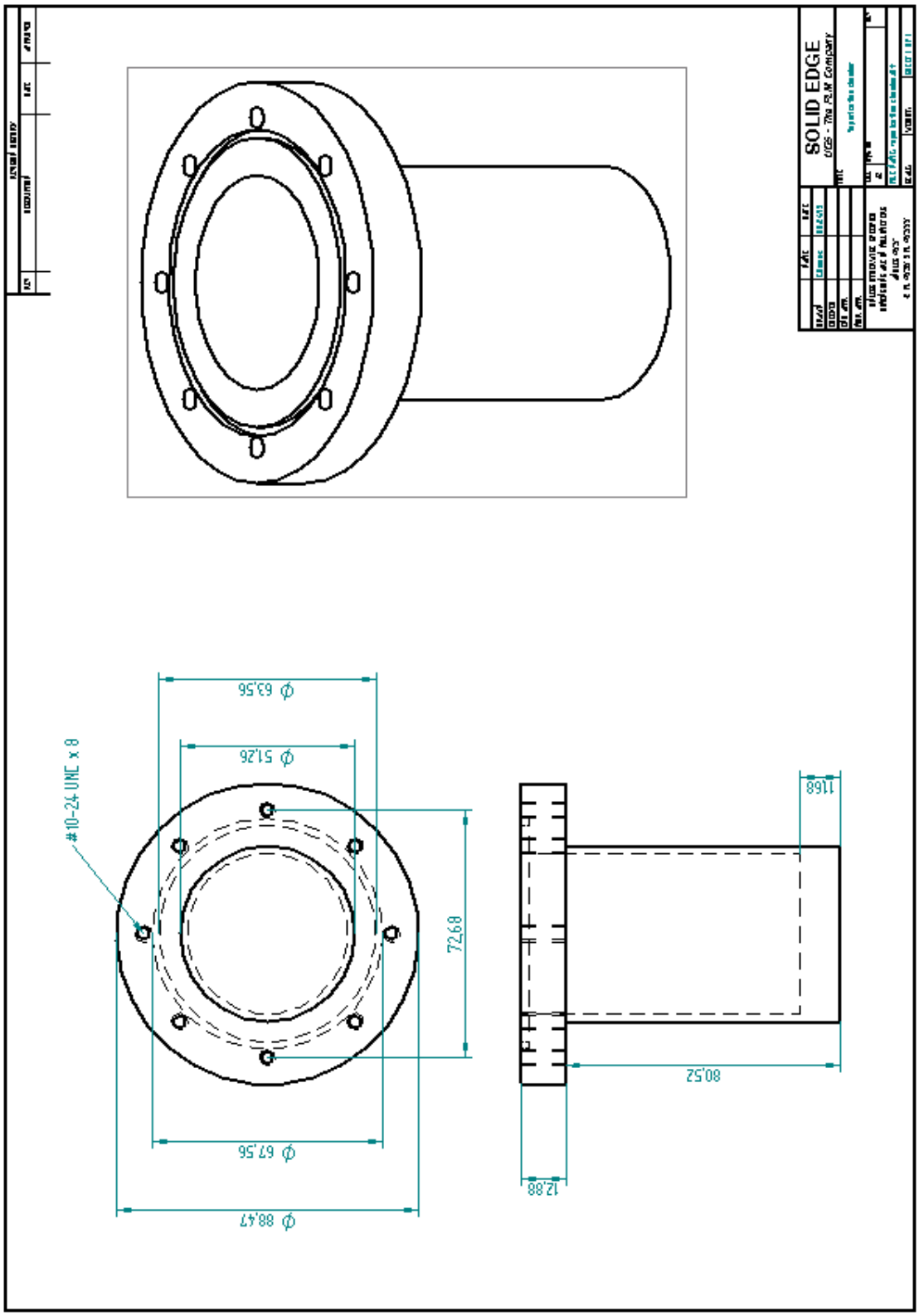

G.2.4 – Vaporization chamber cap